SANDIA REPORT
SAND2022-2751
Printed March 2022

Sandia National Laboratories

MELCOR Accident Progression and Source Term Demonstration Calculations for a FHR

Kenneth Wagner
Troy Haskin
Brad Beeny
Fred Gelbard
David Luxat

Prepared by
Sandia National Laboratories
Albuquerque, New Mexico
87185 and Livermore,
California 94550

Issued by Sandia National Laboratories, operated for the United States Department of Energy by National Technology & Engineering Solutions of Sandia, LLC.

Available to DOE and DOE contractors from
U.S. Department of Energy
Office of Scientific and Technical Information
P.O. Box 62
Oak Ridge, TN 37831

Telephone: (865) 576-8401
Facsimile: (865) 576-5728
E-Mail: reports@osti.gov
Online ordering: http://www.osti.gov/scitech

Available to the public from
U.S. Department of Commerce
National Technical Information Service
5301 Shawnee Rd
Alexandria, VA 22312

Telephone: (800) 553-6847
Facsimile: (703) 605-6900
E-Mail: orders@ntis.gov
Online order: https://classic.ntis.gov/help/order-methods/

ABSTRACT

MELCOR is an integrated thermal hydraulics, accident progression, and source term code for reactor safety analysis that has been developed at Sandia National Laboratories for the United States Nuclear Regulatory Commission (NRC) since the early 1980s. Though MELCOR originated as a light water reactor (LWR) code, development and modernization efforts have expanded its application scope to include non-LWR reactor concepts. Current MELCOR development efforts include providing the NRC with the analytical capabilities to support regulatory readiness for licensing non-LWR technologies under Strategy 2 of the NRC's near-term Implementation Action Plans. Beginning with the Next Generation Nuclear Project (NGNP), MELCOR has undergone a range of enhancements to provide analytical capabilities for modeling the spectrum of advanced non-LWR concepts. This report describes the generic plant model developed to demonstrate MELCOR capabilities to perform fluoride-salt-cooled high-temperature reactor (FHR) safety evaluations. The generic plant model is based on publicly-available FHR design information. For plant aspects (e.g., reactor building leak rate and details of the cover-gas system) that are not described in the FHR references, the analysts made assumptions needed to construct a MELCOR full-plant model. The FHR model uses a TRi-structural ISOtropic (TRISO)-particle fuel pebble-bed reactor with a primary system rejecting heat to two coiled tube air heat exchangers. Three passive direct reactor auxiliary cooling systems provide heat removal to supplement or replace the emergency secondary system heat removal during accident conditions. Surrounding the reactor vessel is a low volume reactor cavity that insulates the reactor with fire bricks and thick concrete walls. A refractory reactor liner system provides water cooling to reduce the concrete wall temperatures. Example calculations are performed to show the plant response and MELCOR capabilities to characterize a range of accident conditions. The accidents selected for evaluation consider a range of degraded and failed modes of operation for key safety functions providing reactivity control, the primary system decay heat removal and also a piping leak of the line to the coolant drain tank.

ACKNOWLEDGEMENTS

This work was funded by the NRC as part of the development and demonstration activities defined in the NRC Non-Light Water Reactor Vision and Strategy Volume 3: Computer Code Development Plans for Severe Accident Progression, Source Term, and Consequence Analysis [1]. The authors gratefully acknowledge the contributions from Jason Schaperow, Hossein Esmaili, and Don Algama of the US NRC for their valuable technical guidance.

The authors graciously acknowledge valuable support provided by Dallin Keesling on developing the direct reactor auxiliary cooling system model.

Friederike Bostelmann of Oak Ridge National Laboratories (ORNL) performed the FHR SCALE analysis and provided the radionuclide decay heat power, radionuclide inventory, and the core axial and radial power profile for this analysis. Robert Kile of ORNL evaluated the tritium production in the molten salt and the xenon poisoning reactivity feedback. The documentation of their analyses are in ORNL/TM-2021/2273 and is part of the same NRC-sponsored effort.

CONTENTS

LIST OF FIGURES

LIST OF TABLES

This page left blank

ACRONYMS AND DEFINITIONS

Abbreviation	Definition
AGR	Advanced Gas Reactor
ATWS	Anticipated Transient without SCRAM
AVR	Arbeitsgemeinschaft Versuchsreaktor
BWR	Boiling Water Reactor
COR	Core
CTAH	Coiled Tube Heat Heater
CV	Control Volume
CVH	Control Volume Hydrodynamics
DHX	DRACS Heat Exchanger
DOE	United States Department of Energy
DRACS	Direct Reactor Auxiliary Cooling System
FHR	Fluoride-Salt-Cooled High-Temperature Reactor
FL	Flow Path
FLiBe	Li_2BeF_4
FU	Fuel
HALEU	High-Assay Low Enriched Uranium
HGTR	High-Temperature Gas Reactor
HS	Heat Structure
IAEA	International Atomic Energy Agency
INL	Idaho National Laboratory
LMTD	Log-mean Temperature Difference
LOCA	Loss-of-Coolant Accident
LWR	Light Water Reactor
Mk1	Mark 1
MSR	Molten Salt Reactor
MST	Mechanistic Source Term
MX	Matrix
NGNP	Next Generation Nuclear Plant
NRC	United States Nuclear Regulatory Commission
NUEP	Nuclear Energy University Program
ORNL	Oak Ridge National Laboratory
PBMR	Pebble Bed Modular Reactor

Abbreviation	Definition
RF	Reflector
RN	Radionuclide
RRCLS	Refractory Reactor Cavity Liner System
SBO	Station Blackout
SFR	Sodium-cooled Fast Reactor
SS	Supporting Structure
TCHX	Thermosiphon-Cooled Heat Exchangers
TRISO	TRi-structural ISOtropic particle fuel
UCB	University of California Berkeley

1. INTRODUCTION

MELCOR is an integrated systems-level thermal hydraulics and source term code for reactor safety analysis [1]. It has been developed at Sandia National Laboratories for the United States Nuclear Regulatory Commission (NRC) since the early 1980s. Current MELCOR development efforts include providing the NRC with the accident analysis capabilities to support regulatory readiness for licensing non-light water reactor (non-LWR) technologies under Strategy 2 of the NRC's near-term Implementation Action Plans [2]. Beginning with the Department of Energy (DOE) Next Generation Nuclear Project (NGNP), MELCOR has undergone a range of enhancements to provide analytical capabilities for modeling the spectrum of advanced non-LWR concepts. A detailed description of the development process, including identification of technical gaps, is provided in NRC's "Non-Light Water Reactor (Non-LWR) Vision and Strategy, Volume 3 – Computer Code Development Plans for Severe Accident Progression, Source Term, and Consequence Analysis" (NRC ADAMS Accession No. ML20030A178). This report describes the generic MELCOR plant model developed to demonstrate MELCOR capabilities to perform fluoride-salt-cooled high-temperature reactor (FHR) safety evaluations.

The MELCOR FHR model is applied to provide an example of a mechanistic source term (MST) analysis. The scope of the MST demonstration project includes development and application of a MELCOR full-plant model using publicly-available references and data. The project also includes MST demonstration calculations for other non-LWR designs that will be documented in separate reports (e.g., a heat pipe reactor and a molten-salt-cooled pebble-bed reactor).

MELCOR characterizes the evolution of the accident from the early thermal-hydraulic response through the core heat up, including the release and transport of radionuclides from the primary system to the containment or confinement buildings and the environment. The code is a knowledge repository from decades of experiments and model development with a historical focus on LWR phenomenology. However, MELCOR has been extended with new models to address non-LWR technologies. The key MELCOR FHR models are discussed in Section 2.

MELCOR relies on the SCALE code system to provide the radionuclide inventories, kinetics parameters, power distributions, and decay heat, especially through the ORIGEN code. SCALE is a multi-disciplinary tool developed by Oak Ridge National Laboratory for the NRC to combine nuclear system simulation tools into one cohesive package [3]. SCALE provides a comprehensive, verified and validated, user-friendly tool set for nuclear data, criticality safety, reactor physics, radiation shielding, radioactive source term characterization, activation, depletion and decay, and sensitivity and uncertainty analysis under a software quality assurance program. Since the 1970s, regulators, licensees, and research institutions around the world have used SCALE for safety analysis.

The MELCOR FHR input model used for the MST analysis is based on a University of California, Berkeley (UCB) Mark 1 (Mk1) design [4]. The Mk1 design was funded by the DOE Nuclear Energy University Program (NEUP). The demonstration FHR input model development included (a) the MELCOR reactor system model based on the Mk1 design information, (b) incorporation of the SCALE inventory, axial and radial power profiles, decay heat tables, and reactivity feedback coefficients, (c) incorporation of TRISO fission product release model input, (d) development of a containment building based on the Mk1 design information, (e) the passive direct reactor auxiliary cooling system using the Mk1 design information, and (f) radionuclide tracking algorithms. Section 3 describes the FHR model used in the MST calculations.

The FHR MELCOR plant model is used to simulate a loss-of-coolant accident (LOCA), a station blackout (SBO) accident, and an anticipated transient without SCRAM (ATWS). The development of the input model identified gaps and uncertainties in design input data. Some exploratory calculations were performed to illustrate the impact of the uncertain parameters as well as variations in the safety system availability. The accident progression and the source term results are described in Section 4. A summary is presented in Section 5.

This report describes the MELCOR FHR full-plant deck and its application to select scenarios. In addition, this work was presented at a public workshop on September 14, 2021. The video recording and presentation material are available at the following links:

- Video – https://www.youtube.com/watch?v=YZDqCka_gm4
- Slides – SCALE MELCOR FHR slides ML21256A231 [5]

2. MELCOR FHR MODELING FEATURES

The MELCOR code is organized into "packages" that correspond to different groupings of reactor regions, physics, or other code functionalities. The balance of the plant is modeled using the building block components of control volumes, heat structures, and flow paths. These basic components are used to represent primary system, the reactor vessel, the reactor building or containment, and the secondary system, which will be described for the FHR demonstration model in the next section. These fundamental modeling features are used for all reactor types. A unique capability of MELCOR includes an integrated calculation of radionuclide release, transport, and deposition in any problem description or nodalization. The level of modeling detail or discretization is user-specified based on the objectives of the analysis. An example for the Mk1 FHR design is described in this report (i.e., the Mk1 design was developed by UCB in a DOE NEUP program [4]). The next subsections describe some of the key MELCOR models used in the FHR demonstration calculations and an overview of the calculation solution methodology.

2.1. MELCOR FHR-specific Models

Superimposed in the reactor core portion of the vessel nodalization are special models for pebble bed and prismatic FHR fuel modeling. The fuel description and associated physics are modeled in the "COR" package. The Mk1 COR modeling includes the representation of the reflectors, the pebbles containing the TRISO fuel, and the TRISO fuel. The MELCOR FHR COR package calculates the thermal response of the pebbles, the surrounding reflectors, the reactor fission power response (i.e., a point kinetics model), and the radionuclide release [6].

The MELCOR diffusional fission product release model calculates the radionuclide distribution and transport within the TRISO and pebbles. Any radionuclides reaching the surface of the pebble are released to MELCOR's Control Volume Hydrodynamic (CVH) package and tracked in the Radionuclide (RN) package for the subsequent transport and deposition. The COR package also calculates the radionuclide behavior during normal power operation. The scope of the modeling includes the amount (and species) of radionuclides generated in the fuel kernels (i.e., as specified by amounts provided by the SCALE code), the amount recoiled and diffused to the buffer layer, the amount diffused into or through the dense TRISO coating layers, the amount released from the kernels of particles with failed TRISO coating layers, and the amount which diffuses through the graphite pebble matrix (see Figure 2-1). A detailed description of the TRISO radionuclide behavior models is presented in Reference [6].

The MELCOR FHR COR package models the combined radiation and conduction heat transfer within the pebble bed. The special heat transfer model accounts for radiation and conduction through a packed bed (i.e., the Zehner-Schlunder-Bauer model with the Breitbach-Barthels modification to the radiation term [6]). The combined radiation and conduction model also predicts the radial and axial heat transfer to the surrounding reflectors. The radiation terms in the packed bed solution are only included when the molten salt has drained or boiled away. The pebble bed convective heat transfer model accounts for natural or forced convective heat transfer from a sphere as flow conditions evolve during the transient. The flow resistance through the pebble bed is based on an Achenbach modification to the porous bed flow resistance [6].

Postulated accident conditions in a FHR can lead to the ingression of air or steam into the core. Consequently, the COR package includes steam and air oxidation models. The steam oxidation correlation calculates the rate of oxidation as a function of the partial pressure of the steam and hydrogen adjacent to the graphite using a parabolic kinetics formulation. Similarly, the air oxidation model calculates the rate of oxidation as a function of the partial pressure of the oxygen adjacent to

the graphite. Both the steam and air oxidation correlations include a rate limit due to steam or oxygen diffusion towards the graphite surface. The chemical equilibrium of reaction products is specified using correlations for the relative extent of reactions producing carbon-monoxide gas versus carbon-dioxide gas.

Finally, MELCOR includes a point kinetics model for the core power evaluation during a transient. The kinetics equations are a function of the reactor's thermal power and the thermal power generated by the 6 groups of delayed-neutron precursors. The model includes generalized interfaces for reactivity feedbacks from the fuel, the moderator, the control rods, and the neutron sources.

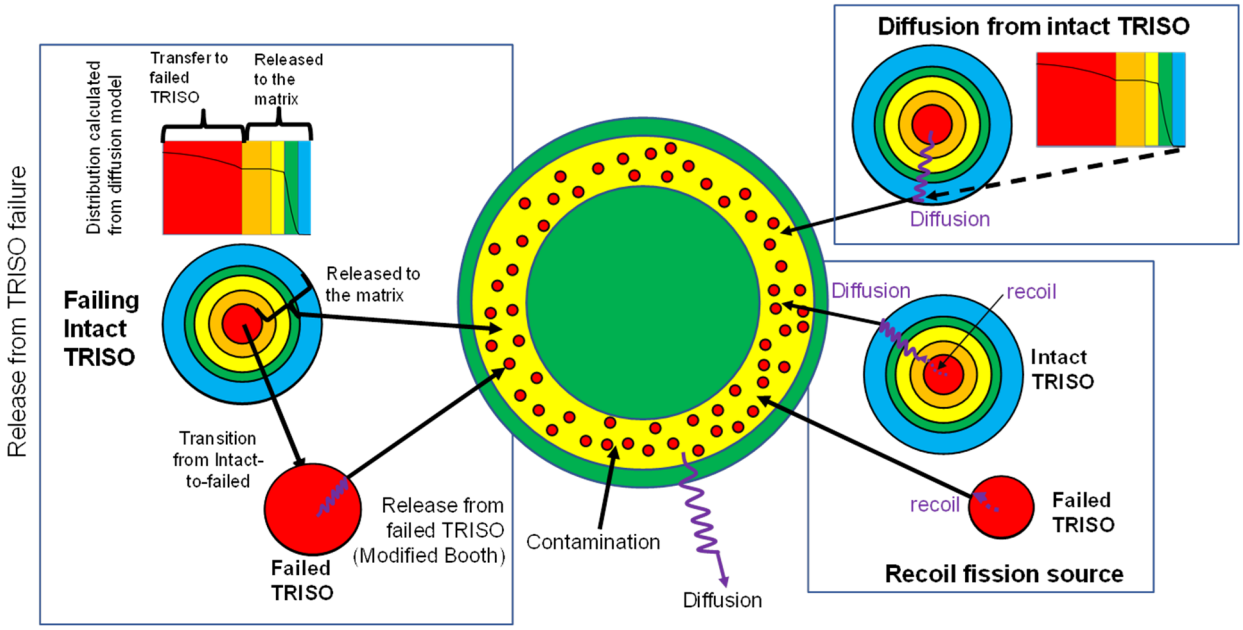

Figure 2-1 MELCOR FHR radionuclide release models.

2.2. MELCOR FLiBe Equation of State

The Mk1 fuel is cooled by the fluoride salt, or FLiBe (Li_2BeF_4). Consequently, a key component of the FHR simulation was the inclusion of FLiBe as the primary system fluid. The FLiBe equation of state was obtained from Idaho National Laboratory (INL) [7]. When simulating a FHR reactor, special input directives are used to identify FLiBe as primary fluid rather than water. MELCOR reads the FLiBe fluid properties database, which provides the specific volume (m^3/kg), the specific internal energy (J/kg), the coefficient of thermal expansion (1/K), isothermal compressibility (1/Pa), the specific heat capacity at constant pressure, c_P (J/kg-K), and the specific entropy (J/kg-K). The coefficient of thermal expansion and isothermal compressibility are determined using these properties.

A key enhancement implemented in the current project was an extrapolation to frozen conditions. FLiBe salt solidifies at approximately 460°C. During the evolution of a transient, the temperature may reach the freezing point. To allow frozen conditions without significant architectural changes, a thermodynamic undercooling model was added to the equation of state, such that the liquid and

vapor phases may exist below the freezing temperature. A modeling option was added to perform an extrapolation of the thermodynamic properties when the fluid drops below the freezing temperature.[1] The pressure is exponentially extrapolated as a function of temperature from the freezing values defined by the equation of state down to 0°C with a small but non-zero pressure. The positive minimum pressure value was chosen such that an extrapolated pressure was always positive, regardless of the freezing state point. Internal energy is linearly extrapolated as a function of temperature from the freezing values, which is consistent with a constant specific heat model. The entropy is linearly extrapolated as a function of the natural logarithm of the temperature from the freezing values, which is consistent with an incompressible substance model. The new extrapolations along with MELCOR's thermodynamic variables of density and temperature permit the calculation of all other needed values and derivatives to effect a solution.

2.3. MELCOR FHR Solution Methodology

A MELCOR FHR accident simulation is performed in a single calculation and includes four stages (see Figure 2-2). The model is initialized to the normal plant operating conditions in Stage 0. Any discrepancies in the user-specified initial conditions are updated as the model's boundary conditions drive the temperature, pressure, and flow conditions to the desired normal operating conditions. Special steady state acceleration models allow the long-term convergence of the heat structure temperature distribution prior to the start of the calculation.

Stage 1 of the steady state calculates the long-term radionuclide transport and releases during normal operating conditions. The accelerated diffusion model predicts the steady state distribution of the various radionuclides through the TRISO finite volume computational meshes for the intact TRISO, the failed TRISO, and the pebbles for each COR cell in the reactor core. At the completion of the long-term steady state diffusion phase of the accident, the long-term radionuclide release from normal operations exists in the primary system, including the long-term fission product deposition onto the reactor vessel and primary system piping and walls. The steady state diffusion model also generates the long-term distribution of the non-released radionuclides between the fuel kernel, the various TRISO layers, and the pebble matrix.

For the Mk1 demonstration problem, the long-term steady state diffusion model was partially disabled. The Mk1 FHR includes an exchangeable charcoal filter at the inlet to the heat exchangers. The charcoal filters clean up any operational releases of non-gaseous radionuclides and the cover-gas system is expected to remove any gaseous radionuclides. Therefore, the long-term operational releases into molten salt were not included. However, the accelerated steady state model still establishes the long-term distribution of the non-released radionuclides between the fuel kernel, the various TRISO layers, and the pebble matrix. Only the second portion of projecting long-term releases from the pebbles into the molten salt was disabled. Consequentially, the demonstration calculations only included the radionuclides released from the pebbles during the accident and did not include any operational releases.

Stage 2 is the non-accelerated transient diffusion phase. The transient diffusion phase of the simulation shifts the physics models for the radionuclide transport to transient calculations. The transient calculations end all time accelerations and activates the TRISO failure modeling in anticipation of Stage 3.

[1] The thermodynamic property routines would fail, which stopped the calculation prior to this modeling enhancement.

Finally, Stage 3 is driven by imposed boundary conditions for the accident simulation (e.g., a SBO). The transient radionuclide diffusion models and TRISO failure models respond to the new conditions and calculate the radionuclide releases in the final phase of calculation.

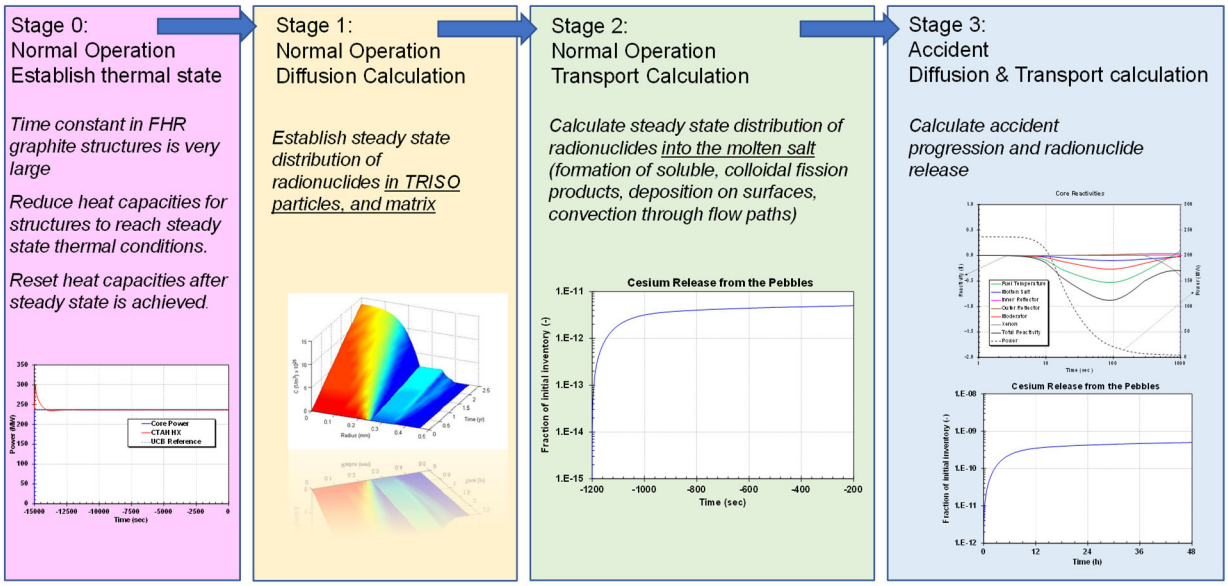

Figure 2-2 MELCOR FHR solution methodology.

3. MODEL DESCRIPTION

The development of the MELCOR Mk1 input model was primarily based on the Mk1 FHR design report [4]. The information from Reference [4] was supplemented with additional geometric information available in Anselmo Cisneros's dissertation [8]. The information available in References [4] and [8] is relatively comprehensive and included the scope of the primary system and the surrounding containment. Nevertheless, some dimensions were not available and therefore estimated from available drawings. Some of the important estimated values included the direct reactor auxiliary cooling system (DRACS) elevations, the loop elevations, and most containment geometric dimensions. The component or compartment interconnections, many component elevations, and the operation of the cover-gas system required assumptions, which are described in the analyses. Also not available in the design reports were the containment leakage rate, the containment inter-compartment leakage areas, and the primary system over-pressurization protection system. Assumptions or estimations for the missing parameters were made to complete the demonstration model. Finally, the radionuclide inventory and decay heat tables were obtained from a supporting SCALE analysis by ORNL [9]. ORNL also provided the axial and radial power profiles and the reactivity feedbacks.

The input model included the vessel, the primary system loops, the DRACS, the refractory reactor cavity liner system (RRCLS), the secondary heat removal, and the containment. Other key inputs included the SCALE-predicted radionuclide inventory, the radionuclide decay heat, and axial and radial power profiles from ORNL, diffusivities for the TRISO fission product release models, reactivity feedbacks from ORNL for the MELCOR point kinetics model, the radionuclide tracking algorithms, and an accident control system.

Section 3.1 provides an overview of the Mk1 FHR. Following the overview, the reactor vessel, the primary and secondary systems, and the containment building nodalizations are described in Section 3.2. The DRACS heat removal system is described in Section 3.3. ORNL provided the radionuclide inventory and the decay heat, which is described in Section 3.4. The FHR uses TRISO fuel in a graphite pebble. The radionuclide release model is described in Section 3.5. ORNL also provided reactivity feedbacks for the point kinetics point model, which is described in Section 3.6. Finally, the steady state initialization is described in Section 3.7.

3.1. Mk1 Overview

The Mk1 reactor system schematic is shown in Figure 3-1. The reactor vessel interfaces with the hot leg to the hotwell. There are two salt pumps located in the hotwell that circulate the molten salt through the coiled tube air heaters (CTAHs) and then back to the vessel. There are three DRACS decay heat removal systems connected to the vessel (i.e., only one shown). The secondary side of the CTAHs is a high-pressure, Brayton air cycle that powers the gas turbines. Some of the key Mk1 design parameters are summarized in Table 3-1.

The Mk1 reactor vessel nodalization was developed using the detailed geometry in Reference [8] with the geometry and technical information in Reference [4]. The reactor vessel is 12 m high with a diameter of 3.5 m. The volume of molten salt in the core and refueling chute is 7.2 m^3. There is 3.38 m^3 of molten salt in the other reactor internals, for a total of 10.58 m^3. The Mk1 vessel includes a downcomer, center and outer reflectors, a refueling chute at the core exit, and an outlet collector leading to the hot leg (see Figure 3-2). The top half of the vessel is largely open and includes the DRACS heat exchangers (DHX) and the defueling wells. The hot leg and two cold leg penetrations are located near the top of the vessel.

The Mk1 vessel uses an annular pebble core geometry. The pebbles are approximately half the size of a high temperature pebble bed gas reactor (e.g., Reference [10]) and have an inner carbon core with an annular fueled region near the outside of the sphere. UCB cites that the small pebble design increases the pebble surface per unit volume of fuel, decreases the thermal diffusion length to the fluid, and permits a high power density with relatively low fuel temperatures. The core power density is 22.7 MW/m^3, which is significantly higher than a PBMR (4.8 MW/m^3) but much lower than a current-generation pressurized water reactor (105 MW/m^3).

There are both fueled and unfueled pebbles in the core. Each fueled pebble has approximately 4730 TRISO fuel kernels imbedded in a spherical shell between the 25 mm and 29 mm radii. A 25 mm graphite core is at the center with a 1 mm graphite coating on the outer surface of the pebble. There are 470,000 fueled pebbles and 218,000 unfueled pebbles in the core and the defueling chute. The unfueled pebbles are located in the periphery of the core and next to the outer reflector, which reduces the fast-neutron fluence damage of the outer reflector. The center reflector can be replaced but the outer reflector is designed to last for the life of the reactor [8].

The circulating molten salt (976 kg/s) enters the vessel through two cold legs that are attached to the vessel downcomer. The molten salt flows downward through the annular downcomer to the lower plenum region below the reactor core. The 2.8 cm wide downcomer is formed between the stainless steel vessel wall on the outer surface and the stainless steel core barrel on the inner surface. 70% of the molten salt enters the passageways in the center reflector and 30% enters directly into the fueled region of the core through the passageway between the center and outer reflector. The new and recirculated fuel pebbles enter the core from the fueling machine into the passageway between the center and outer reflectors. The molten salt in the center reflector exits through flow passages along the length of the reflector and mixes with the molten salt entering from the bottom of the vessel. The passageway between the center and outer reflector widens into the uniform portion of the core. The molten salt flows axially and radially outward through the core and discharges into exit passageways along the outer reflector. A portion of the molten salt flows through the defueling chute before mixing with the bulk of the core exit flow. The molten salt rises upwards through a duct riser that connects to the hot leg.

The flow from the hot leg goes to the hotwell, which contains two salt pumps. The hotwell has a free surface that connects to the argon cover-gas system. It is assumed the cover-gas system maintains a 34.5 kPa (5 psig) overpressure. Each salt pump connects to a hot leg that flows to the four inlet headers for the CTAH (see Figure 3-3). The molten salt flows through the annular tube bundle formed by coiled tubes as the air flows radially outward over the tubes (see Figure 3-4). The coiled tube's outer diameter is 6.35 mm with a tube thickness of 0.889 mm. The net tube length is 252,697 m per CTAH. The molten salt exits the 13,680 coiled tubes to the four exit headers from the CTAH, which connect to the cold leg.

The cold legs connect to the bottom of a tall cylindrical standpipe (i.e., see Figure 3-5). At the bottom of each standpipe is a drain tank that is isolated from the primary loop by a passive freeze valve. The molten salt rises through the two standpipes and enters the vessel through separate vessel penetrations.

The secondary side of the Mk1 connects to a high-pressure Brayton air cycle with a gas turbine. The high-pressure air from the turbine enters the bottom of each CTAH vessel at 418.5°C. The hot air flows into the center of the coiled tube bundle, flows radially outward across flow across the coiled tubes, and then exits upward from the CTAH at 670°C. The air flowrate through each CTAH is 418.5 kg/s at a nominal pressure of 18.76 bar.

Reference [4] includes a description of the Mk1 containment but very few dimensions. The containment is designed with a low leakage boundary around the reactor cavity, which surrounds the reactor. There are bellows on the piping penetrations from the reactor cavity that accommodate the thermal expansion and also limit leakage. If the space pressurizes, then there is over-pressure pathway to a compartment in the lower containment.

The other key containment compartments around the reactor system in the cylindrical portion of the lower containment are shown in Figure 3-6. The hotwell with the salt pumps and the standpipes are located in an adjacent compartment to the reactor. The two CTAHs are placed in separate compartments. The secondary system piping from the CTAHs passes into a large rectangular room outside the cylindrical boundary of the shield building. Much of the balance of the plant is located in the above-grade portion of the rectangular room with the CTAH inlet and outlet piping.

A tall shield dome is located above the reactor cavity and the surrounding compartments in the lower containment (see Figure 3-7). The tall cylindrical shield building provides protection against external events (e.g., tornados). Reference [4] describes the low-leakage reactor cavity as the primary containment boundary with the shield building functioning as a secondary containment. The shield building dilutes and delays any release of beryllium and radioactive contamination. The refueling floor of the shield building is used for fuel transfer work associated with the on-line refueling. The three thermosiphon-cooled heat exchangers (TCHX) for the DRACS are also located in the shield dome. The DRACS condenser cooling chimneys are attached to the outside of the shield dome.

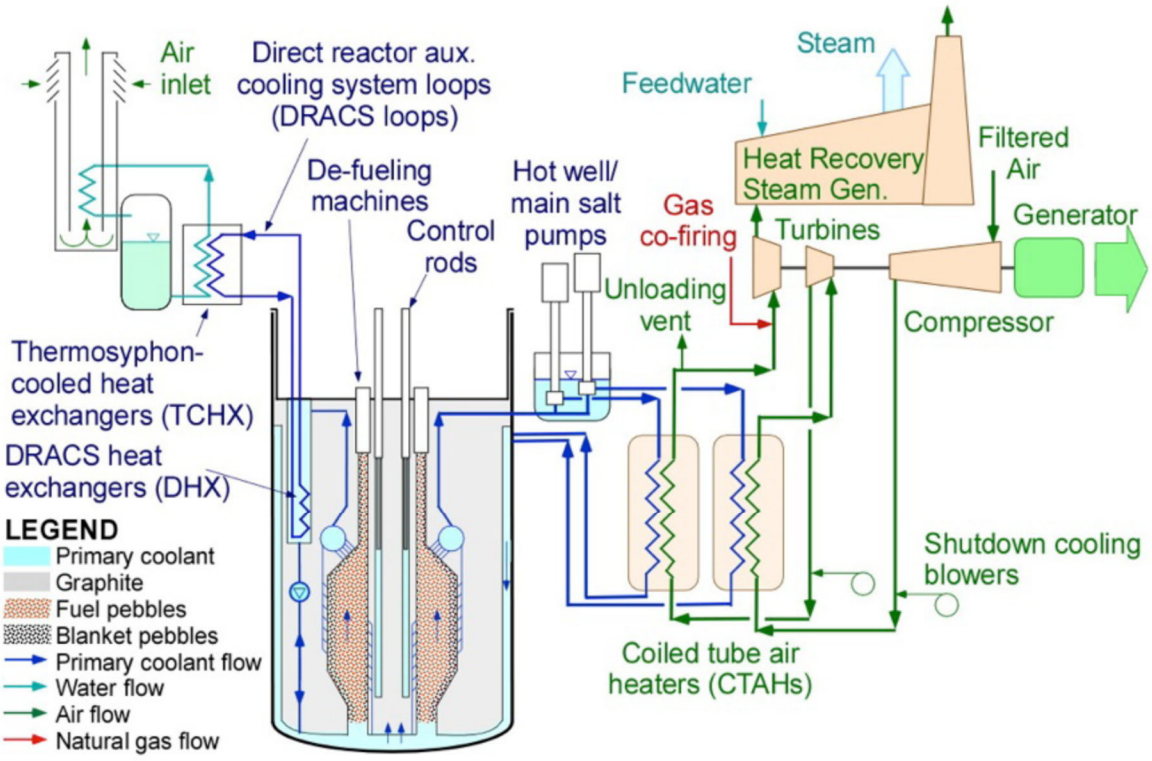

Figure 3-1 Mk1 reactor system schematic [4].

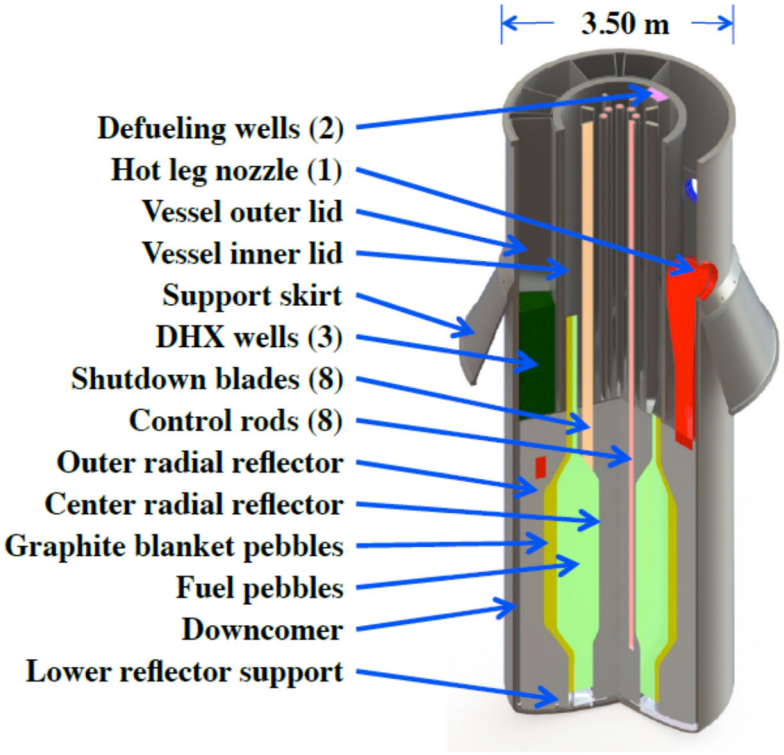

Figure 3-2 Mk1 reactor vessel [4].

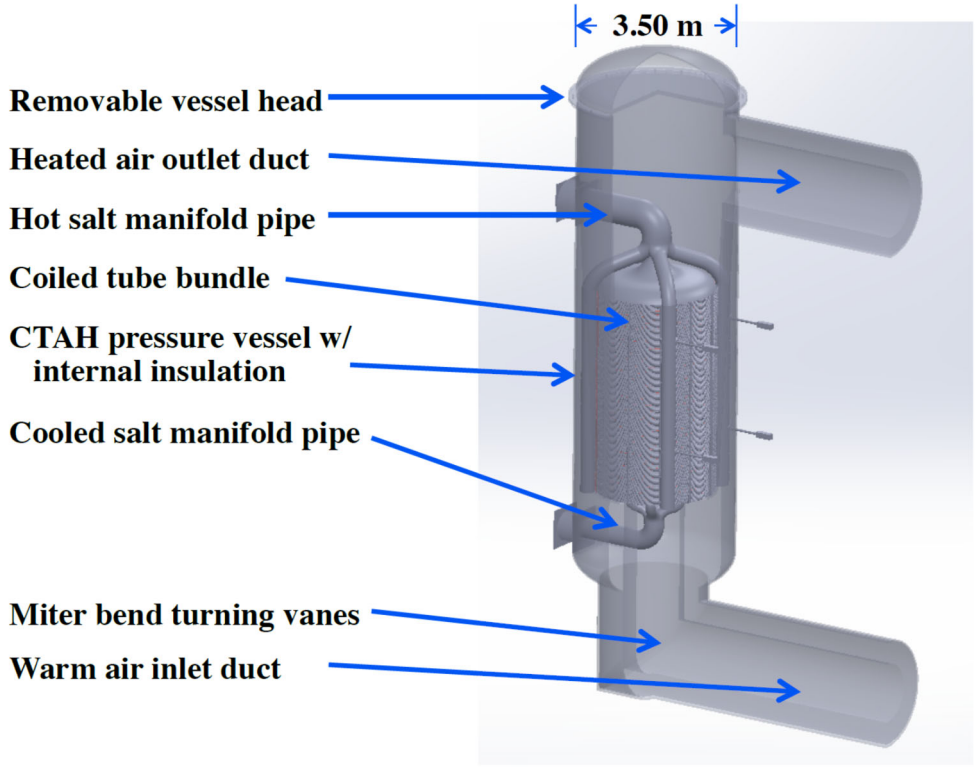

Figure 3-3 Mk1 CTAH interior design [4].

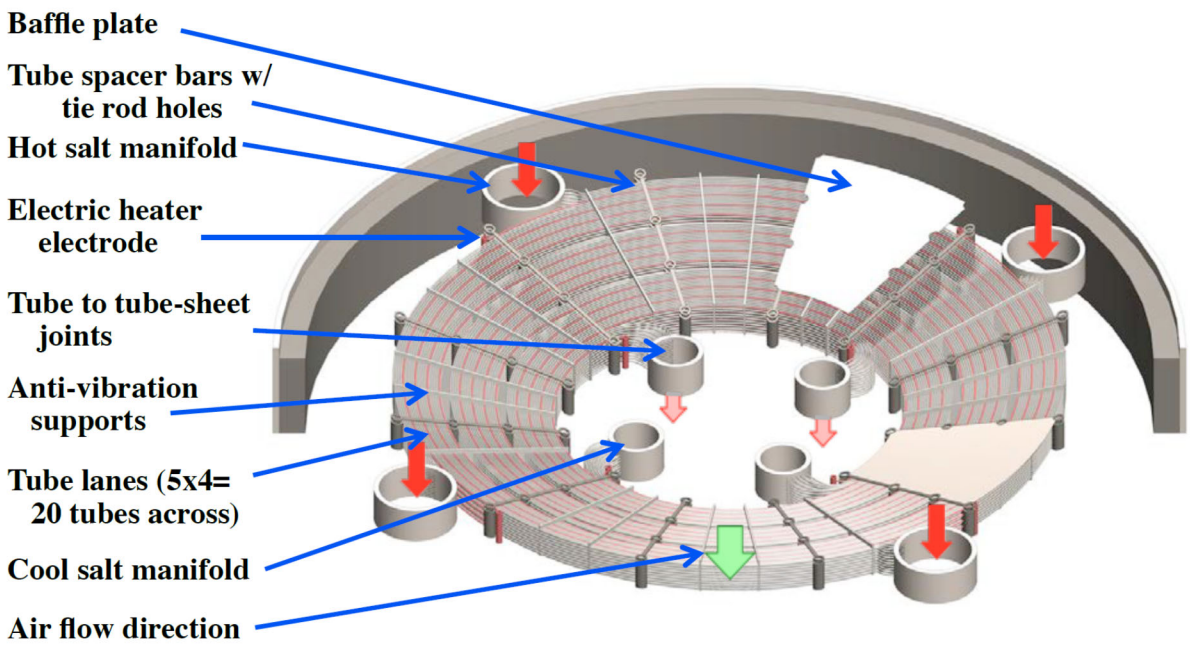

Figure 3-4 Mk1 CTAH cross-section [4].

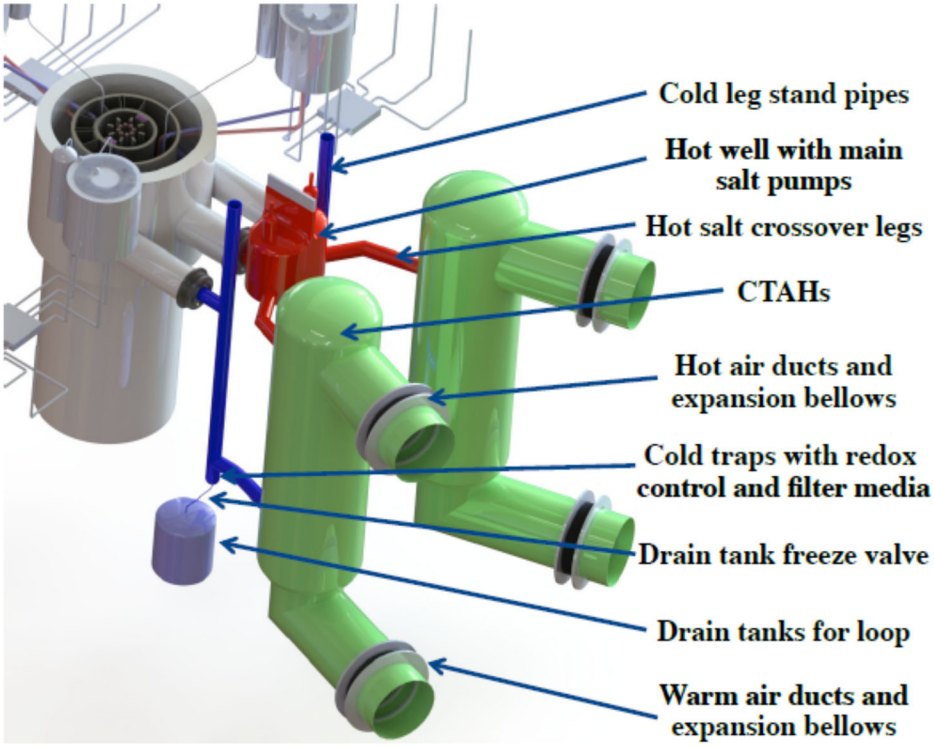

Figure 3-5 Mk1 isometric showing the standpipes and drain tank [4].

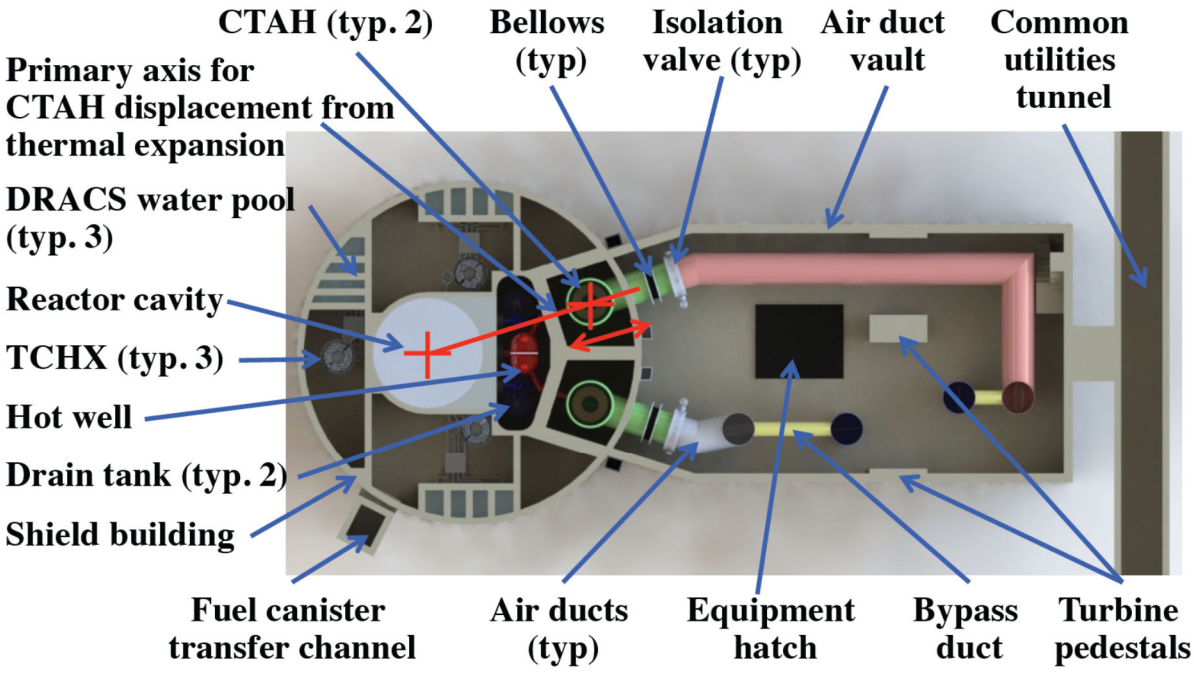

Figure 3-6 Plan view of Mk1 reactor building [4].

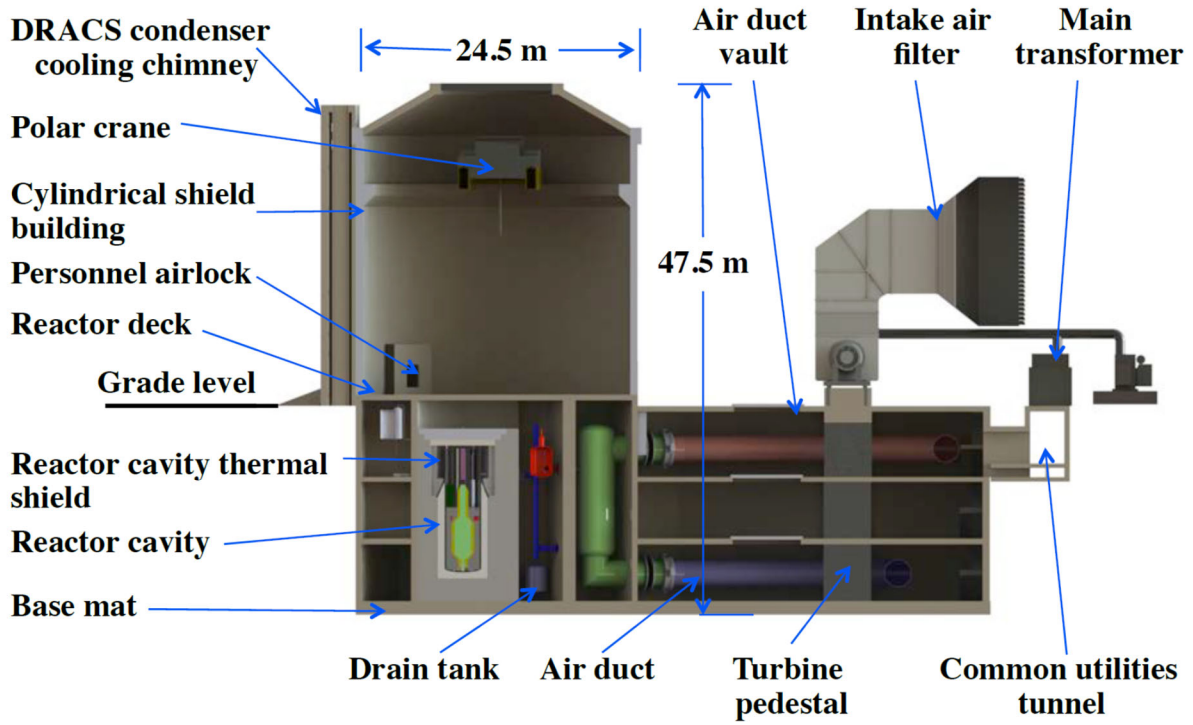

Figure 3-7 Elevation view of Mk1 reactor building [4].

Table 3-1 Key Mk1 design parameters [4].

Parameter	Value
Reactor thermal power	236 MW
Coolant	FLiBe (Li_2BeF_4)
Reactor vessel pressure	Near atmospheric [#]
Reactor inlet temperature	600°C
Reactor outlet temperature	700°C
Core power density	22.7 MW/m^3
Uranium enrichment	19.9% (HALEU) *
Average pebble lifetime	1.4 yr
Average pebble void fraction	40%
Fueled pebbles in core and chute	470,000
Graphite pebbles in the core and chute	218,000
Number of pebbles	~452,000
Target burn-up	180 MWd/kgHM

Notes:
[#] No specific value was cited. The demonstration calculation assumed that the cover gas system maintained a 5 psig over-pressure from the containment.
[*] High-Assay Low-Enriched Uranium (HALEU)

3.2. Mk1 Model Nodalization

The Mk1 model nodalization and key modeling features for the reactor vessel, the primary and secondary systems, and the containment are described in Sections 3.2.1 through 3.2.3, respectively.

3.2.1. Reactor Vessel Nodalization

The modeling of the Mk1 reactor vessel in MELCOR utilizes building block inputs from multiple packages. The building block approach to the input provides flexibility to model alternate reactor designs with varying levels of resolution. A key set of vessel input comes from COR package, which includes the structures in the core and the radionuclide release model. The Mk1 COR nodalization has 11 axial levels and 8 radial rings. The COR package includes the contents of the vessel from the lower head on the bottom to the top of the graphite reflectors and the inside surface of the core barrel on the outer radius. The COR package calculates the structural material response and interfaces with the CVH, FL, and Heat Structure (HS) packages. The reactor vessel COR, CVH, and FL nodalization is shown in Figure 3-8. The cylindrical coordinates for the COR axial and radial boundaries are shown with the light blue lines. The CVH and FL nodalization is superimposed onto the COR nodalization with spaces between the control volumes (CV) to show the connecting flow paths.

The fuel pebbles are fed into the bottom of the core and float upwards to the defueling chute at the outlet of the core. The core uses a mixture of fueled and unfueled graphite pebbles. CV-161 models the unfueled graphite pebble inlet and CV-131 is the fueled pebble inlet region. The fueled pebbles are located in COR Rings 2 through 7, which includes CV-131 through CV-138, CV-143 through

CV-148, CV-153 through CV-158, CV-162 through CV-168, and CV-173 through CV-178. The unfueled pebbles continue upwards from CV-161, CV-162, CV-173, and CV-180. There are both unfueled and fueled pebbles in CV-162, CV-173, CV-181, and CV-182. COR Axial Level 11 extends to the top of the central and outer reflectors. The pebble behavior above the top of the refueling reflectors (i.e., top of COR Level 11 and CV-182) is not modeled. The pebble power reduces to decay heat levels above the top of the reflectors. The pebbles in the defueling chute exit into the refueling devices and are transported out of the vessel for a burn-up assessment.

The center reflector is located in COR Ring 1. The center reflector has passageways (i.e., CV-105) for molten salt flow from the lower plenum (CV-100). The molten salt from the center reflector enters the core through FL-113 through FL-118 and contributes to radial flow across the core toward the outlet passageway (i.e., CV-190). Some of the molten salt flow exits through the refueling chute (CV-185), which combines with the flow in the vessel exit header (CV-190).

The vessel downcomer (CV-115) is located outside the COR nodalization. COR Ring 8 ends at the outer edge of the outer reflector. The outer reflector conducts across the small gap between the outer reflector and the stainless steel core barrel. The stainless steel core barrel and the outer vessel wall are modeled in the HS package.

The vessel region above the top of the core (i.e., above axial core Level 9) is largely empty (see Figure 3-2). As described above, the core exit piping and the downcomer pass through this region. The three DRACS heat exchangers are also located in his region, which will be described in Section 3.3.

The fueled COR cells contain the graphite pebbles with the TRISO fuel. The pebbles are modeled with the fuel (FU) component for the uranium portion of the fuel kernel, graphite for the non-fueled portion of the pebble as an additional FU component, and matrix (MX) for the pebble inner and outer shell. The mass of uranium in a COR cell's fuel component is determined by calculating the number of pebbles in the cell (i.e., equal to the total cell volume times the packing fraction, 0.6, divided by the volume of one pebble), which is multiplied by the number of TRISO fuel particles per pebble (i.e., 4730) and the mass of uranium per fuel particle (i.e., 1.5 g). The additional fuel graphite mass is calculated by determining the number of pebbles in the cell and multiplying by the mass of graphite in the fueled and center core regions of one pebble, which is equal to the mass of pebble minus the outer graphite shell and uranium mass. Finally, the matrix (MX) mass is calculated by multiplying the number of pebbles in the cell by the mass of graphite in the shell around a pebble, which is equal to the volume of the shell times the density of graphite.

The surrounding graphite reflectors are modeled using the COR reflector (RF) component. The mass of the reflector is equal to the volume of the COR cell minus the volume of the flow channels and plenums. The stainless steel support skirt below the center and outer reflectors is modeled using the supporting structure (SS) component.

MELCOR includes core degradation models for the collapse and rubblization of unsupported components (e.g., structures that thermally yield or melt). Consequently, every intact component in a MELCOR COR model must be supported. Some supporting structures (i.e., modeled with a trivial, non-yielding stainless steel component) are used to support graphite reflector (RF) components that do not have a reflector component in the cell below or a supporting structure in the same cell. This was a work-around requirement to satisfy the reflector component support requirements for the

unusual core geometry of the Mk1. These required supporting structures had no impact on the heat transfer or thermal capacity of the COR cell.

The radial and axial heat transfer within the pebble bed is modeled using a modified version of the Zehner-Schlunder-Bauer unit cell approach. In a FHR, the most important component of heat transfer between cells is convection of the surrounding molten salt. However, the Zehner-Schlunder-Bauer model calculates any conduction between core cells when the pebbles are covered with molten salt. If the molten salt boils or drains away, then the main component of the heat transfer is radiation. The model was recently updated to seamlessly include the radiation terms in the Zehner-Schlunder-Bauer correlation when the local fluid fraction goes to zero. The COR default axial and radial radiation model is disabled in lieu of this modeling approach.

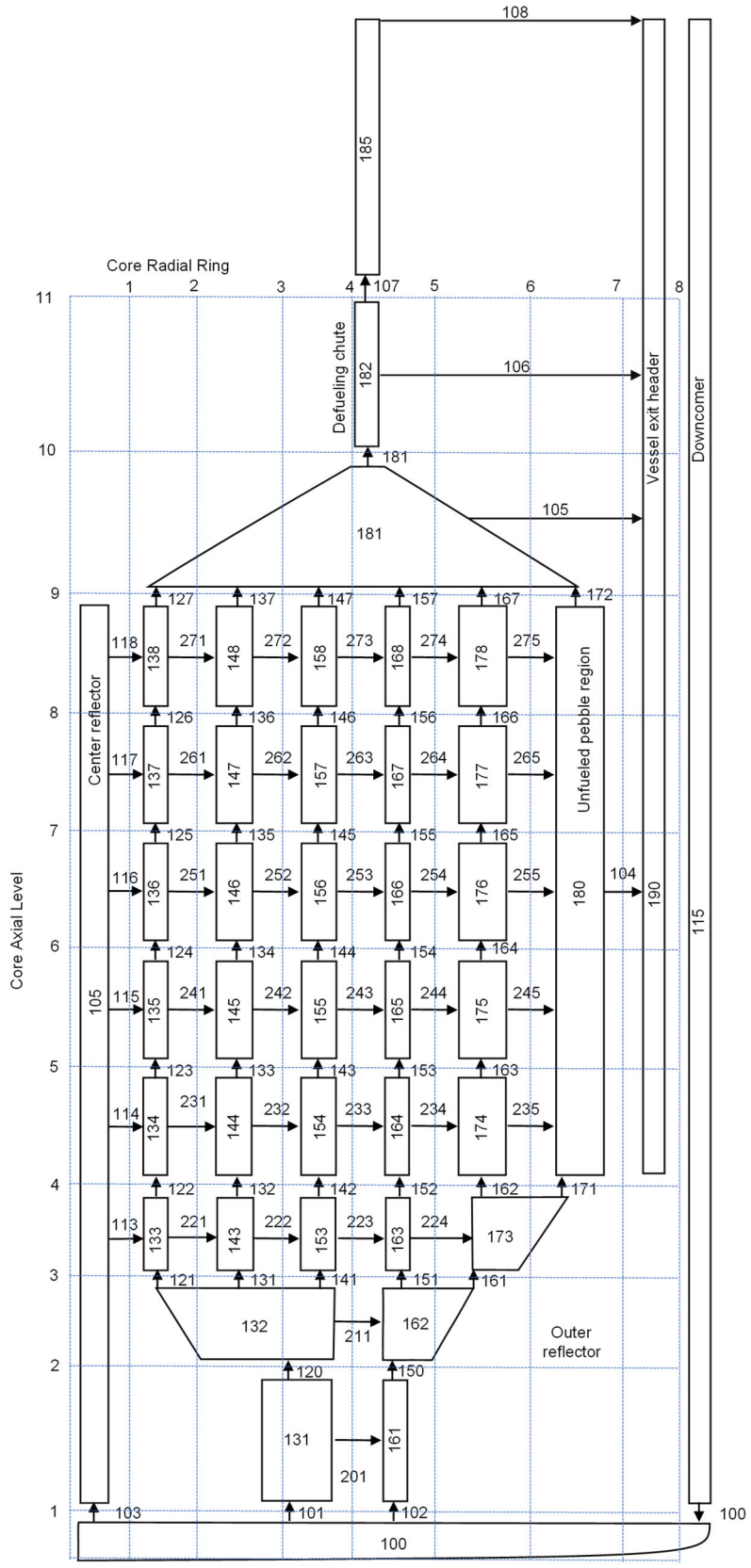

Figure 3-8 Mk1 reactor vessel and COR nodalization.

3.2.2. Primary and Secondary System Nodalization

As described in Section 3.1, the Mk1 has one hot leg leaving the vessel but two recirculation loops after the hotwell. The nodalization schematic of the Mk1 recirculation loop is shown in Figure 3-9. The hot and cold leg connections to the vessel are FL-300 and FL-345/FL-346, respectively. There are free liquid surfaces in the hotwell and the two standpipes. The fluid volume associated with the CTAH inlet and exit headers are included in CV-310 and CV-330, respectively for Loop 1. Similarly, CV-311 and CV331 include those regions for Loop 2, respectively. The tubes on the primary side of the CTAH are modeled with a single CV (i.e., CV-320 and CV-321) but include a log-mean temperature difference (LMTD) heat transfer calculation for the complex geometry. The secondary side was not active during the demonstration scenarios but the model included provisions for the emergency blowers.

All piping and the CTAHs include heavy insulation to minimize the heat loss. Reference [4] cites that the external surface of the piping insulation remain below 60°C. The insulation properties and the containment compartment heat removal during the steady state are specified to establish the specified insulation surface temperature. The containment heat removal was not active after the start of the transient.

The cover gas system is shown with the blue lines in Figure 3-9. Many of the specific design details of the system were unknown. Reference [4] describes a liquid overflow connection from the standpipes to the hotwell for level swells. During steady state calculations, the gas pressure in the standpipes was greater than the hotwell due to the pressure rise from the salt pumps. As the connection was implemented (i.e., FL-391 and FL-397), there was a bypass flow from the standpipes to the hotwell. To eliminate level swings with pump operation, the liquid flow path was disabled during pump operation and the cover gas connection to the standpipes was isolated. These choices are a reflection of not having the system design details rather than a criticism or identification of a design flaw.

Another area of modeling uncertainty was the vessel over-pressurization system. Reference [4] describes that the hotwell and standpipe gas spaces provide overpressure protection in rapid transients (e.g., a CTAH tube failure). However, there were no specific details of the system response in a sustained pressurization (e.g., during unmitigated heating events with sustained salt expansion and vaporization). It is assumed that the cover gas system is connected to a compartment in the lower containment for over-pressurization protection (i.e., see CV-395 on Figure 3-9). Reference [4] identified this compartment as providing over-pressure protection if the reactor cavity pressurized. The hotwell cover-gas is connected to the same compartment in the lower containment for over-pressure protection. It is also assumed that the compartment had a rupture disk that opened when the compartment pressure exceeded 68.9 kPa (10 psig).

With all the interconnections included with the cover gas system, a number of strange flow patterns occurred that were judged unlikely during transient conditions. However, there was not enough information to model the intentions of the designers. Consequently, a number of flow paths were disabled or included check valves to prevent reserve flows. First, the standpipe to the cover-gas line was closed while the salt pumps were running but allowed to open after the pumps tripped. A check valve was also added to these lines to prevent reverse flow from the overflow compartment. Second, the liquid overflow lines from the standpipe to the hotwell were always disabled except in some sensitivity studies after the salt pumps tripped. Third, a check valve was placed in the overpressure line from the reactor cavity to the overflow compartment to prevent flow into the reactor cavity. Finally, a constant-pressure argon source was connected to the overflow compartment, which

maintained a constant pressure during normal operations. The argon supply to the overflow compartment was isolated following the pump trip signal or a loss of power.

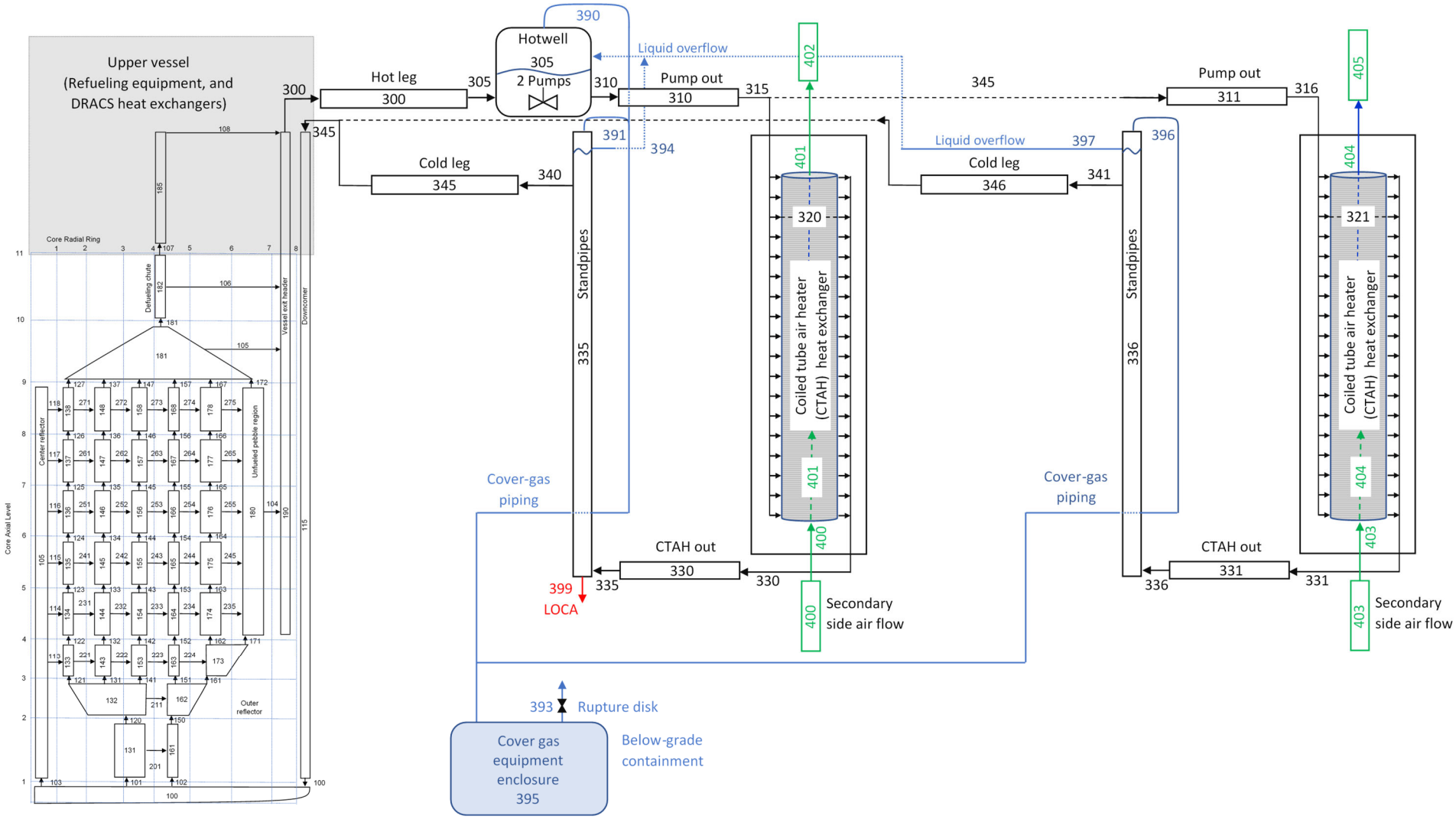

Figure 3-9 Mk1 primary and secondary CVH and FL nodalization.

3.2.3. Containment and Reactor Cavity Cooling System Nodalization

The Mk1 containment nodalization is shown in Figure 3-10. The scope of the containment building includes the lower cylindrical portion of the containment with the reactor cavity, the hotwell compartment, the CTAH compartments, and the bulk of the lower containment. The cylindrical shield dome above lower containment is represented with CV-14. The cover gas enclosure compartment (i.e., CV-395 in Figure 3-9) is located in the below-grade CV (i.e., CV-13) The rectangular building with the CTAH piping in the below-grade region and the turbine are not included in the scope of the containment model.

The leakage area between the various compartments was estimated. Two leakage pathways (1.5 in^2 each) are included from the reactor cavity to the pump room (FL-10 and FL-11) and another leakage pathway goes to the bulk of the lower containment (FL-12). The remaining connections in the lower containment flow paths are assumed to be unrestricted (i.e., 155 in^2 each). However, all the leakage pathways are adjustable for sensitivity studies. There are high and low leakage connections from the CTAH compartment to the turbine side the of the reactor building (FL-16 and FL-17). Since the turbine-side of the reactor building is not modeled, any leakage through FL-16 and FL-17 goes to the environment. High and low leakage paths are also connected to the shield dome (FL-19 and FL-20).

The overall leakage from the building is assumed to be similar to the reactor building around a boiling water reactor (BWR), which is 100% leakage per day at a design pressure of 0.25 psi. The effective leakage area of the four leakage paths to the environment is 8.7 in^2, which is evenly split between the two leakage paths into the turbine-side of the reactor building around the CTAH piping and the two leakage paths from the shield dome.

A key attribute of the Mk1 containment design is the refractory reactor cavity liner system (RRCLS). The space between the reactor vessel and the cavity stainless steel liner is filled with low conductivity, refractory blocks. The refractory blocks insulate the stainless steel reactor vessel from the surrounding concrete structure. The reactor cavity concrete walls and floor have a steel liner with an imbedded water cooling system. The reactor cavity cooling subsystem circulates through the liner to maintain the concrete behind the liner plate at nominally 30°C. The design includes provisions for an emergency water supply during beyond design basis accident conditions. A second design feature of the RRCLS is a small free volume for leak protection. If the reactor vessel leaks, the minimum vessel level remains above the top of fuel located in the defueling chute.

The refractory liner blocks, the cavity liner with the water cooling system, and the concrete are modeled as a multi-composition heat structure. The cavity liner cooling system is modeled using an energy sink. The energy sink maintains the nominal concrete temperature during the accelerated steady state calculation at approximately 30°C. The availability of the liner cooling system during accidents is specified in the control system. However, sensitivity studies showed that the RRCLS did not impact the accident progression. Consequently, it is assumed available in all demonstration calculations.

When there is an external wind, one flow path is assigned to the upwind side of the building and the other is on the downwind side. The guidance for modeling building wind effects is described in Reference [11]. External wind effects are included in DOE facility safety analyses, where there are not strong driving forces for fission product release. The wind increases building infiltration and exfiltration rates. Both an upwind infiltration location and a downwind location were included in the

model. The wind effects are modeled as an additional Bernoulli pressure term in the flow path pressure solution,

$$dP_{Wind} = \frac{1}{2}\rho C_p v^2$$

where,

dP_{Wind}	Bernoulli wind pressure term, (Pa)
ρ	Fluid density, (kg/m^3)
C_p	Building coefficient, (-)
v	Wind velocity, (m/s)

The values for building coefficients are typically obtained using computational fluid dynamics evaluations. When wind effects are modeled in the demonstration calculations, generic values were obtained from the American Society of Heating, Refrigerating and Air-Conditioning Engineers (ASHRAE) handbook (see Table 3-2 [12]).

Sensitivity studies with and without wind did not shown any appreciable differences in the containment leakage (i.e., the containment pressurization from the FliBe vaporization negated any wind-aided infiltration and exfiltration). Consequently, the demonstration calculations described in this report assumed that there was no wind.

Table 3-2. Typical building coefficients [12].

Wind Direction	Value
Upwind	0.7
Downwind	-0.4
Side and top of the building	-0.35

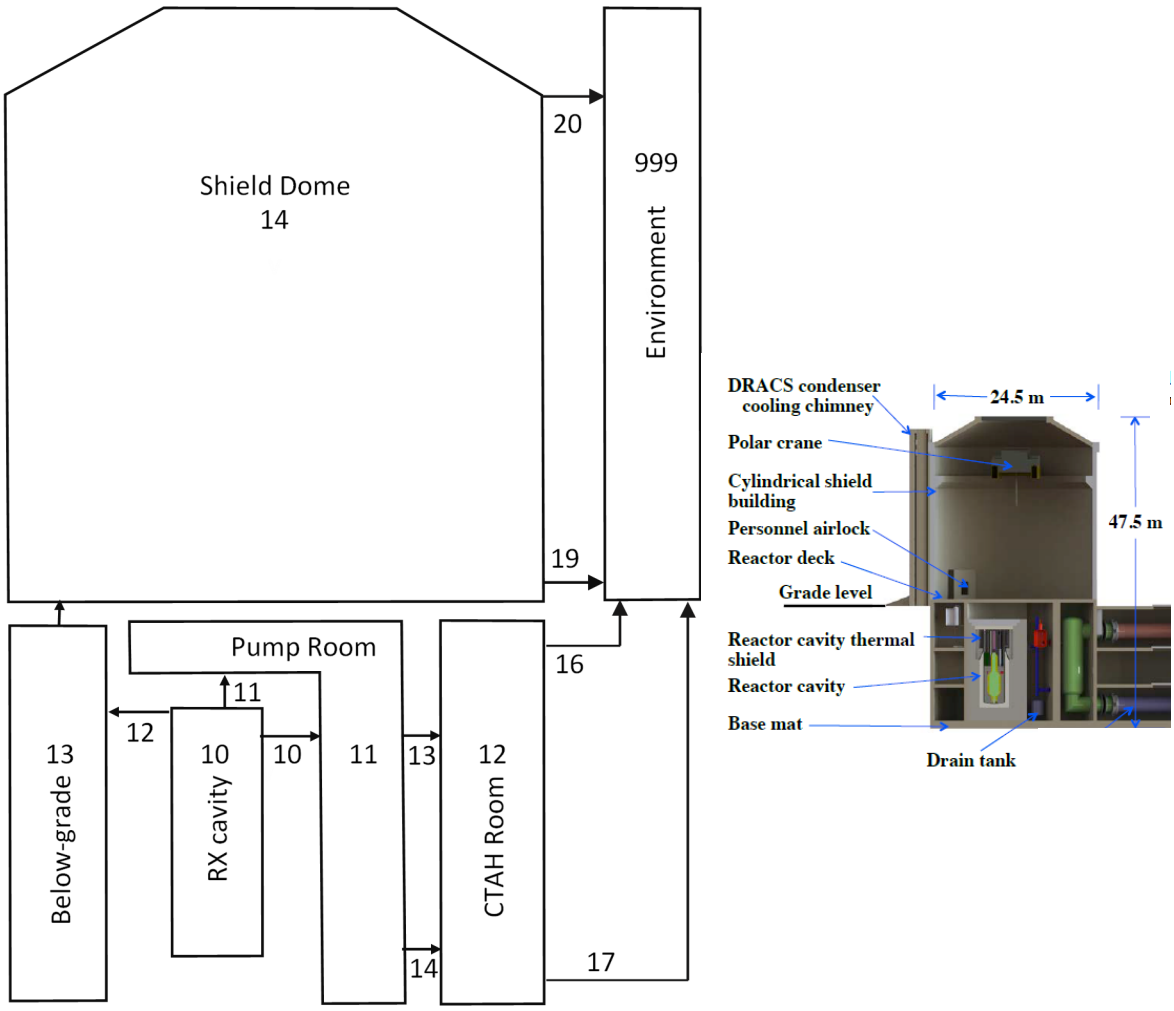

Figure 3-10 Mk1 containment nodalization and Mk1 containment elevation view [4].

3.3. DRACS vessel heat removal system

The DRACS provides the emergency passive heat removal for the Mk1. Each of the three DRACS units is designed to remove 1% of the reactor thermal power. A DRACS unit consists of the primary system loop, a secondary-side salt loop, a water loop, and an air natural circulation loop through the chimneys on the exterior of the shield building as the ultimate heat sink. The DRACS schematic is shown in Figure 3-11, and the DRACS air chimneys can be seen in Figure 3-7. The vessel fluid entering the primary side of the DHX (i.e., CV-500) connects from the vessel exit piping (i.e., FL-510) near the top of the vessel. The fluid is cooled by a molten salt loop on the secondary side of the DHX (i.e., CV-530). The cooled salt exists through the bottom of the DHX and discharges into the vessel lower plenum. A ball valve (i.e., FL-520) in the primary-side molten salt return piping isolates the system when the salt pumps are running. The ball valve is held closed by the differential pressure across the core developed from salt pumps and passively opens when the pumps trip.

The secondary salt loop also uses molten salt. The molten salt in the secondary salt loop is heated and rises from the DHX to the TCHX (i.e., CV-540). The molten salt flows circularly downward

through 234 THCX tubes (i.e., CV550). Running between the molten salt tubes are 2050 water-filled tubes (i.e., CV-610). The hot salt tubes radiate and convect to the water-filled tubes, which causes the water to heat and boil. The water loop circulates to a heat exchanger in a chimney connected to the outside of the shield building. The hot water tubes heat the air in the chimney, which creates a natural draft of air. The heat removal from the air natural circulation flow condenses the steam to form the condensate return back to the TCHX (i.e., CV-560).

The water and chimney air loops are not explicitly modeled in the MELCOR Mk1 model. The water tubes are modeled with an appropriate heat structure representing the 2050 tubes. The water is modeled as a constant temperature energy sink at the water boiling point (i.e., 100°C). Degraded operation of the water loop is simulated by degrading the heat transfer across the THCX air gap.

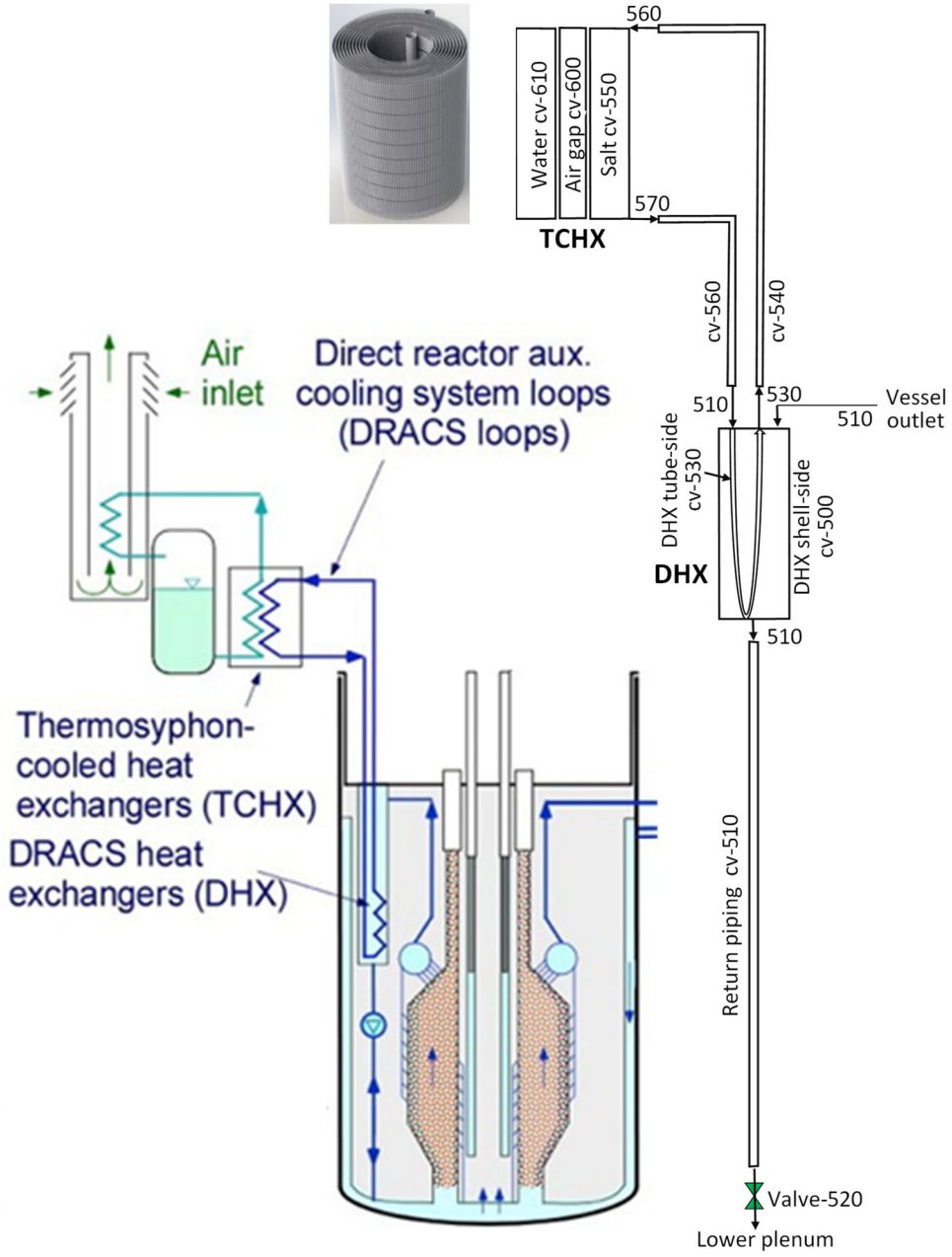

Figure 3-11 DRACS schematic and nodalization [4].

3.4. Radionuclide Inventory and Decay Heat Input

The radionuclide inventory and decay heat inputs were calculated using SCALE at ORNL [9]. ORNL performed an analysis to determine the equilibrium burn-up that approximated the continuous refueling of a Mk1. The oldest pebbles in the core circulated eight times over 1.4 years for a maximum 180 GWd/MTU burn-up. The corresponding inventory and decay heat were calculated based on the mix of eight groups of pebbles in continuous circulation. The data provided from SCALE includes separate decay heat curves for each radionuclide class in Table 3-3. The radionuclide class inventories are shown in Table 3-4, and the overall decay is shown in Figure 3-12. For the airborne transport of iodine, 95% of the iodine is assumed to form cesium iodide aerosols and 5% remains in a gaseous (i.e., I_2) form.

Table 3-3 MELCOR radionuclide classes

Class	Class Name	Chemical Group	Representative Element	Member Elements
1	XE	Noble Gas	Xe	He, Ne, Ar, Kr, Xe, Rn, H, N
2	CS	Alkali Metals	Cs	Li, Na, K, Rb, Cs, Fr, Cu
3	BA	Alkaline Earths	Ba	Be, Mg, Ca, Sr, Ba, Ra, Es, Fm
4	I2	Halogens	I_2	F, Cl, Br, I, At
5	TE	Chalcogens	Te	O, S, Se, Te, Po
6	RU	Platinoids	Ru	Ru, Rh, Pd, Re, Os, Ir, Pt, Au, Ni
7	MO	Early Transition Elements	Mo	V, Cr, Fe, Co, Mn, Nb, Mo, Tc, Ta, W
8	CE	Tetravalent	Ce	Ti, Zr, Hf, Ce, Th, Pa, Np, Pu, C
9	LA	Trivalents	La	Al, Sc, Y, La, Ac, Pr, Nd, Pm, Sm, Eu, Gd, Tb, Dy, Ho, Er, Tm, Yb, Lu, Am, Cm, Bk, Cf
10	UO_2	Uranium	UO_2	U
11	CD	More Volatile Main Group	Cd	Cd, Hg, Zn, As, Sb, Pb, Tl, Bi
12	AG	Less Volatile Main Group	Ag	Ga, Ge, In, Sn, Ag

Table 3-4 Mk1 radionuclide class masses.

MELCOR RN class	MELCOR Class Mass (kg)
Noble Gases (Xe)	12.70
Alkali Metals (Cs)	6.73
Alkaline Earths (Ba)	5.63
Halogens (I)	0.44
Chalcogens (Te)	1.14
Platinoids (Ru)	7.27
Early Transition Elements (Mo)	8.87
Tetravalent (Ce)	46.52
Trivalents (La)	16.28
Uranium (U)	616.79
More Volatile Main Group (Cd)	0.14
Less Volatile Main Group (Ag)	0.20

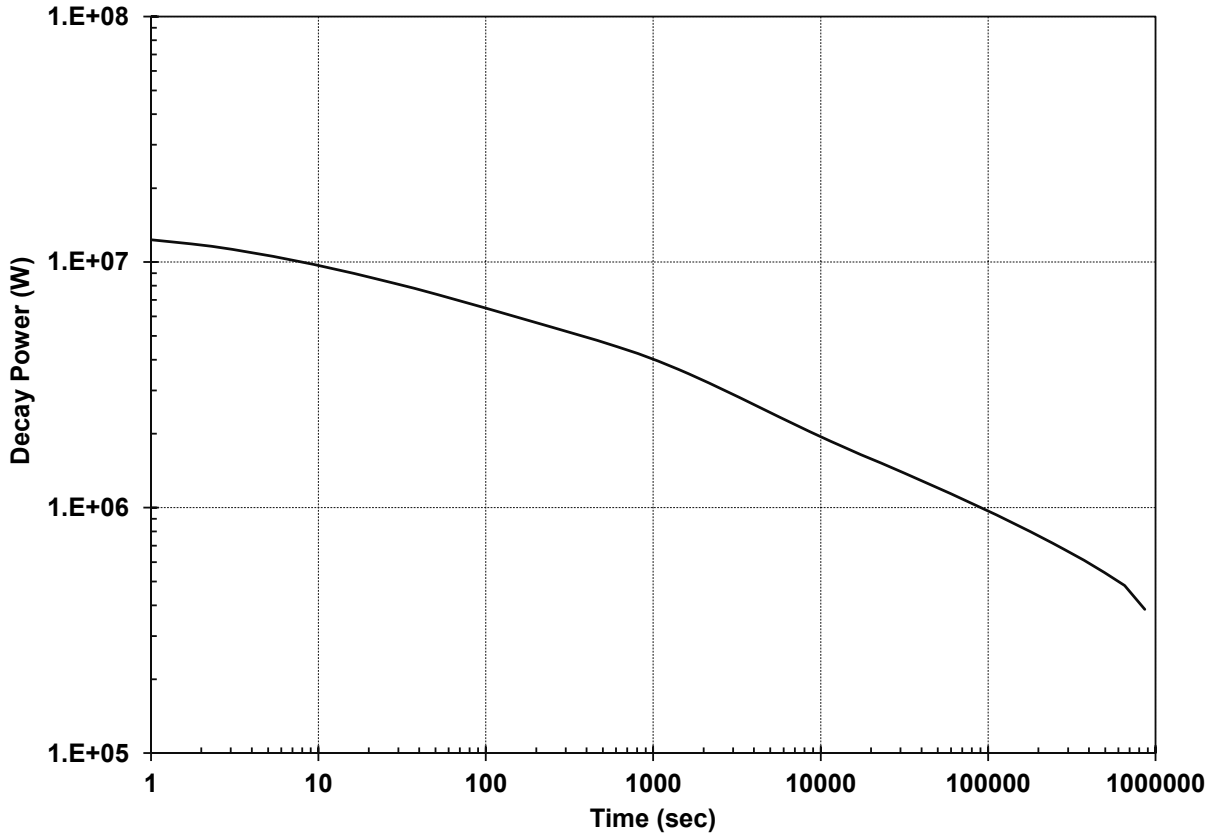

Figure 3-12 Mk1 decay heat curve.

3.5. Fission Production Release

The input required for the diffusional fission product release model is described in Section 3.5.1. The diffusional fission product release model calculates the radionuclide distribution and transport within the TRISO particles and pebbles. The scope of the diffusional release model includes the radionuclide release into the fluid surrounding the pebbles. By default, any radionuclides released into molten salt remained in the fluid. However, the MST accident progression included the boil-off of the molten salt. Consequently, the late phase of the accident included fission product releases directly from the pebbles to the salt vapor. In one sensitivity calculation, the new pool fission product chemistry and release model was used, which permits a more detailed evaluation of fission product behavior in the molten salt. The new pool fission product chemistry and release model is described in Section 3.5.2.

3.5.1. Fission Production Release from the TRISO

The MELCOR fuel diffusivity model calculates the release of fission products from the TRISO-fuel pebbles in the core. Figure 2-1 shows the key processes included in the model. The model calculates the distribution of the fission products generated and released during normal power operation and during an accident. The steady state distribution of fission products generated in the fuel kernels (i.e., set to the values provided by SCALE) includes the amount recoiled and diffused to the buffer layer, the amount diffused through the dense coating layers, the amount released from the kernels of particles with failed coating layers, and the amount which diffuses through the pebble graphite matrix (e.g., see Figure 2-1 for various types of radionuclide release). Following radionuclide release from the pebbles to the surrounding fluid, the MELCOR RN model calculates the transport and deposition of fission products in the reactor system and reactor building.

The MELCOR fuel diffusivity release model includes important phenomena for fission product behavior in FHRs [13]. The model considers two types of TRISO particles: those with intact coating layers and those with failed coating layers (e.g., see the intact TRISO layer schematic in Figure 3-13). A small fraction (i.e., 10^{-5}) of the fuel particles is modeled as initially failed due to manufacturing defects. The fraction of failed particles during accidents or transients can be specified using MELCOR's temperature-based, empirical correlation (i.e., the TRISO failure correlation). However, there are provisions for user-specified model. The demonstration calculation used the default temperature-based correlation, which was developed from German post-irradiation failure testing.

For intact TRISO, the fission products released from the fuel kernel accumulate in the buffer; for failed particles, the fission products go directly to the graphite matrix. The release and transport of the condensable (metallic) and non-condensable (gaseous) fission product releases are calculated using diffusion-based models. The diffusion calculation determines the distribution of the fission products between the kernel and the various TRISO layers, and the amount released from failed particles. There are also contributions to fission products from uranium contamination in the graphite matrix, which is specified to be a very small fraction of the total fuel inventory (i.e., 10^{-6}).

A key input for the MELCOR diffusivity model is the radionuclide-specific diffusivity data. The International Atomic Energy Agency (IAEA) published a comprehensive review of TRISO fuel performance and fission product behavior in gas-cooled reactors (i.e., Reference [14]). The objectives of the IAEA international cooperative research program were to review and document the status of the experimental data base and of the predictive methods for gas-cooled reactor fuel performance and fission product behavior; and to verify and validate methodologies for the prediction of fuel performance and fission product transport. The participants included institutions

from Germany, Japan, the United States, Russia, China, France, and the United Kingdom. There are limited diffusivity data for radionuclide transport through TRISO fuel. The key measured radionuclides are cesium, krypton, strontium, and silver. Appendix A of the IAEA report provided a comprehensive set of diffusivity data. Table 3-5 summarizes the data. Although there were no reported data for the buffer region between the kernel and the inner pyrolytic carbon layer, a recommended value was provided. It was also suggested the values for krypton would be appropriate for iodine gas.

The fuel kernel diffusivity data used in the demonstration calculations were based on a UO_2 kernel in the TRISO particles. However, the Mk1 design specifies a $UC_{1.5}O_{0.5}$ kernel, which is generically identified as a UCO kernel. The UO_2 data was used for two reasons. First, there was no UCO kernel diffusivity data in the IAEA TECDOC. The diffusivity data for alternate kernels compositions was very limited at the time of the IAEA report. Furthermore, a recent review of diffusivity data from INL also recommends using UO_2 kernel diffusivity data due to a lack of UCO data [15]. The second reason is consistency with the TRISO failure model. The TRISO failure curve (see Figure 3-14) is inherently connected to the fuel kernel composition. A UCO failure curve has not yet been developed. Consequently, any increases in accuracy with UCO diffusivity data are not complimented with a UCO TRISO failure curve. For these reasons, UO_2 kernel diffusivity data and the associated TRISO failure curve are used in the demonstration calculation. UCO kernels are preferred in US due to performance benefits at higher burnups. The UCO kernels form less carbon monoxide gas, which is an important contributor to the failure of the TRISO silicon carbide layer [16].

The MELCOR Mk1 fuel diffusivity release model tracked 5 elements (i.e., cesium, krypton, strontium, silver, and iodine). It was assumed that iodine transported the same as krypton. The remaining radionuclide classes were modeled using MELCOR's CORSOR-Booth radionuclide release scaling factors. The CORSOR-Booth model for radionuclide release was validated to experimental results from the light-water reactor VERCORS experiments and benchmarked to Phebus data [17]. Although there are inadequate data to adjust the release coefficients for the TRISO fuel pebbles, LWR scale factors were used as a surrogate to estimate additional radionuclide contributors to the accident source term. The LWR scaling factors are shown in Table 3-6. The LWR radionuclide class scaling factors are applied to chemically similar elements in the various radionuclide classes shown in Table 3-3. The LWR scaled release factors in Table 3-6 and radionuclide class definitions in Table 3-3 are presented to illustrate code capabilities rather than an endorsement of their appropriateness for TRISO-based systems. As more TRISO diffusivity data becomes available, then the new elements can be added to the fuel diffusivity release model and the elements in the associated radionuclide classes (i.e., Table 3-3) can be appropriately adjusted.

A TRISO failure model is built into the MELCOR code (see Figure 3-14) but can be replaced using user-input [6]. MELCOR's default failure curve was developed from a statistical analysis of the post-irradiation testing of primarily German AVR TRISO fuel up to 1800 °C. The curve was developed using UO_2 TRISO fuel. However, the FHR uses UCO TRISO. As discussed above, the UO_2 TRISO failure curve was used due to a lack of UCO kernel diffusivity data and an associated failure curve.

Finally, regarding ongoing research and manufacturing improvements for TRISO fuel, Reference [16] provides a summary of recent TRISO fuel qualification experiments from the DOE Advanced Gas Reactor (AGR) fuel development and qualification program. The AGR data are showing improvements in UCO TRISO performance versus UO_2. Whereas the ^{134}Cs release from UCO during the tests has been relatively low (i.e., $\leq 2 \times 10^{-4}$ after 300 h at 1600°C and $\leq 2 \times 10^{-3}$ after 300 h at 1800°C), the ^{134}Cs releases from UO_2 were significantly higher with peak release fractions reaching ~10^{-2} and ~10^{-1} at 1600 °C and 1700°C, respectively. At lower temperatures, the

radiation-enhanced damage grain-boundary diffusion is important for the release of metallic radionuclides such as cesium, europium, and strontium [18]. As the new data are generated, improved inputs for the fission product release from UO_2 and UCO TRISO and an associated TRISO fuel failure curve can be easily incorporated in the MELCOR TRISO diffusivity release model.

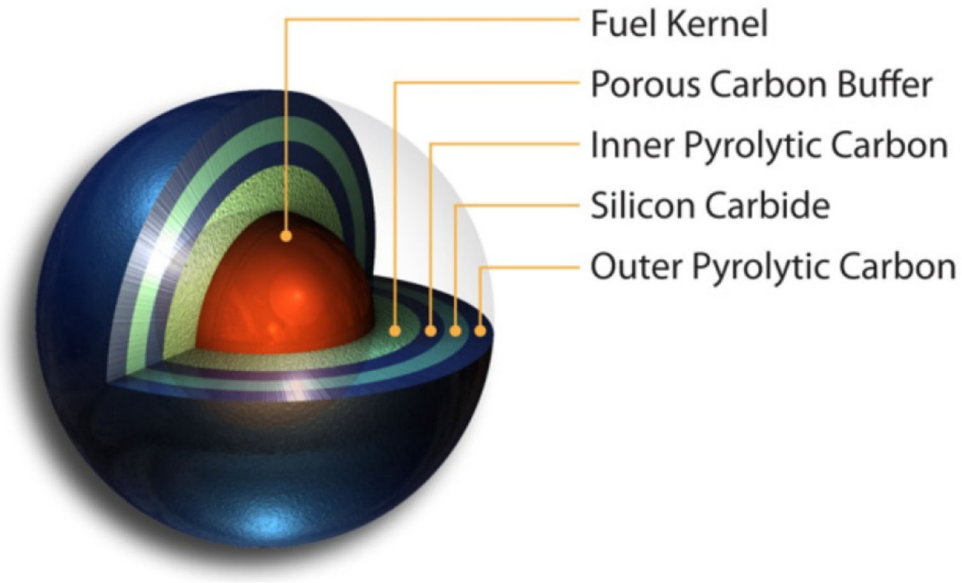

Figure 3-13 TRISO fuel particle layer identification [19].

Table 3-5 Diffusivities used in the Mk1 model [14]

Layer	FP Species							
	Kr		Cs		Sr		Ag	
	Do,i (m^2/s)	Qi (J/mole)	Do,i (m^2/s)	Qi (J/mole)	Do,i (m^2/s)	Qi (J/mole)	Do,i (m^2/s)	Qi (J/mole)
Fuel kernel	$1.3x10^{-12}$	126000.0	$5.6x10^{-8}$	209000.0	$2.2x10^{-3}$	488000.0	$6.7x10^{-9}$	165000.0
Buffer	$1.0x10^{-8}$	0.0	$1.0x10^{-8}$	0.0	$1.0x10^{-8}$	0.0	$1.0x10^{-8}$	0.0
PyC	$2.9x10^{-8}$	291000.0	$6.3x10^{-8}$	222000.0	$2.3x10^{-6}$	197000.0	$5.3x10^{-9}$	154000.0
SiC	$3.7x10^{+1}$	657000.0	$7.2x10^{-14}$	125000.0	$1.2x10^{-9}$	205000.0	$3.6x10^{-9}$	215000.0
Matrix Carbon	$6.0x10^{-6}$	0.0	$3.6x10^{-4}$	189000.0	$1.0x10^{-2}$	303000.0	1.6	258000.0
Str. Carbon	$6.0x10^{-6}$	0.0	$1.7x10^{-6}$	149000.0	$1.7x10^{-2}$	268000.0	1.6	258000.0

The coefficients above are used to calculate the local diffusivity using an Arrhenius type equation as a function of temperature.

$$D = \sum_i D_{o,i} \exp\left(\frac{Q_i}{RT}\right)$$

where,

- i is the index when multiple coefficients are specified (i=1 in demonstration calculations)
- $D_{o,i}$ is the pre-exponential factor [m^2/s]
- Q_i is the activation energy [J/mol]
- T is the local temperature [K]
- R is the universal gas constant [J/mol-K]

Table 3-6 CORSOR-Booth radionuclide release scaling factors [6].

Class	Scaling Factor
Te	0.64
Ru	2.5e-3
Mo	6.25e-2
Ce	4.0e-8
La	4.0e-8
Cd	0.25

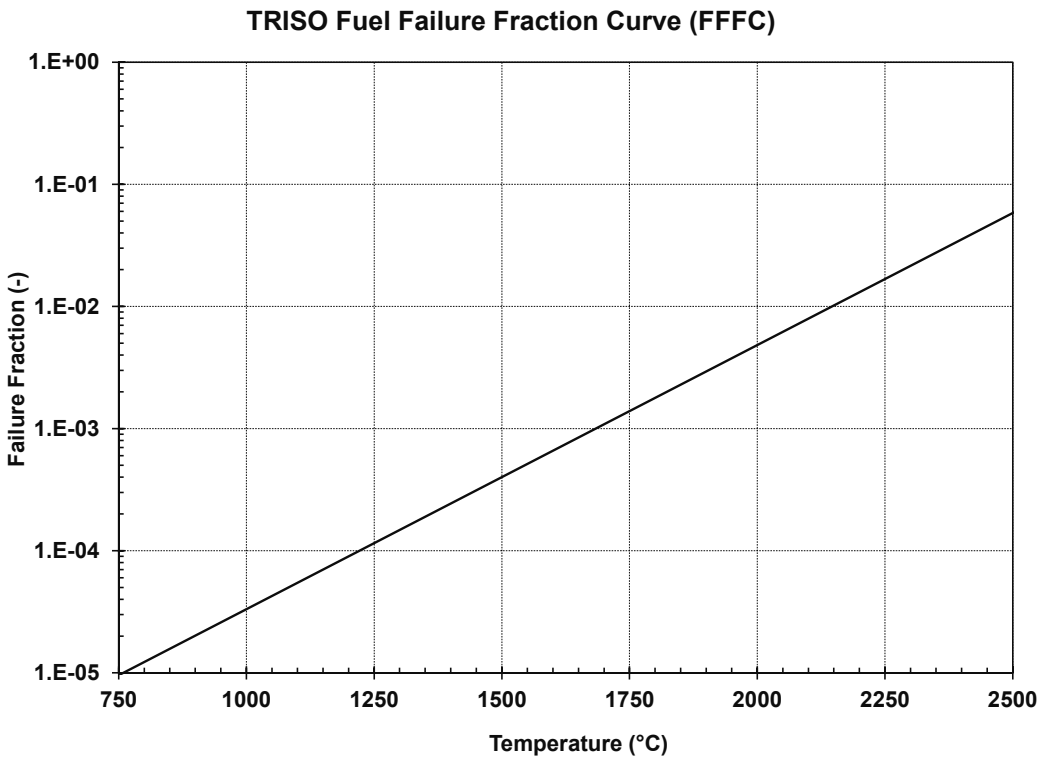

Figure 3-14 TRISO fuel failure fraction curve.

3.5.2. Fission Product Release from the Molten Salt

The MST demonstration calculations are based on a leak in the piping between the bottom of a standpipe and the connecting drain tank (see Figure 3-5). The LOCA calculations without DRACS heat removal were extended to include the boiloff of the molten salt in the vessel, which exposed the pebbles in the core to only salt vapor. Without the surrounding liquid molten salt, the fueled pebbles heated and the subsequent radionuclide releases from the pebbles went into the salt vapor. However, any fission product releases prior to the fuel uncovery were assumed to be retained in the molten salt. A new pool fission product chemistry and release model has been developed for MELCOR that was demonstrated for the first phase of a FHR LOCA. The new model was used to examine the cesium fission product release from the molten salt pool to the salt vapor prior to the fuel uncovery.

The new pool fission product chemistry and release model was initially developed for molten salt reactors (MSRs) that have flowing fuel (and fission products) in the liquid. However, the generalized framework is also applicable for the Mk1 FHR, chloride high-temperature fast reactors, and sodium-cooled fast reactors (SFRs). The pool fission product chemistry model uses the Thermochimica Gibbs free energy minimization routine to determine equilibrium chemical forms. Form-wise transfer models move fission products to appropriate states and locations, including the release to the vapor (see Figure 3-15).

The form-wise transfer is accomplished in three steps, given the state of fission products in five forms in the salt, and the presence of a gas space in the control volume. At the beginning of a time step, the fission products can be in forms 1 to 5 as: (1) salt-soluble, (2) salt-insoluble, (3) residing at

the surface of the liquid salt pool, (4) deposited on structures, and (5) as a vapor in small bubbles in the liquid salt. Some chemical species may be in more than one form.

The calculation progresses as follows. First, Thermochimica calculates the soluble, insoluble, and gaseous distribution at equilibrium conditions. With the appropriate thermochemical database, Thermochimica provides the solubility and vapor pressure of species as a function of temperature and composition. The Gibbs free energy of the system includes nonideal solution effects. Thus, the activity coefficient is not set at one, which is the case for ideal solutions.

The second step performs the form-wise transport calculations. In this step, the insoluble fission products in the salt are modeled as colloidal particles that migrate to and deposit on surfaces. The colloid particles may contain fission products, corrosion products, and abraded graphite particles. The colloids particles can migrate to surfaces, such as heat structures (e.g., piping walls) or pebbles in the reactor core. There is modeling flexibility for deposited particles to release back into the fluid. However, there is little experimental evidence for this release mode. Particles may also migrate to a pool surface layer that is at the interface between the salt pool and the gas space.

The final step is the release of aerosols or vapors into the gas space. Noncondensible gases such as Xe and Kr bubbles are released to the gas space when the bubbles reach the pool surface. Soluble and insoluble species with a significant vapor pressure can be released directly from the pool surface. The released vapors may condense or nucleate to form aerosol particles, which can settle back into the pool. Aerosol particles may also be released by bubbles that rupture. The bubble liquid film may include also soluble fission products, which could release into the gas space when the bubbles rupture.

The new pool fission product chemistry and release model is fully integrated into MELCOR. Any releases from the pool to the vapor space are modeled with the gas-phase radionuclide aerosol and vapor models. This is the first application in which the thermodynamic state was calculated using Thermochimica in each control volume. While the model structure is nearly complete, the MELCOR code development and applications staff are currently working on adding flexibility to incorporate alternative thermochemical databases and built-in physics options for the form-wise transfer functions.

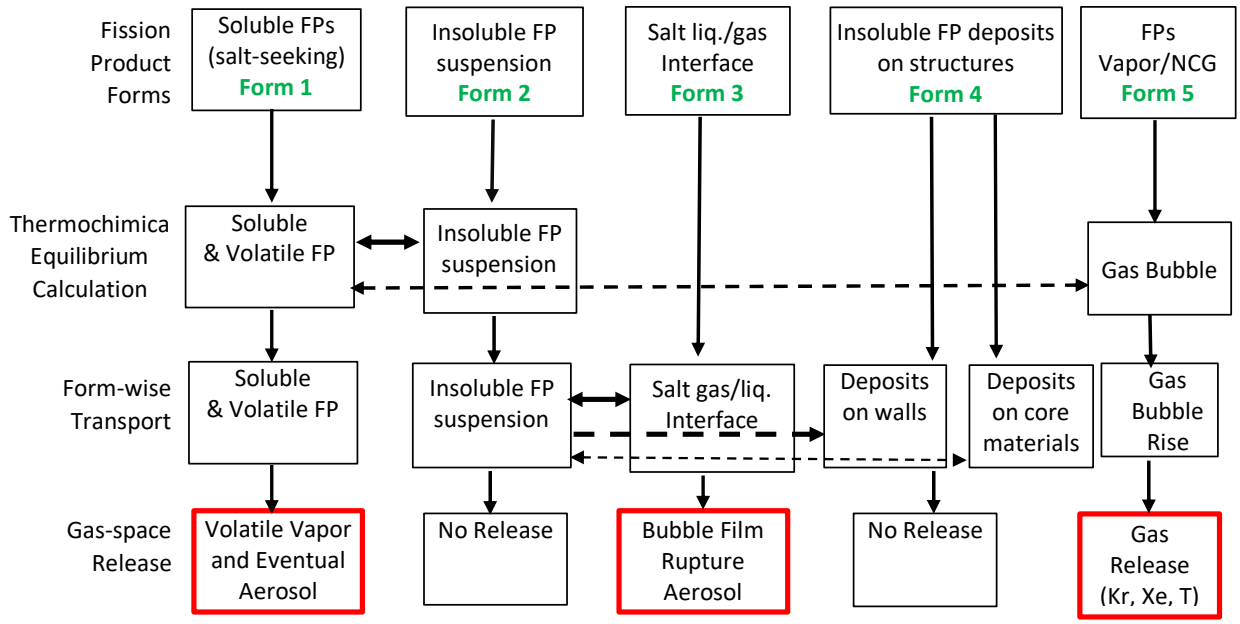

Figure 3-15 MELCOR pool fission product chemistry and release model.[2]

3.6. Point Kinetics Modeling

MELCOR includes a six-group point kinetics model for the dynamic calculation of the reactor power. The model was developed to support the evaluation of the DOE NGNP [20]. ORNL determined the reactivity feedbacks for the Mk1 using SCALE. Following the initial research of UCB [8], separate temperature feedbacks were determined for the fuel, the molten salt around the fuel, the pebble matrix, the central reflector, and the outer reflector (see Figure 3-16). The reactivity data were incorporated into the reactor control system for ATWS scenarios.

The ATWS scenarios were extended to a return to power after a xenon poisoning transient. ORNL did an analysis of the xenon reactivity following shutdown. The xenon worth curve was also placed into the Mk1 model to capture this important effect during an ATWS. The xenon reactivity curve is shown in Figure 3-17.

[2] The horizontal arrows correspond to mass transfer processes between forms. Only the forms pointed to by an arrowhead indicate mass transfer. Masses of released species are given in the bottom row in red-bounded boxes.

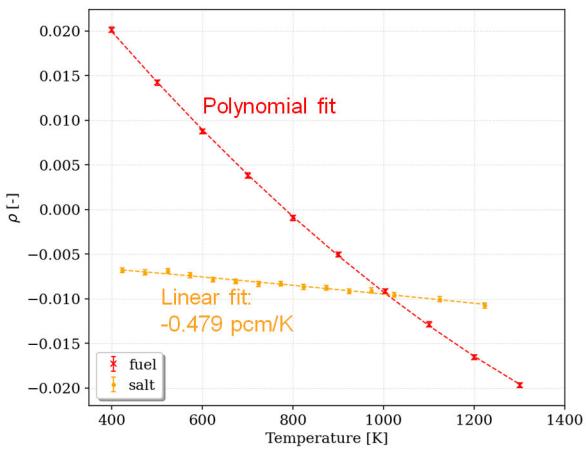

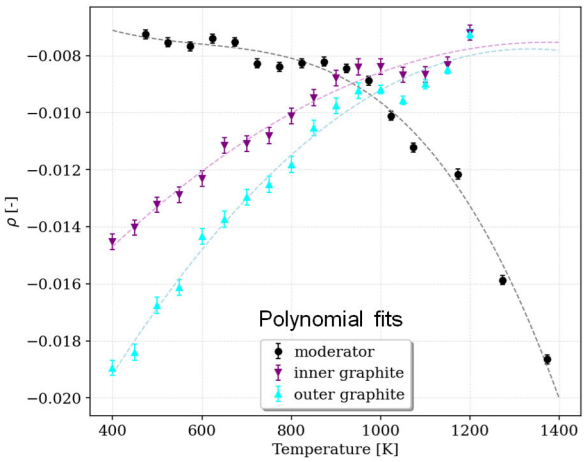

1. Linear fit for salt temperature coefficient
2. Polynomial fit or tabulated values for fuel, moderator, and graphite temperature coefficients

2σ statistical error bars are displayed

$$\rho = a + bT + cT^2 + dT^3$$

	a	b	c	d
Fuel	4.57E-02	-7.08E-05	1.59E-08	
Moderator	-2.02E-03	-2.48E-05	3.88E-08	-2.16E-11
Inner graphite	-2.18E-02	2.07E-05	-7.55E-09	
Outer graphite	-3.10E-02	3.49E-05	-1.31E-08	

Figure 3-16 Mk1 reactivity feedback curves [5].

- Steady-state Xe-135 reactivity worth is -6.48$
- Using equilibrium I-135 and Xe-135 concentrations from UCB Mark 1 model, we can calculate time-dependent concentrations analytically
- When flux goes to zero, Xe-135 inventory is dictated only by decay of I-135 and Xe-135
- Peak Xe-135 reactivity is -18.6$ and occurs at 9.49 hours
- Xe-135 reactivity drops below steady-state value after 34.67 hours

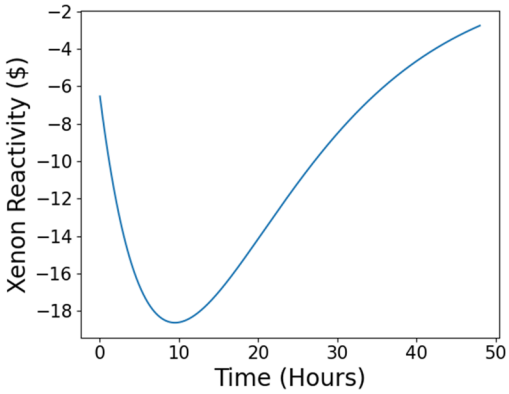

$$\frac{dI}{dt} = \gamma_I \Sigma_f \phi - \lambda_I I$$

$$\frac{dX}{dt} = \gamma_X \Sigma_f \phi + \lambda_I I - \lambda_X X - \sigma_a X \phi$$

Figure 3-17 Mk1 xenon response [5].

3.7. Steady State Initialization

The Mk1 model was stabilized to steady state conditions that were provided in Reference [4]. Figure 3-18 through Figure 3-25 show the comparison to key steady state variables from Reference [4]. The calculated agreement with the reference data was good. Long-term steady state calculations were performed to establish the initial conditions. The results from the long-term steady state calculations were successively reentered into the input files over time, which permitted a shorter initialization period prior to the transient calculations.

Prior to -100 sec, the point kinetics model was in steady power mode and not calculating any reactivity feedbacks. Consequently, the fission power is constant while the model stabilizes to steady conditions. The reactivity feedback is specified to begin at -100 sec, which allows confirmation of steady power conditions prior to the transient.

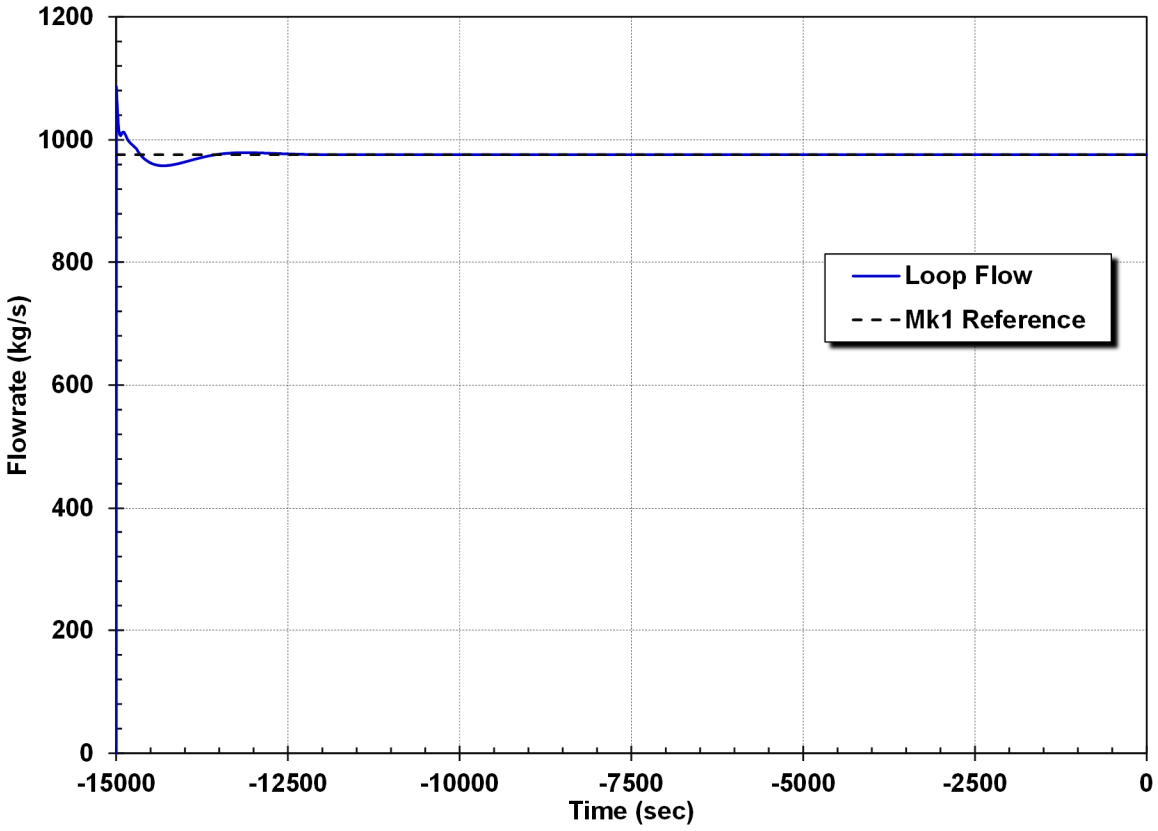

Figure 3-18 Steady state core flow.

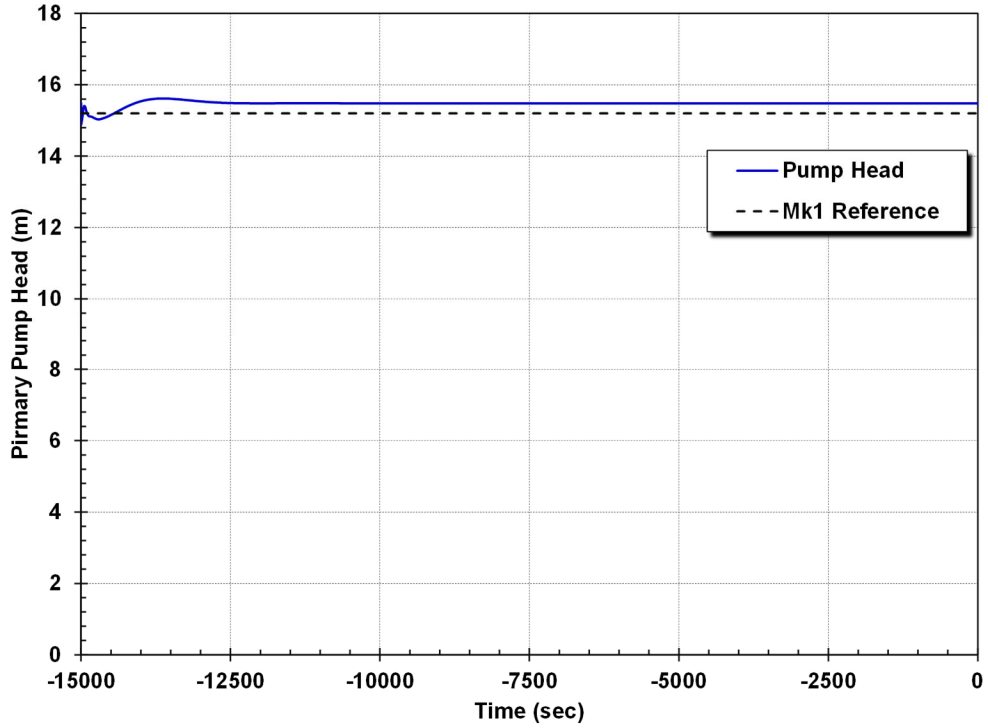

Figure 3-19 Steady state salt pump head.

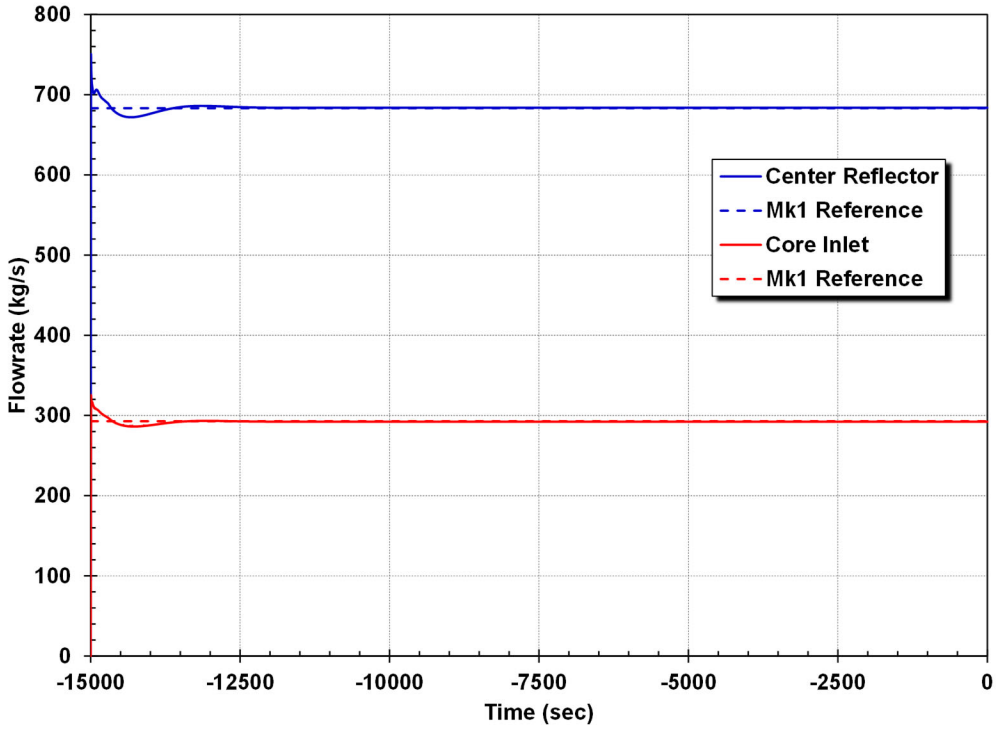

Figure 3-20 Steady state center reflector and core inlet flow distribution.

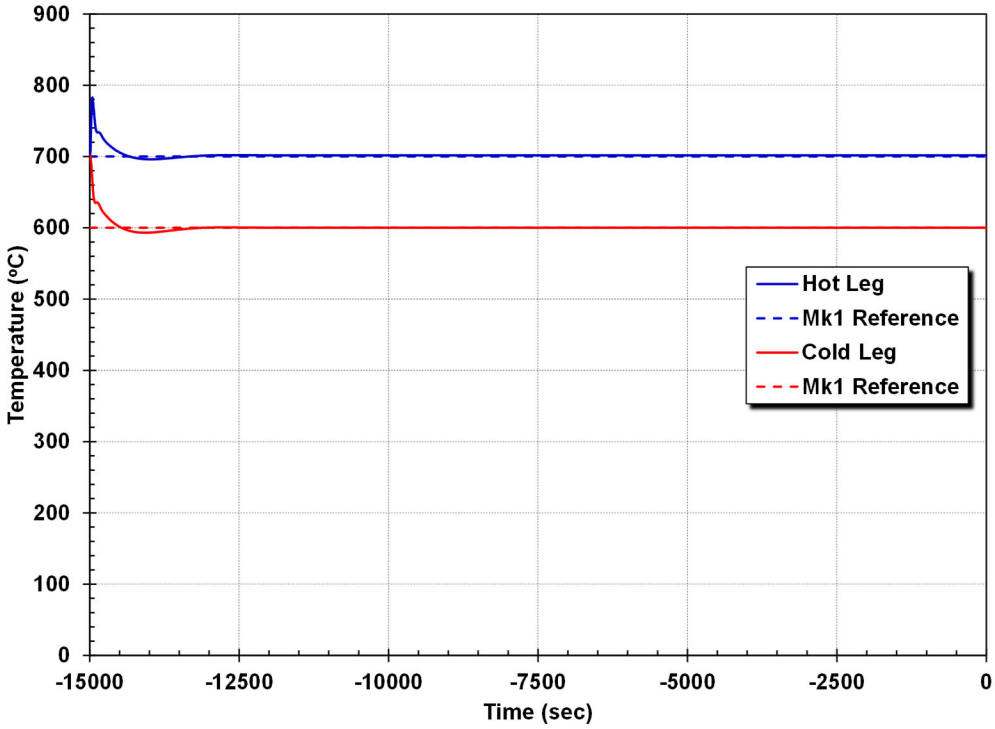

Figure 3-21 Steady state hot leg and cold leg temperatures.

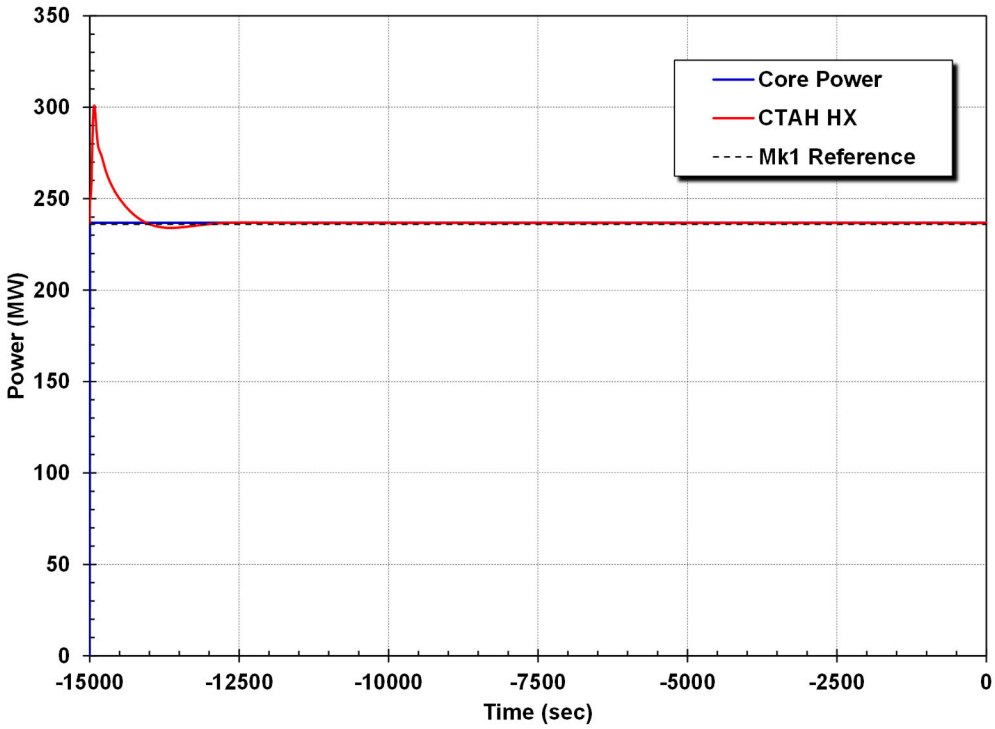

Figure 3-22 Steady state core and CTAH energy balance.

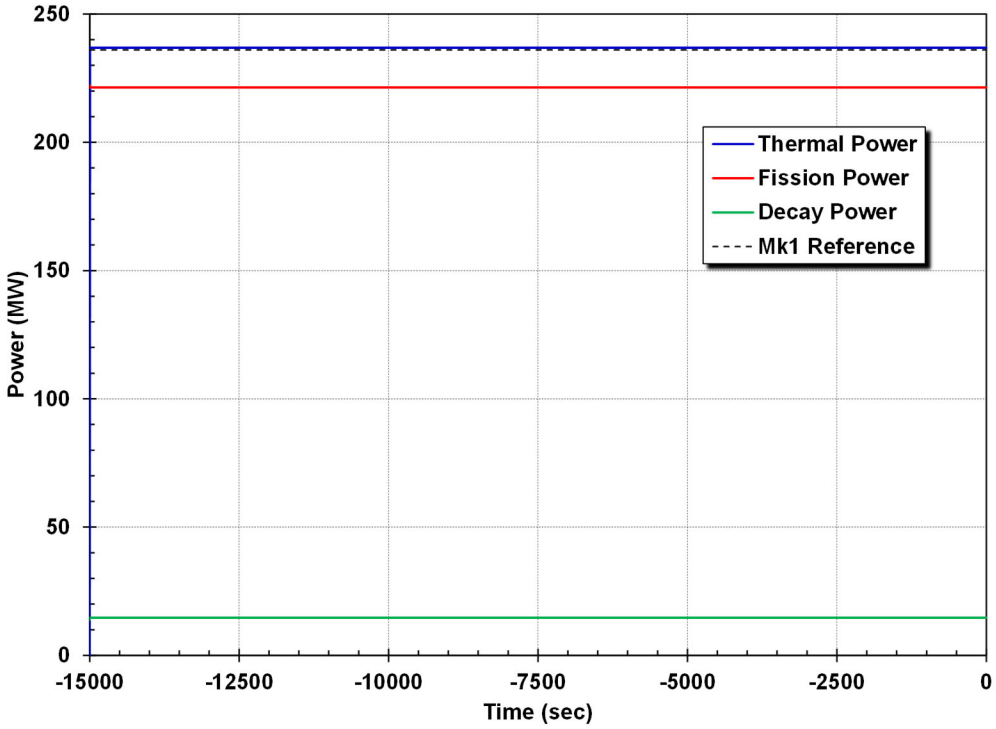

Figure 3-23 Steady state core thermal, fission, and decay power.

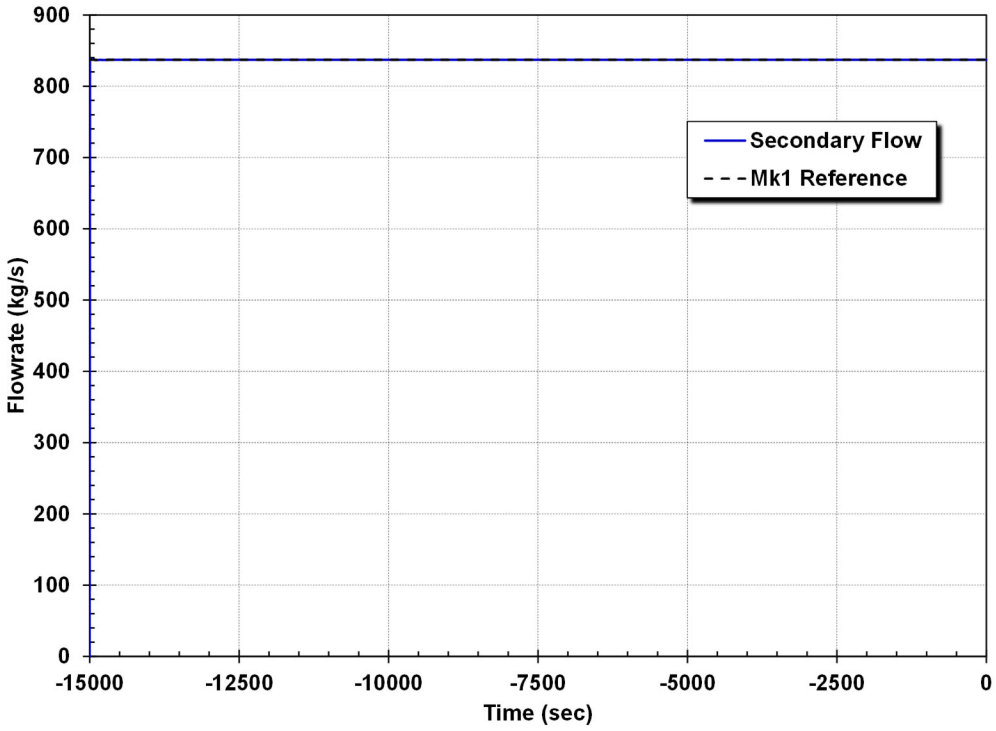

Figure 3-24 Steady state secondary CTAH air flowrate.

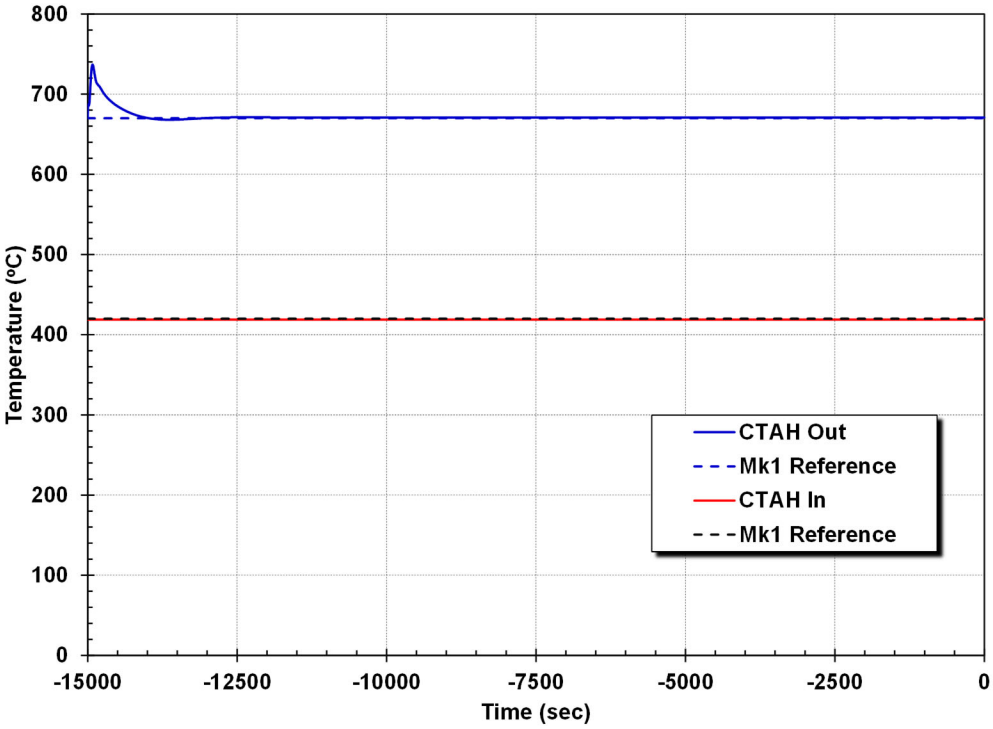

Figure 3-25 Steady state secondary-side CTAH inlet and outlet temperatures.

4. EXAMPLE RESULTS

The Mk1 demonstration calculations consisted of ATWS,[3] station blackout, and LOCA scenarios. As described in Section 3.5.2, one LOCA calculation was performed using the new pool fission product chemistry and release model. Each of the three scenario groups included some boundary condition variations to illustrate the Mk1 response to varying amounts of heat removal. The ATWS scenarios are discussed in Section 4.1; the SBO scenarios are discussed in Section 4.2; the LOCA scenarios are discussed in Section 4.3; and the LOCA with the pool fission product chemistry and release model is discussed in Section 4.4. The discussion of the calculations includes the thermal-hydraulic response of the Mk1 reactor. The SBO and LOCA discussions also present the associated radionuclide release behavior.

MELCOR Revision 19798 was used for all of the demonstration calculations except the one. The LOCA with the new pool fission product chemistry and release model used MELCOR Revision 20976, which included some updates to the pool chemistry and release model.

4.1. Anticipated transient without SCRAM

The ATWS is initiated with a loss of all onsite power. The salt pumps shut off and coast to a stop, and the secondary heat removal ends. However, the reactor protection system fails to insert the control rods into the core. Subsequently, the point kinetics model calculates the power transient using the reactivity feedbacks provided by ORNL (see Section 3.6). Four ATWS calculations are presented that illustrate the system response with normal and degraded DRACS availability.

The base ATWS case assumes all three DRACS units are available. Figure 4-1 shows the core temperature response to the loss of flow and secondary heat removal. The five temperatures in Figure 4-1 are the average temperatures used in the feedbacks for the point kinetics model. The fuel, moderator, and molten salt temperatures[4] rise after the pumps coast down (~10 seconds) and reach a maximum between 90 to 100 seconds. The average fuel, moderator, and molten salt temperatures subsequently begin a sustained cooldown until nearly 100,000 sec, which is followed by a rapid temperature increase.

The response of the large inner and outer reflectors is much slower. The average inner and outer reflector temperatures rise more slowly and lag behind the fuel and fluid temperatures. The outer reflector absorbs energy and increases in temperature through 630 sec before slowly cooling. Similarly, the inner reflector temperature increases through 1130 sec before starting a slow cooldown. Although the magnitude of the heatup of the reflectors is smaller than the fuel and the molten salt, the large heat capacity of the graphite structures is important for absorbing heat from the core and mitigating the overall fuel heatup.

The DRACS system automatically starts at approximately 10 seconds after the main salt pumps coast down (Figure 4-2). The core fission power decreases to less than 2.4 MW by 215 sec (i.e., 1% of the full power level). Meanwhile, the DRACS heat removal steadily increases to 7.5 MW and

---

[3] ATWS and SCRAM are generic terms often associated with BWRs and also used here. The FHR designers may use other scenario names for ATWS such as a reactivity transient. Similarly, the reactor protection system may be used in lieu of SCRAM.

[4] The fuel temperature is the average fuel kernel temperature. The moderator temperature is represented with the average fueled pebble matrix temperature. The molten salt temperature is represented by the average fluid temperature around the fueled pebbles.

exceeds the core power by 330 sec. Consequently, the heat absorption by the large reflectors, the DRACS heat removal, and natural convective flow from the core combine to start the cooldown of the fuel and molten salt observed in Figure 4-1.

The relatively small heatup of the fuel in the ATWS is attributed the large heat capacity of the materials in the core and the strong negative reactivity feedbacks that quickly reduce the fission power. Figure 4-3 shows the relative magnitudes of the reactivity feedbacks that contributed to the fast reduction in power. The fuel, moderator, and molten salt feedbacks combined to provide the initial negative feedback that decreased the fission power from 100% to 1% in 215 seconds. The reflector feedbacks are weakly positive during this timeframe due to their smaller contribution to the overall reactivity (i.e., see Figure 3-16) and the small increase in reflector temperatures (i.e., see Figure 4-1). After the reflectors start to cooldown, their feedback becomes negative.

The long-term reactivity feedback is dominated by the xenon feedback. The long-term negative xenon feedback, which is dominated by the growth and decay of Xe-135, adds significant negative feedback after 200 sec and reaches a maximum at approximately 33,000 sec (9.1 hr). While the system cooldown by the DRACS led to positive fuel, moderator, and molten salt reactivity additions, the strong negative xenon feedback overwhelms these effects. After the negative xenon reactivity decays away, the net core reactivity becomes positive near 100,000 sec.

Figure 4-4 through Figure 4-6 show the reactor response after the total reactivity becomes positive. Prior to the positive reactivity addition, the fission power is approximately 0 MW and the decay power is 1.1 MW. In response to the positive reactivity addition, the fission power increases to approximately 22 MW. The power increase causes the average fuel temperature to increase 50°C, which causes an overall negative feedback and stops the power increase. While the fuel slowly cools immediately after the power increase, the overall reactivity remains negative. The core fission power subsequently decreases to 1.6 MW in response to the negative reactivity. Approximately 540 sec later at 90,360 sec, the cooler fuel contributes to another positive reactivity addition. However, the second power increase is only to 6.3 MW. One more small power oscillation occurs before the core power starts a slow increase to 8.6 MW at 105,000 sec.

The energy balance in Figure 4-4 shows an imbalance in the core power and the DRACS heat removal following the increase in fission power. The core heatup also causes an increase in the DRACS heat removal rate. The integrated system response requires a slow but sustained heatup of the fuel for its negative reactivity effect to offset an increasing DRACS heat removal rate and the residual but decreasing negative xenon feedback. By the end of the calculation at 135,000 sec, the core power and the DRACS heat removal rate are converging (see Figure 4-4) and the fuel, the moderator, and the molten salt temperatures were stabilizing (see Figure 4-5). The reflectors are slowly heating but lagging behind the fuel, the moderator, and the molten salt temperatures.

The core response is relatively stable after the three power oscillations as the system slowly transitions to a new equilibrium core power and DRACS heat removal rate. The net reactivity subsequently oscillates near zero while the excess xenon decays away and the system slowly heats. A very small power oscillation occurs at 11,790 sec as the inner reflector starts adding a small positive reactivity from its gradual heatup (see Figure 4-6). Overall, the system responds in a dampening and self-correcting manner. The new equilibrium occurs where the core power balances the DRACS heat removal and the overall reactivity is approximately zero. No other power oscillations are expected after 135,000 sec.

The highest average fuel temperature and the highest peak fuel temperature were 789°C at 90 sec and 853°C at 17 sec, respectively. Although the ATWS scenario included a loss of forced circulation

and secondary heat removal without an insertion of the control rods, the large heat capacity of the pebbles, the reflectors, and the molten salt in the core and the strong negative reactivity to the temperature rise mitigated the fuel heatup. Any radionuclide releases from the fuel to the molten salt coolant were on the order of the very small operational releases. Consequently, the ATWS was considered mitigated by the DRACS.

Three ATWS sensitivity calculations were performed to investigate degraded DRACS configurations. The FHR has three DRACS units available but these sensitivity cases investigated failures of one, two, and all three DRACS units. The three sensitivity cases are presented with the previous base case result for comparison. Although the base case with all three DRACS units might appear to offer the best mitigation for an ATWS, the three DRACS units cause a stronger cooldown during the xenon reactivity transient that could lead to an earlier and stronger positive reactivity addition from the fuel, moderator, and molten salt. Consequently, there could be offsetting factors that impact the early and long-term responses.

Figure 4-7 shows the peak fuel temperature response for the four cases. As discussed above, the three DRACS case has the lowest initial peak temperature and the fastest cooldown. The other two cases with operating DRACS units have successively higher initial peak temperatures and slower cooldowns. However, the differences in the peak fuel temperatures are relatively insignificant due to the low impact of the DRACS heat removal relative to the heat capacity of the system in the first 200 sec. The case with no DRACS illustrates the significant role of the core heat capacity to slow the system heatup for several hours without any heat removal.

Figure 4-8 shows a comparison of the core power versus the DRACS heat removal for the four cases. The initial rise in the core temperature that caused the large negative feedback was relatively unaffected by the availability of the DRACS. In all four cases, the decrease in the core power is approximately the same with each additional operating DRACS unit causing an almost imperceptible slowdown in the power decrease. The negative xenon feedback becomes observable after approximately 200 sec, which grows to overwhelm the other feedbacks. In summary, the early core power response was similar for all four cases due to a similar negative reactivity insertion from the initial fuel temperature rise, which is subsequently supplemented with the negative xenon feedback.

The comparison of the DRACS heat removal with the core power illustrates the overall system energy balance (see Figure 4-8). The three, two, and one DRACS heat removal rates exceeds the core power at 330 sec, 1090 sec, 9780 sec, respectively. The impact on the successively latter times for the DRACS heat removal to exceed the core decay power is evident on Figure 4-7. The single DRACS unit case shows a flattening of the peak temperature curve between 2000 sec to 10,000 sec because of the lower heat removal from one DRAC unit (see Figure 4-7). Similarly, the two DRACS case shows a slower temperature cooldown rate than the three DRACS case but not a significant plateau like the one DRACS unit case.

The late responses of the ATWS cases with variable DRACS units are shown in Figure 4-9 and Figure 4-10. The temperature rises after the positive reactivity insertion occur successively. All DRACS cases show an approximately 75°C increase in the peak fuel temperature and a 22 MW fission power transient in response to the positive reactivity insertion. The two and one DRACS cases are successively delayed relative to the base case with three DRACS but not significantly due to a similar xenon transient. Due to the greater cooldown with more operating DRACS in the base case, the accompanying positivity reactivity from the fuel, moderator, and molten salt results in a slightly earlier rise in the fission power.

The long-term responses of the core power and the DRACS heat removals are similar for the three cases (i.e., see Figure 4-10). All three results show a rapid dampening of the core power oscillations. All cases have a heatup phase (i.e., the core power greater than the DRACS heat removal) after the rise in fission power but are converging towards a balance of the core power and DRACS heat removal by the end of the calculation. The difference in the core power and DRACS heat removal rates during the equilibration phase after the power increase is greater with more operating DRACS units to compensate for the higher overall DRACS heat removal rate. However, all three cases are converging nearly converged by 135,000 sec.

The ATWS case without DRACS was not extended beyond 100,000 sec (27.7 hr). The peak fuel temperature was 996°C at 100,000 sec and increasing due to the lack of the DRACS heat removal. However, there is still a large temperature and time margin until the molten salt begins boiling (i.e., the FLiBe boils at ~1310°C). If the ATWS continues unmitigated, then the fuel pebbles will continue heating. The LOCA that is described in Section 4.3 provides an example of a mechanistic source term from an unmitigated LOCA. The unmitigated LOCA includes a boiloff of the molten salt in the reactor vessel and a large fission product release.

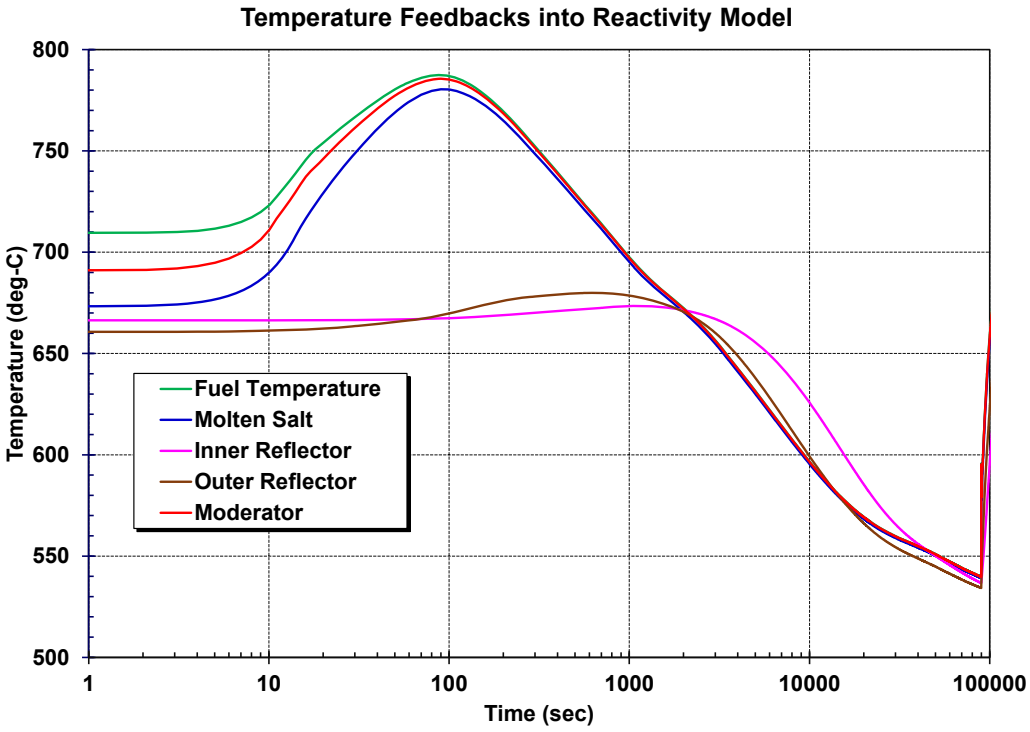

Figure 4-1 Core temperatures for the reactivity feedback model (semi-log scale).

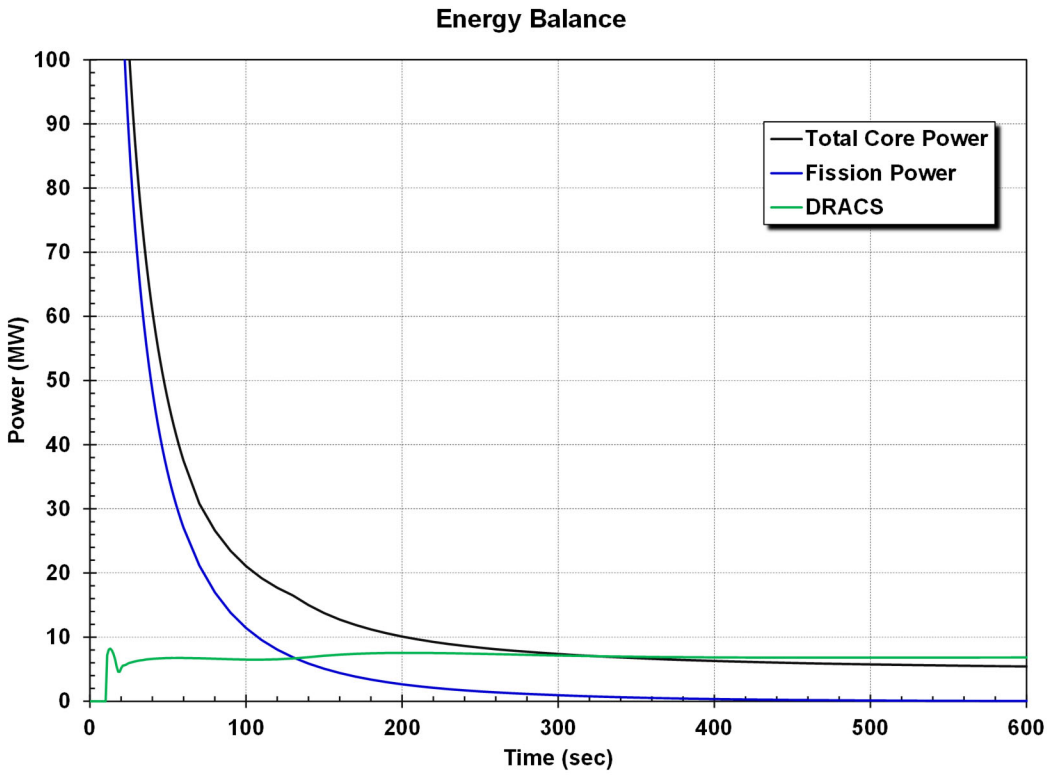

Figure 4-2 Core power, fission power, and the DRACS heat removal energy balance.

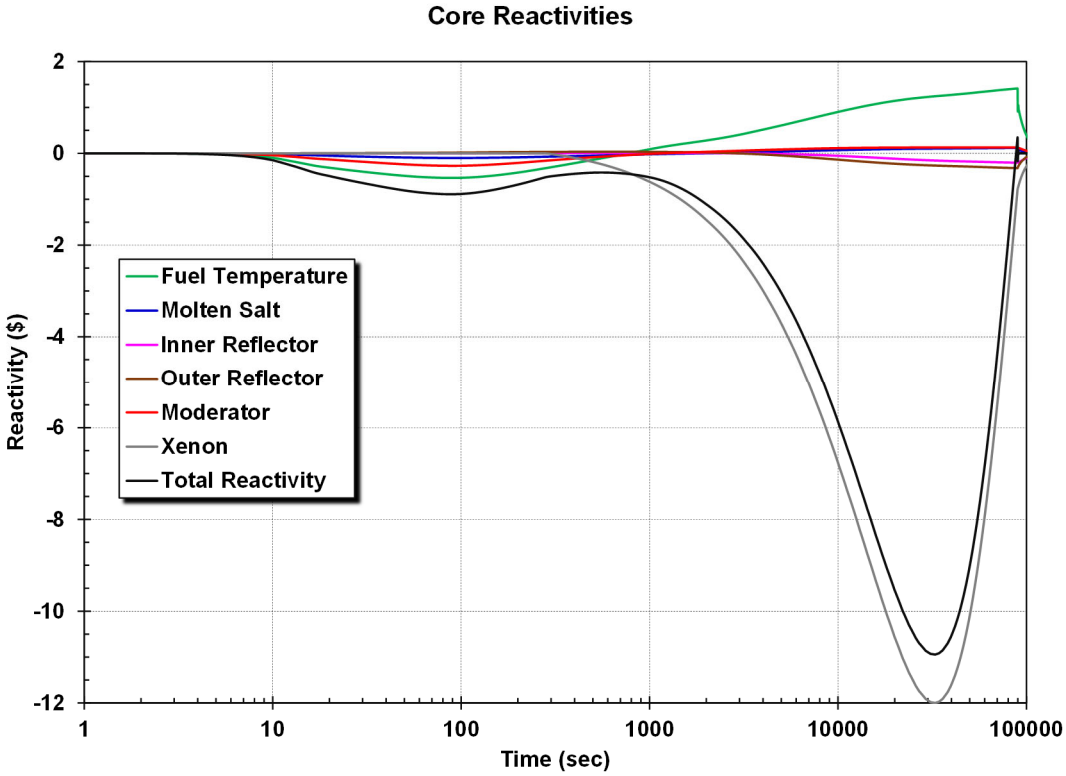

Figure 4-3 Core reactivity feedback (semi-log scale).

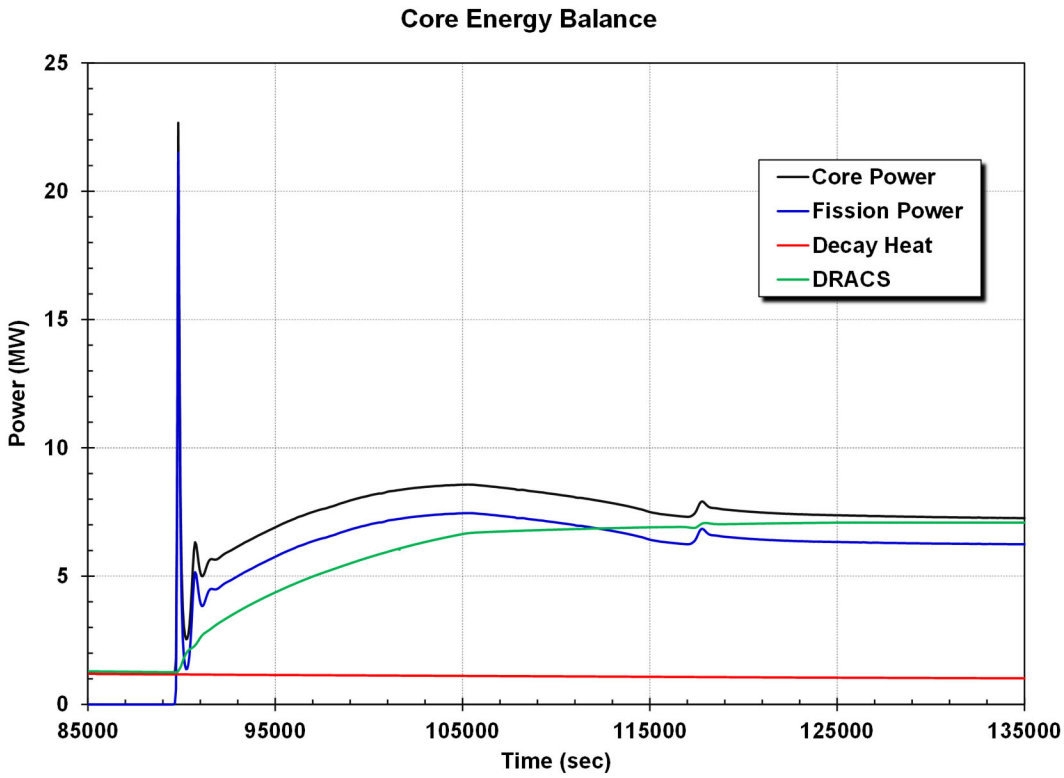

Figure 4-4 Core power, decay power, and the DRACS heat removal energy balance (linear scale).

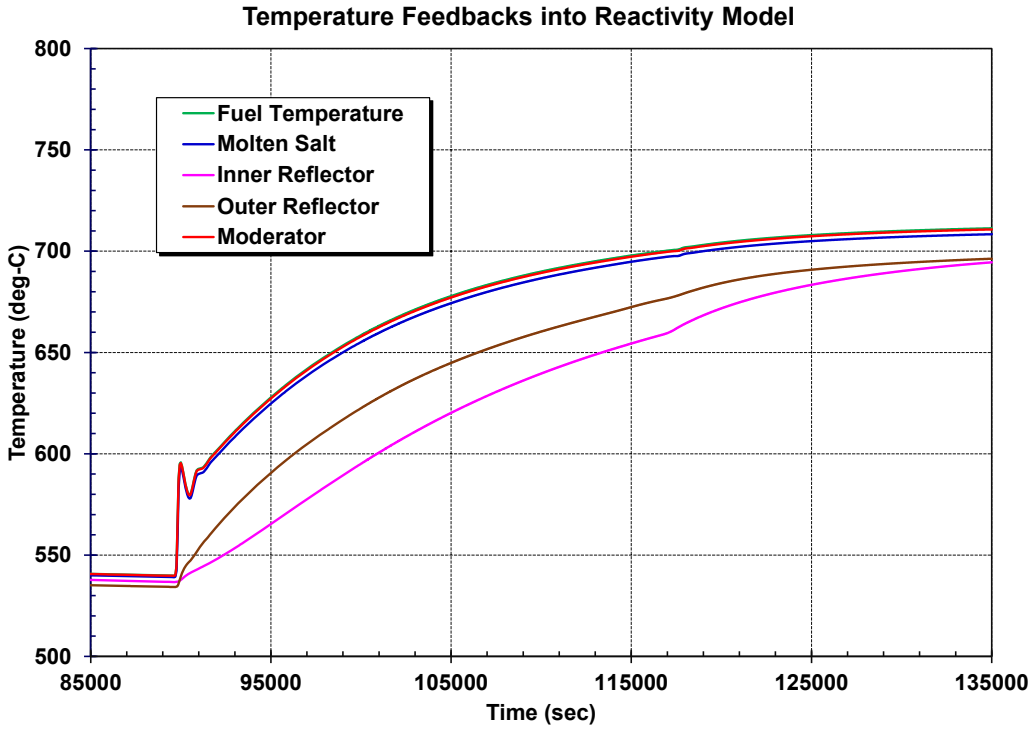

Figure 4-5 Core temperatures for the reactivity feedback model (linear scale).

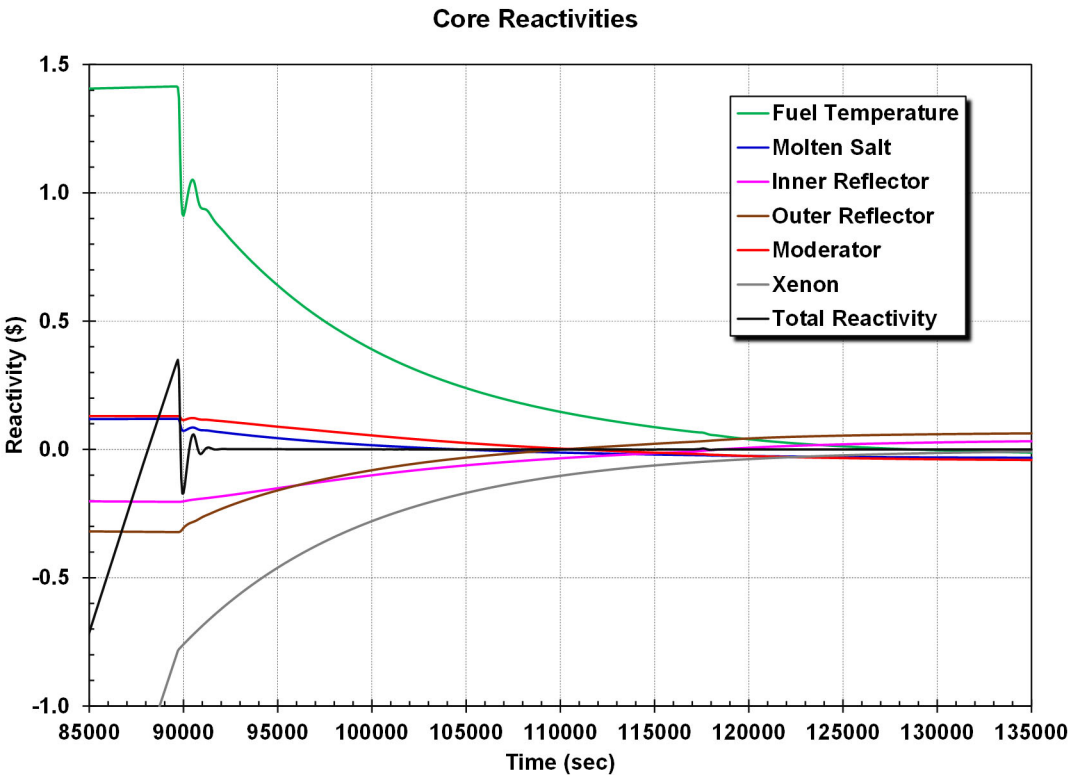

Figure 4-6 Core reactivity feedback (linear scale).

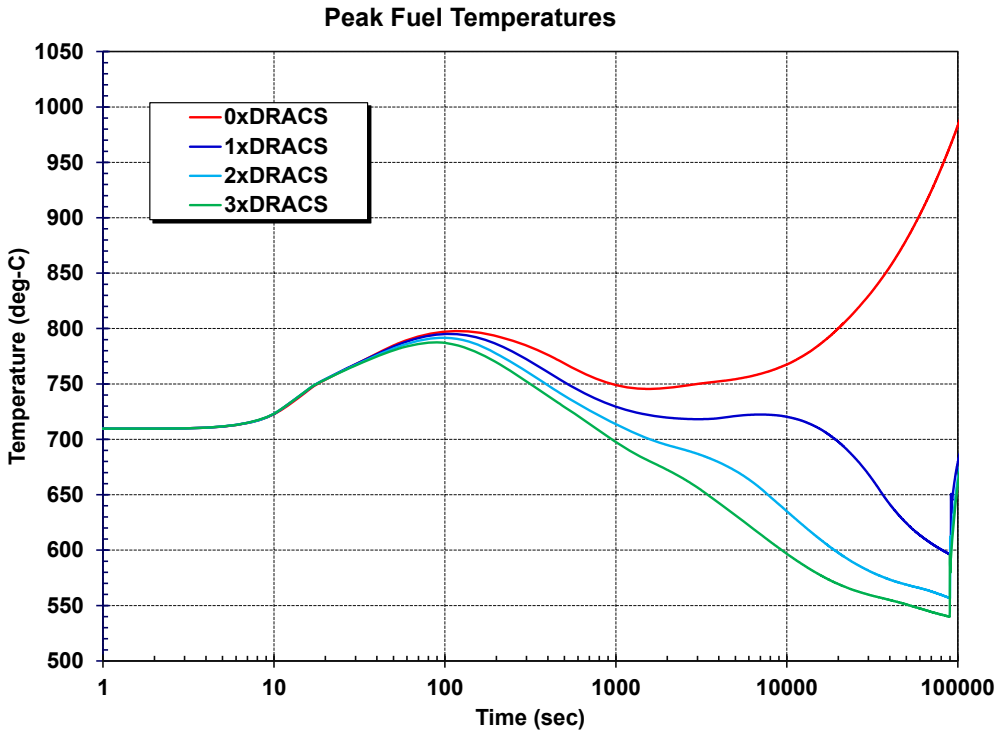

Figure 4-7 Peak fuel temperature response for the DRACS sensitivity cases (semi-log scale).

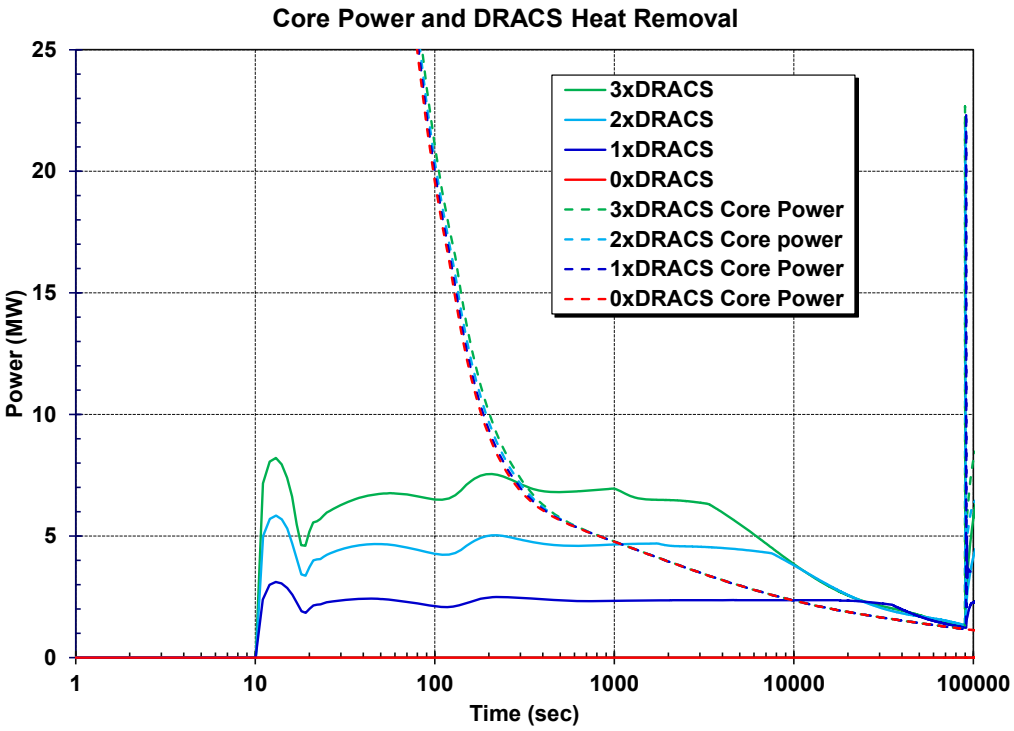

Figure 4-8 Comparison of the core power and DRACS heat removal rate for the DRACS sensitivity cases (semi-log scale).

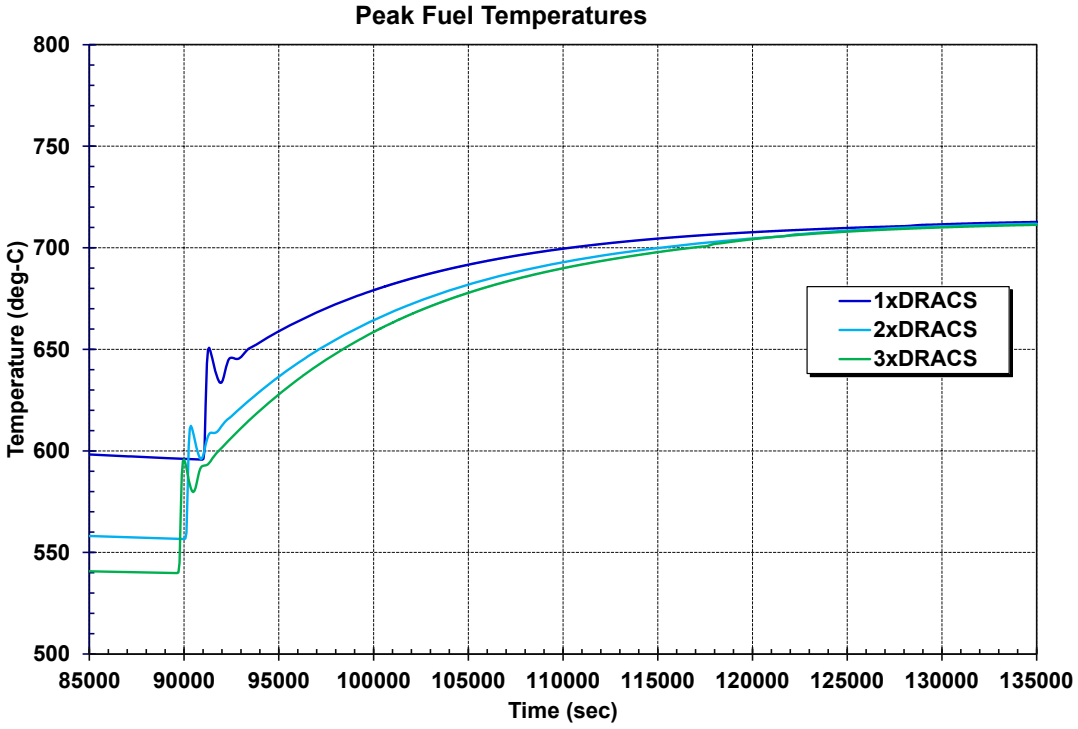

Figure 4-9 Peak fuel temperature response for the DRACS sensitivity cases (linear scale).

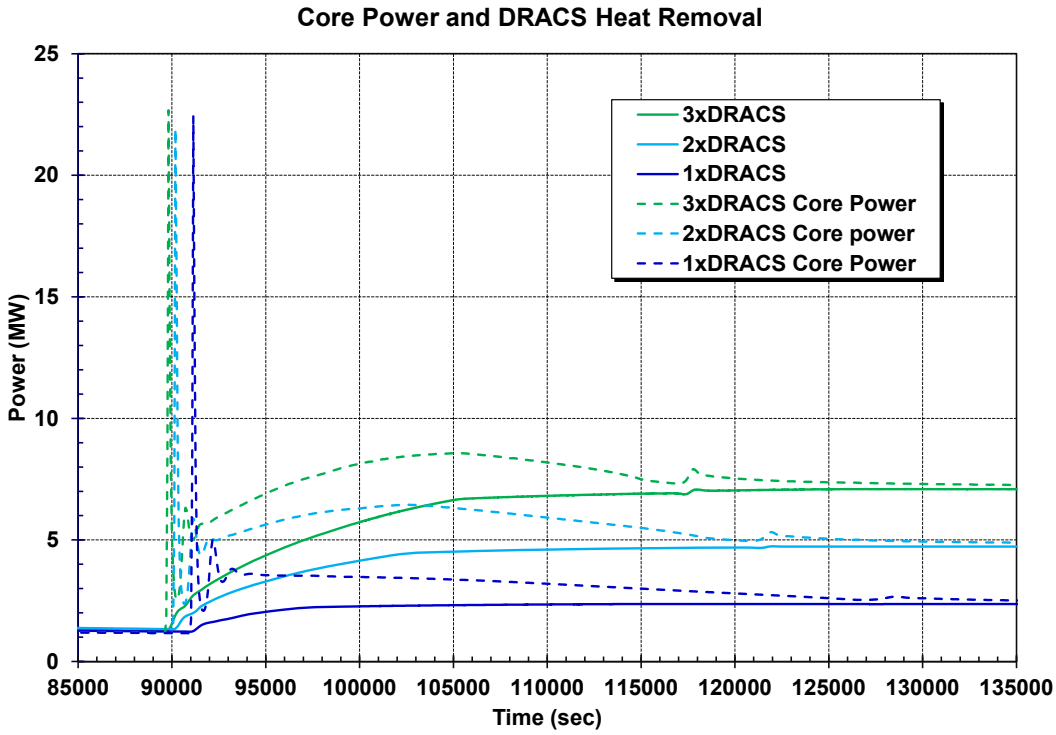

Figure 4-10 Comparison of the core power and DRACS heat removal rate for the DRACS sensitivity cases (linear scale).

4.2. Station blackout

The station blackout transient is initiated with a loss of all onsite power. The salt pumps shut off and coast to a stop, and the secondary heat removal ends. Unlike the ATWS, the reactor protection system inserts the control rods into the core. Due to the successful insertion of the control rods to terminate the fission power, the heat removal requirements are less than the ATWS, which was mitigated with one operating DRACS unit. It was decided to explore the minimum requirement for fuel cooling during a station blackout. Consequently, all the station blackout sequences assumed that only one DRACS unit is working. The sensitivity calculations further assume that the available DRACS unit was degraded from its rated performance (e.g., 80%, 60%, etc.). Each calculation was run for 48 hours.

Figure 4-11 shows the peak fuel response as a function of the DRACS rated performance. With a single DRACS unit operating without any degradation (i.e., 100%), the peak core temperature decreases from the steady state value of 762°C to 725°C over the first 30 sec as the salt pumps coast to a stop and the heat transfer to the secondary system ceases. The system slowly cools down to 620°C at 24 hr and 582°C at 48 hr. The fuel remained below its normal operating temperature for the entire transient. As the system cooled, the DRACS heat removal effectiveness decreased as the system gradually approach a balance between the core decay heat and the DRACS heat removal rate.

The remaining curves on Figure 4-11 show the impact of degrading the single DRACS unit, including a complete failure. The 0.8 x DRACS (i.e., 80%) result is relatively flat over the first 6 hr but then asymptotically approaches the 100% result. The 60% result rises to approximately 12°C above the normal operating temperature over the first 16 hr but subsequently decreases to 610°C at

48 hr. The 40% case has a similar trajectory as the 60% case but remains above the normal operating temperature through 48 hr. However, the maximum temperature for the 40% case is only 796°C and is cooling after 32 hr. Only the 20% and no DRACS cases are rising in temperature through 48 hr. The peak fuel temperature for the 20% and 0% cases at 48 hr are 929°C and 1089°C, respectively. The 20% DRACS heat removal offers a significant decrease in the heatup rate versus no DRACS case but not enough to exceed the decay power. Consequently, the maximum fuel temperature is rising at 48 hr. The no DRACS case will heat to saturation conditions after 48 hr (i.e., discussed later in this section) and start boiling away inventory. The FLiBe saturation temperature is indicated on the figure for reference.

A comparison of the decay heat and the DRACS heat removal for the SBO sensitivity calculations is shown in Figure 4-12. In addition to removing the core decay heat, the DRACS must also reduce the fuel pebble, the molten salt, and the reflector stored energy for the system temperature to decrease. With one DRACS working at 100% effectiveness, the DRACS heat removal converges toward the decay heat power over the first 24 hr, which corresponds to the flattening of the peak fuel temperature response in Figure 4-11.

The initial impact of the DRACS heat removal is evident in Figure 4-12 as successively lower values. As the DRACS heat removal is degraded, the times to exceed the core decay power are 2.7 hr, 5.3 hr 13.6 hr, and 45.7 hr for 100%, 80%, 60%, and 40% cases, respectively. The core decay power is greater than the 20% DRACS heat removal at 48 hr and not expected to be lower until ~180 hr. Consequently, only 40% effectiveness is needed to meet decay heat removal requirements within 48 hr, which is also evident on the peak fuel temperature response (Figure 4-11).

The TRISO failure fraction is shown in Figure 4-13 for the SBO sensitivity calculations. The TRISO failure fraction was initialized at 10^{-5}, which reflects an estimate of the manufacturing defects. As described in Section 3.5.1, the TRISO failure fraction is based on historical German Arbeitsgemeinschaft Versuchsreaktor(AVR) UO_2 TRISO experience. As described previously, the Mk1 uses UCO TRISO, which is expected to have an reduced failure rate due to a lower internal TRISO gas production [16]. However, a corresponding UCO TRISO failure model has not been developed due to the lack of high temperature testing of irradiated UCO TRISO. Coincidentally, the UO_2 failure curve (see Figure 3-14) increases above 10^{-5} when the fuel temperature increases above the maximum fuel temperature at normal operating conditions (~762°C). Consequently, the SBO cases with little to no heatup did not show any significant change in the overall TRISO failure fraction (i.e., the $\geq$40% DRACS cases). However, the TRISO failure fractions increase to 2.2×10^{-5} and 4.9×10^{-5} for the 20% effectiveness and no DRACS heat removal cases at 48 hr, respectively.

The cesium release from the pebbles though 48 hr is shown in Figure 4-14. As described in Section 3.5.1, the accelerated steady state was not used. Consequently, the early response of the cesium release reflects very small operational releases predicted at normal operating temperatures during the transient and does not include any prior operational releases. The cesium released from the pebbles is assumed to be retained in the molten salt. Section 4.4 includes a sensitivity study where the radionuclide pool chemistry and release model is used to estimate cesium releases from the molten salt into the gas space.

The SBO cases with $\geq$40% DRACS effectiveness show that the release fractional release of cesium from the pebbles is $<10^{-5}$ through 48 hr. As the fuel temperature rises to higher levels in the 20% and no DRACS cases, the cesium release fraction increases to 2×10^{-5} and 9×10^{-5} at 48 hr, respectively. The cesium releases are attributed to the TRISO with existing failures, the newly failed TRISOs that release cesium that was previously in the TRISO buffer (see Figure 2-1), and also

diffusion through the intact TRISO protective layers. However, the releases are very small and assumed to be retained within the primary system in the molten salt.

The SBO without DRACS was extended to 1-week. The peak fuel response and the vessel exit saturation temperature are shown in Figure 4-15. The fuel temperature continued to rise and reached the saturation temperature of the molten salt at ~120 hr. The molten salt in the vessel started to boil and evaporate while the fuel stayed near the saturation temperature of the salt. The peak fuel temperature remained near the saturation temperature through 168 hr (i.e., 1 week) when the calculation was terminated.

The heating of the molten salt causes its expansion, which causes the system to pressurize. It was assumed that the cover gas system connected the hotwell to a leak-tight enclosure in the lower containment. As described in Section 3.2.2, the enclosure compartment was assumed to have a rupture disk that opens at 68.9 kPa (10 psig). The primary system depressurization following the rupture disk opening at 19.2 hr can be seen in saturation temperature response in Figure 4-15.[5] Prior to the enclosure rupture disk opening, the primary system and the enclosure pressurized to 68.9 kPa (10 psig) relative to the containment pressure. Once the enclosure rupture disk opened, the cover-gas system vented into the containment through the open rupture disk.

Figure 4-16 shows the vessel downcomer and hotwell level responses in the SBO without DRACS. The initial expansion of the molten salt caused the level in the hotwell to increase. The molten salt overflowed into the cover-gas system and into the enclosure compartment in the containment. The hotwell remained full through 113 hr as molten salt overflowed into the cover-gas system. However, a vapor bubble formed in the hotwell after salt vapor started being produced in the core. As the boiling in the vessel continued, the vapor bubble grew and extended back into the vessel. The vessel level was approaching the top of the refueling chute at 168 hr, and the hotwell was completely filled with salt vapor. The calculation was terminated at 168 hr but illustrated the long time margin before any fuel uncovery.

[5] The drop in the saturation temperature at 19.2 hr is a direct response to the enclosure compartment rupture disk opening. The enclosure compartment abruptly decreased from 68.9 kPa (10 psig) over the containment pressure to the containment pressure when the molten salt vapor discharged from the enclosure compartment. Due to the primary system cover-gas connections to the hotwell, the entire primary system also dropped in pressure when the rupture disk opened. The decrease in the saturation temperature corresponds to the decrease in the system pressure, which is determined by the molten salt equation of state routine (see Section 2.2).

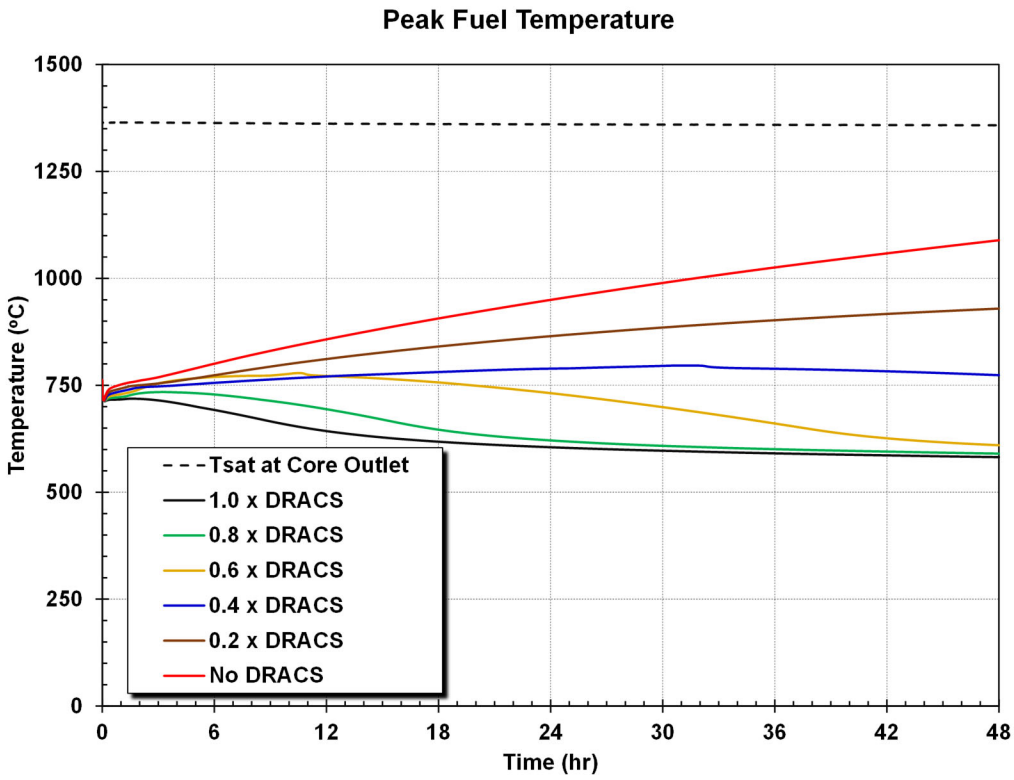

Figure 4-11 Comparison of the peak fuel temperatures for the SBO DRACS sensitivity cases.

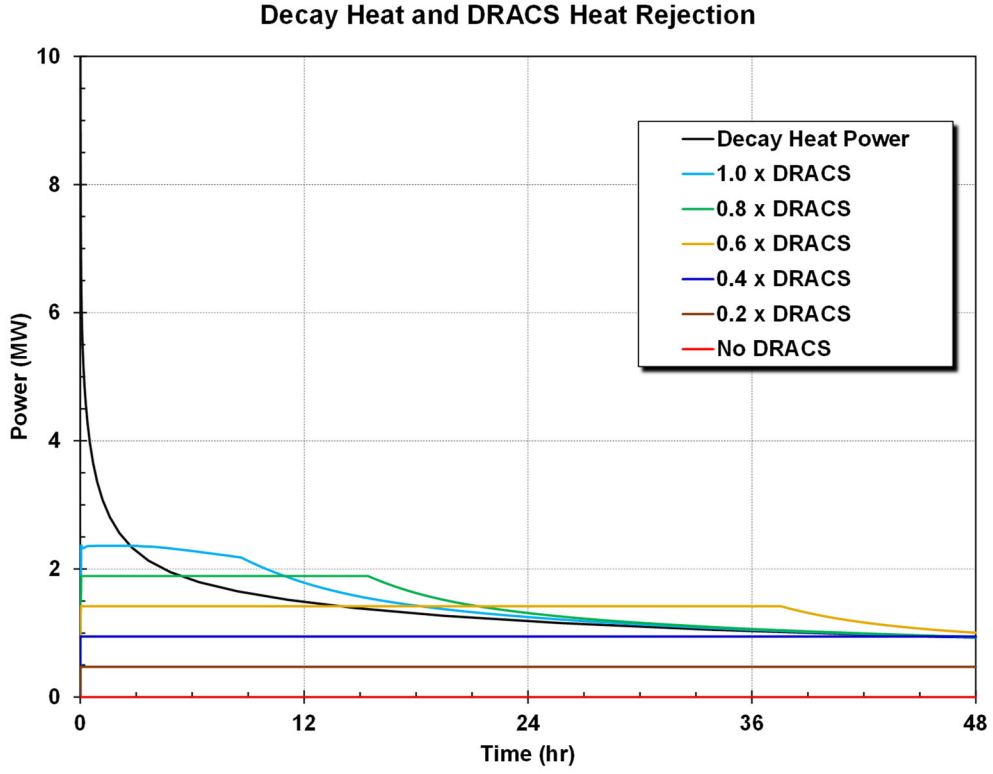

Figure 4-12 Comparison of the decay heat and DRACS heat removal for the SBO DRACS sensitivity cases.

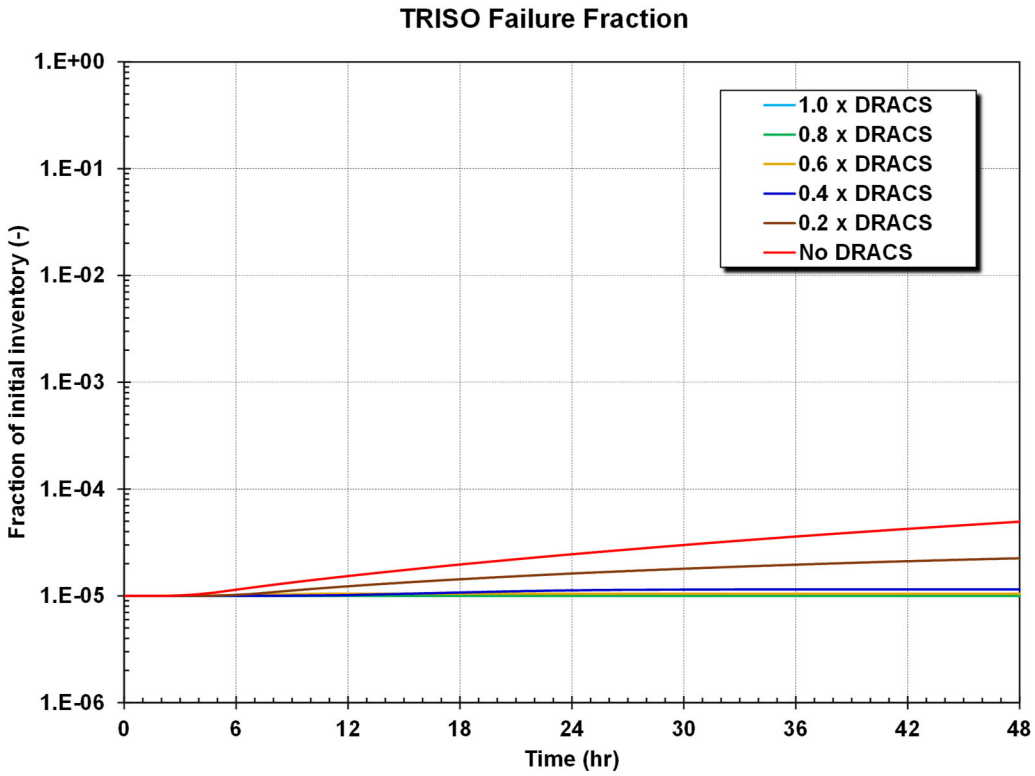

Figure 4-13 Comparison of the TRISO failure fraction for the SBO DRACS sensitivity cases.

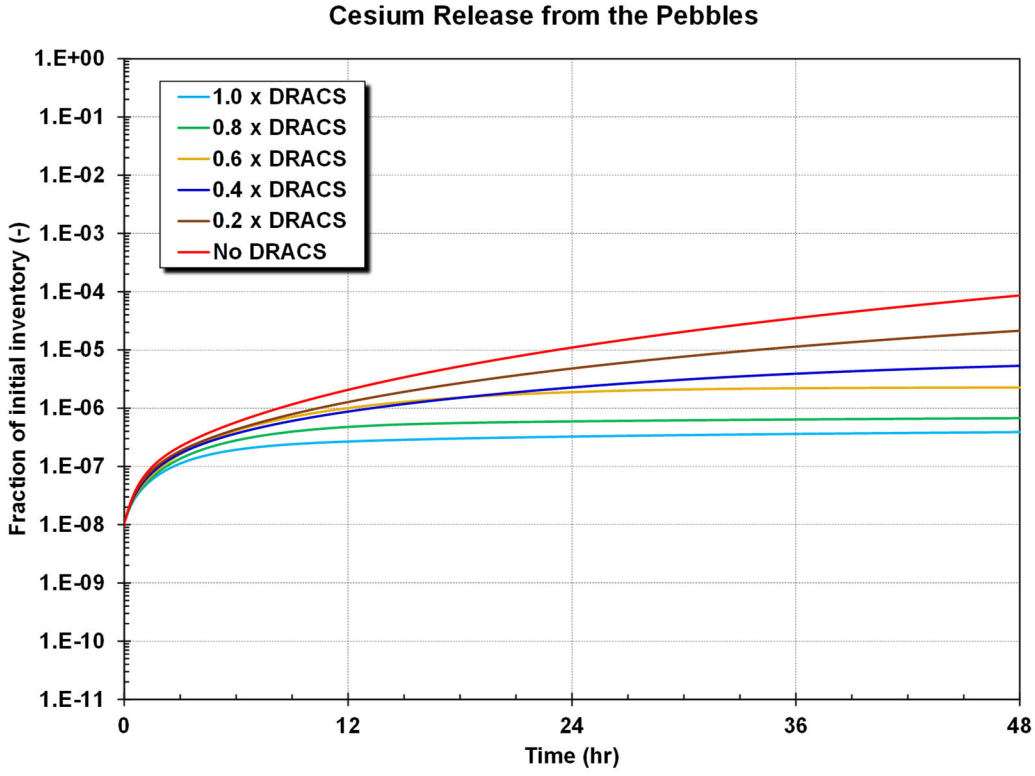

Figure 4-14 Comparison of the cesium release from the pebbles for the SBO DRACS sensitivity cases.

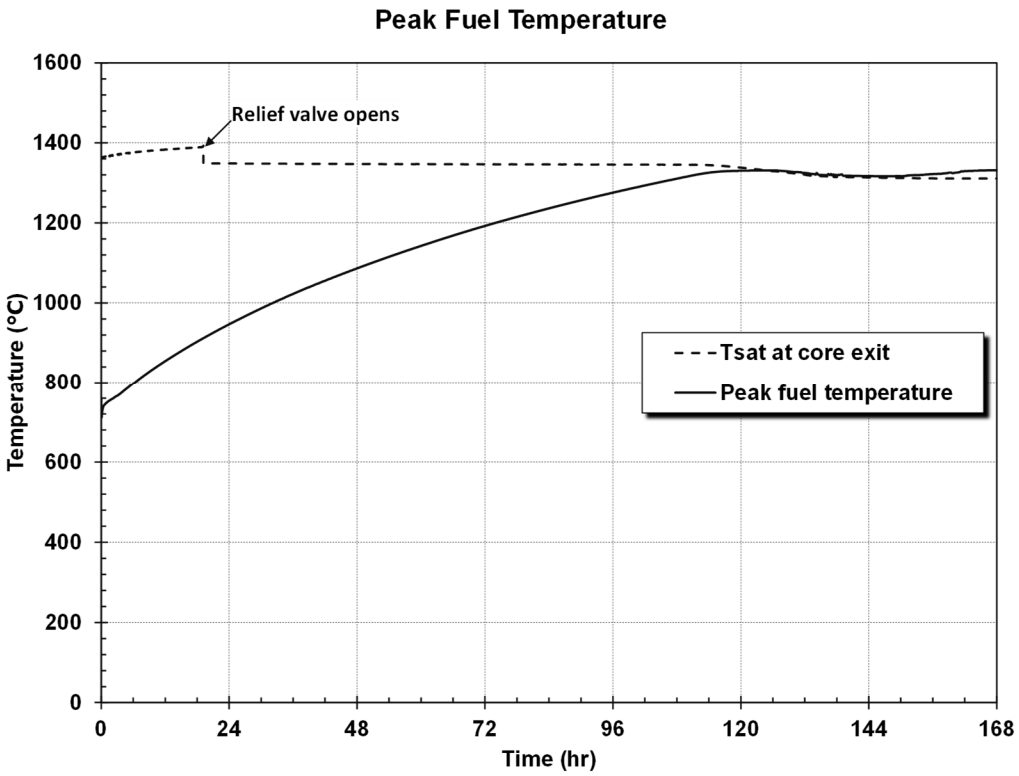

Figure 4-15 Peak fuel temperature for the SBO without DRACS.

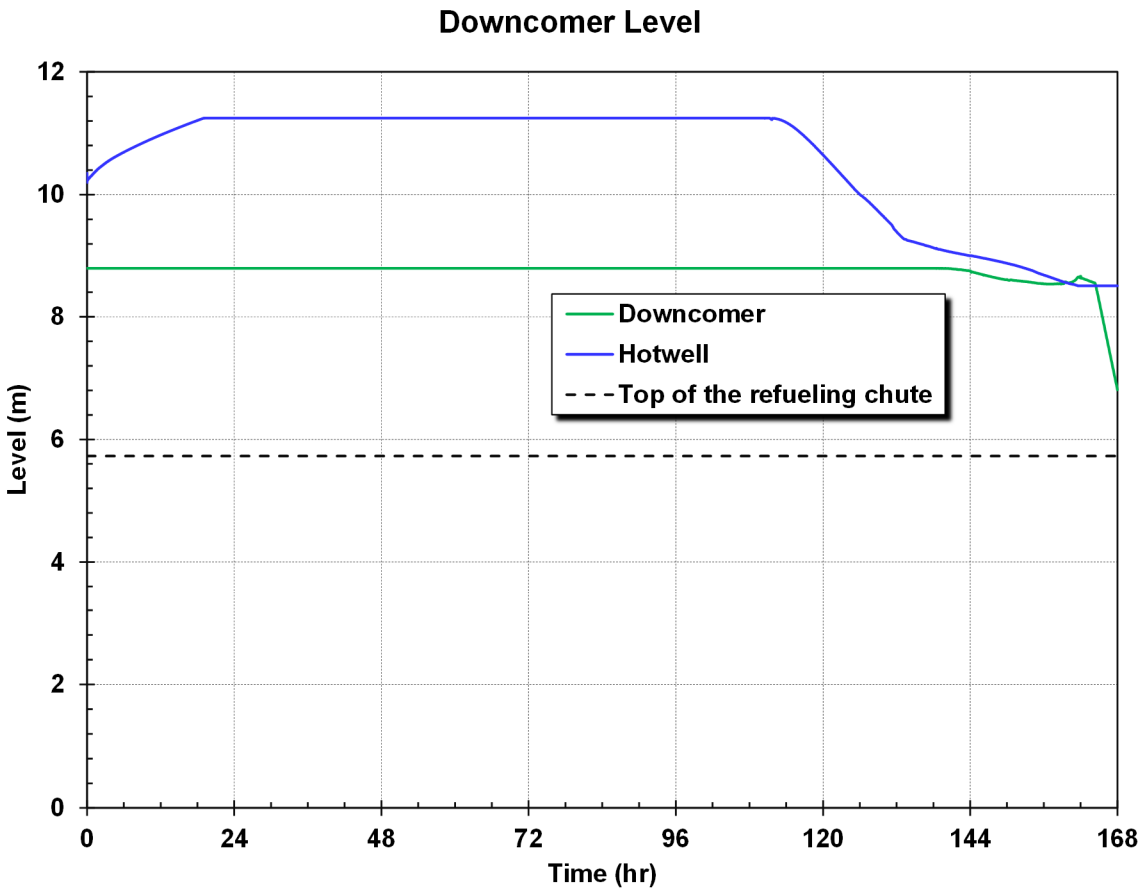

Figure 4-16 Vessel downcomer and hotwell levels for the SBO without DRACS.

4.3. Loss-of-coolant accident

The LOCA scenario was used to demonstrate MELCOR's MST capabilities. The accident is initiated with a loss of all onsite power and a leak in the piping between the bottom of a standpipe and the drain tank (see Figure 3-5 and Figure 3-9). Following the loss-of-onsite power, the reactor protection system inserts the control rods; the main salt pumps trip off; and the secondary heat removal stops. The DRACS is degraded (i.e., only one unit) or unavailable.

A number of scenario variations were considered to illustrate their importance in the thermal-hydraulic progression of the accident. One calculation was extended with fuel overheating to demonstrate the radionuclide release and transport response. The scope of the LOCA sensitivity calculations include (a) the leak size (i.e., relative to a nominal 3" pipe to the drain tank), (b) the availability of one DRACS unit, and (c) the inclusion of a cover-gas connection between the standpipes and the hotwell. Another sensitivity LOCA calculation is presented in Section 4.4 that includes vaporization of cesium from the molten salt. There are many uncertainties that affect the accident progression and timing that could be further explored through uncertainty analysis of the uncertain parameters (e.g., see examples in other non-LWR presentations [21][22]). However, the current effort focused on demonstration of MST capabilities rather than a more extensive analysis of the uncertainties.

The leak in the piping to the drain tank starts the loss of the primary system molten salt inventory into the containment. In the base case response, it is assumed that the cover-gas system is connected to the hotwell but not the top of the standpipe (i.e., the importance will be discussed later). The response of the standpipe liquid level as a function of the leak size is shown in Figure 4-17. The LOCA or leak sizes were varied from 5% to 100% of the 7.62 cm (3") diameter piping. The normal molten salt liquid level in the standpipe is ~9.96 m and the bottom elevation is 0.94 m. The timing to drain the standpipe varies from 0.3 hr to ~5.7 hr for the various leak sizes. The level decreases are impacted by the size of the LOCA and the cold leg connection to the downcomer (i.e., see Figure 3-9). When the leak rate is smaller, there are longer flow interconnections between the downcomer and the other loop that slow the drain rate until the salt level decreases below the bottom of the cold leg connection to the vessel (i.e., 8.8 m). Thereafter, the vessel liquid level is decoupled from the cold leg and standpipe liquid levels.

Figure 4-18 shows the downcomer level response. The impact of the LOCA on the vessel downcomer level response varies according to the size of the LOCA and the cover-gas connection status. The LOCA initially creates a siphon that also draws molten salt from the vessel and the CTAH. Argon gas from the enclosure compartment flows into the hotwell due to the primary system depressurization from the LOCA and the loss of molten salt inventory. The argon gas region expands to form a level depression at the top of the vessel and in the piping to the CTAH (i.e., the argon gas replaces the molten salt volume drained out by the LOCA).

Figure 4-19 and Figure 4-20 show a schematic of the molten salt levels around the Mk1 primary system during the siphon phase and after the equilibration. During the siphon phase, the vessel level is unbalanced with the downcomer-side filled to the top and a depression on the core-side of the vessel. The equilibration of the core-exit side of the vessel and the downcomer side occurs after the argon gas can circulate around the CTAH exit piping to the standpipe (i.e., shown on Figure 4-20). This is evident with the rebalancing of the downcomer and core liquid levels (i.e., the sharp downcomer level decreases between 0.5 hr to 5.4 hr on Figure 4-18 for the various sized LOCAs).

The siphon behavior does not occur if the cover-gas system is also connected to the standpipes.[6] The "100% LOCA + CG" response shown in Figure 4-18 includes a connection of the hotwell to the two standpipes after the pumps trip. In this calculation, an argon bubble can also form at top of the standpipe. The standpipe argon bubble allows downcomer level to decouple from the standpipe level once the cold leg level drops below the bottom of its connection to the downcomer (i.e., 8.8 m). Thereafter, the downcomer level remains at 8.8 m and standpipe drains independently. The hotwell and standpipe cover-gas connections keep the vessel core-side and downcomer levels balanced with one another at 8.8 m.

After the vessel level equilibration, the remaining fluid in the vessel heats due to the core decay heat and expands. The molten salt expansion causes the vessel level to rise and spill into the standpipe. The molten salt continues to spill over into the standpipe until the molten salt in the core approaches the FLiBe saturation temperature. Thereafter, the molten salt in the vessel boils away,

[6] The base case model disabled the cover-gas connections between the hotwell and the standpipes due to its impact on the steady state hotwell and standpipe levels when the salt pumps are operating (see discussion in Section 3.2.2), which led to siphoning. The initial vessel level depression behavior was confusing and led to various sensitivity studies. Reference [4] discusses a liquid overflow connection between the standpipe and the hotwell, which was enabled for gas flow in the "100% LOCA + CG" case after the salt pumps tripped. The siphon response is not intended as a criticism of the design but a reflection of not having the cover-gas system design details. Ultimately, the long-term response was similar with or without the siphon effect.

which is evident in the long-term downcomer level decrease (i.e., see late phase in downcomer response in Figure 4-18).

As shown on Figure 4-18, neither the break size nor the initial siphon behavior had a significant impact on the long-term vessel level response. The consistent long-term response occurs because most of the vessel salt inventory lies below the top of the refueling chute. Since this portion of the vessel is not drained or not significantly drained, the time to heat to saturation conditions is relatively uniform. While the salt is heating, it expands above 8.8 m for the larger break sizes and then spills into the standpipe. However, after the molten salt starts boiling, the salt vapor flows out of the vessel and through the piping break into the containment. The boiling phase starts the boiloff and level decrease that eventually uncovers the fuel pebbles in the core.

The downcomer level response for four 100% LOCA cases as a function of DRACS availability and the cover-gas connection between the hotwell to the standpipes are shown Figure 4-21. As discussed above, the cover-gas connection to the standpipes avoids the initial siphon phase. The response of the two cases without DRACS are the same as described earlier. However, the availability of one DRACS unit changes the response significantly. If the DRACS is available and the cover-gas system connections stop a siphon, then the vessel level remains full.[7] Figure 4-22 shows that the DRACS case with the cover-gas connection (i.e., "100% LOCA + CG + 1xDRACS") remained below 750°C through 1-week. In contrast, the two cases without DRACS reached 2000°C within 43 hr.

The vessel initially drains due to a siphon effect in the "100% LOCA + 1xDRACS" case without the standpipe to hotwell cover-gas connection but with the DRACS is available. The DRACS was not effective during the level depression because the vessel molten salt level was below the connection to the DHX. However, the heating of the salt caused it to expand above the connection to the DHX. The salt started to circulate through the DRACS piping to the DHX. The natural circulation flow of the molten salt through the DHX stopped the core heatup below the saturation temperature of the salt (see Figure 4-22). The system reached a quasi-steady balance where there was sufficient heating and expansion to maintain the molten salt level above the DHX connection but enough cooling to remove the core decay heat. The long-term maximum fuel temperature was ~1220°C.

The "75% LOCA" case is used to demonstrate a MST.[8] The "75% LOCA" simulated the heat-up and boiloff of the molten salt in the core. Without the DRACS heat removal, the molten salt inventory in the core boiled away. The calculation was terminated at 54 hr when the maximum fuel temperatures approached the UO_2 fuel kernel melting temperature (i.e., $\geq$2800°C). Although the fuel kernels were very hot, the fuel kernel and pebble temperatures were well below the sublimation temperature of the graphite pebbles and reflectors (i.e., $T_{sublimation}$ is ~3600°C).

The steel structure temperatures at various locations are shown in Figure 4-23. The upper core barrel is heating towards the melting temperature of the stainless steel likely loosing strength. The core barrel does not support the core and primarily serves to define the downcomer region around the outer surface of the reflector. The reactor vessel wall above the liquid salt level benefits from some radiative cooling to the reactor cavity wall in the upper locations. The upper vessel wall is

---

[7] It was assumed that the DRACS connection to the DHX, which allows the liquid flow into the DHX from the core exit piping, was not above the spillover elevation to the hot and cold legs. The hot and cold leg connections to the vessel are at 8.805 m and the core exit connection to the DHX is at 8.229 m. These elevations were estimated and assumed, respectively. If the DRACS connection to the DHX was above the hot and cold leg connections, then there was no liquid natural circulation flow into the DHX and the DRACS was ineffective at removing the core decay heat.

[8] The accident progression of the 75% LOCA was very similar to the 100% LOCA.

somewhat insulated from the hot outer reflector due to only salt vapor in the upper portion of the downcomer (see Figure 4-24). Since the molten salt in the lower plenum is near the saturation temperature and has good heat transfer to the lower head, the lowest level reactor vessel temperature remains hot (i.e., near the molten salt saturation temperature). The creep slumping of the vessel wall was not evaluated. However, the vessel lower head and side walls are very close to the fire brick liner, which is surrounded by a stainless steel liner and thick concrete walls. Consequently, there would be relatively little movement due to the minimal cavity volume design.

The TRISO failure fraction and the peak fuel temperature are shown in Figure 4-25. The TRISO failure fraction remained relatively low (i.e., 1.7×10^{-4}) until the top of the fuel uncovered at 34 hr. Subsequently, the overall TRISO failure fraction increased as the fuel heated to $\geq$2800°C. Since the accident was unmitigated, the magnitude of the TRISO failure damage through 54 hr is significant (i.e., >7.5% at 54 hr).

The iodine and cesium release from the pebbles and their distribution are shown in Figure 4-26 and Figure 4-27, respectively. The TRISO coatings are very effective at retaining the iodine until the temperature exceeds 1800°C near 41 hr. There is a sharp rise in the iodine release after 41 hr as the maximum fuel temperature increases from saturation conditions at 34 hr to >2800°C at 54 hr. The fuel pebbles uncover during this time and most releases go into the salt vapor. The pressurization from the in-vessel salt vaporization carries the released iodine into the containment with some reaching the environment. The TRISO diffusivities and failure fraction correlation are being extrapolated above 1800°C because of a lack of experimental data above 1800°C.

The cesium response in Figure 4-27 illustrates some differences from the iodine response. The iodine release is modeled using krypton diffusivities, which are measured to be very effective at retaining gases below 1800°C. In contrast, the cesium begins releasing at lower temperatures. The cesium releases occur due to the initial TRISO manufacturing defects (i.e., assumed to be 10^{-5}), from the new failures as the TRISOs heated to saturation conditions, and through diffusion through intact TRISOs at high temperatures. However, the early cesium releases through 34 hr are assumed to be retained in the molten salt (i.e., see the molten salt levels at 34 hr in Figure 4-28).[9] After the core begins uncovering, the cesium releases from the pebbles go into the gas space in the high temperature region above the core molten salt level. The cesium distribution shows the new releases leaving the vessel into the containment (i.e., similar to the iodine behavior after 42 hr). A small amount of the cesium is released to the environment through 54 hr due to the release into the containment and the small containment pressurization from the in-vessel salt vapor generation.[10]

[9] Section 4.4 presents a sensitivity study on the cesium behavior in the molten salt during the first 24 hr of the calculation.

[10] The salt vapor also condenses in the containment, which limits the magnitude of the containment pressurization.

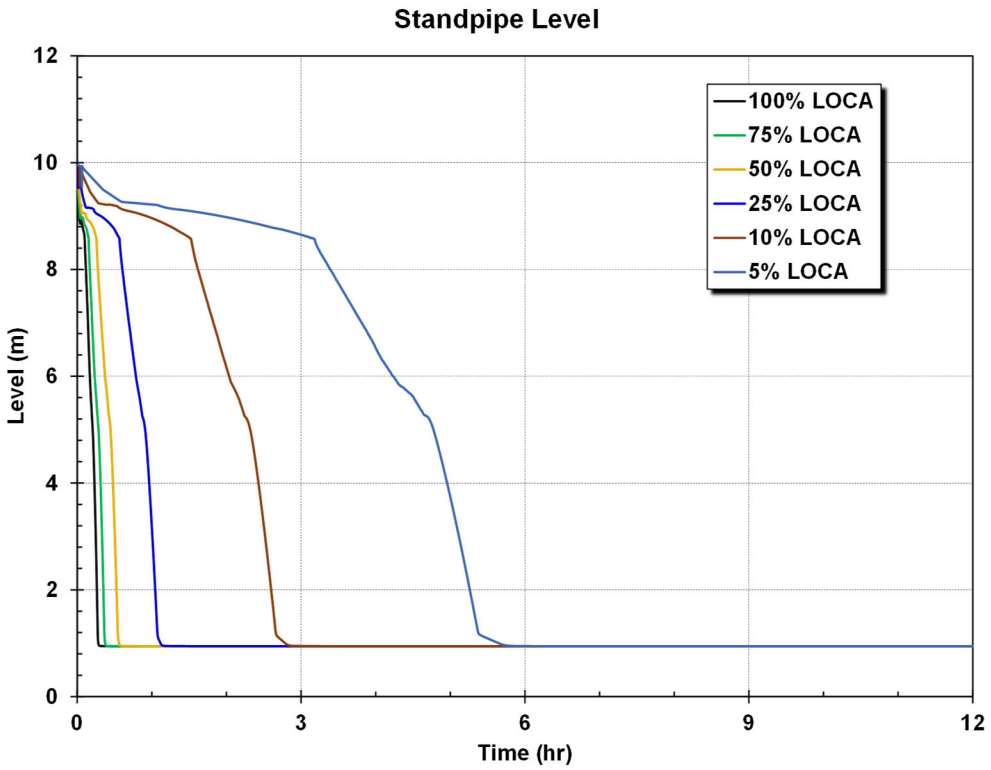

Figure 4-17 Standpipe salt level response versus LOCA size.

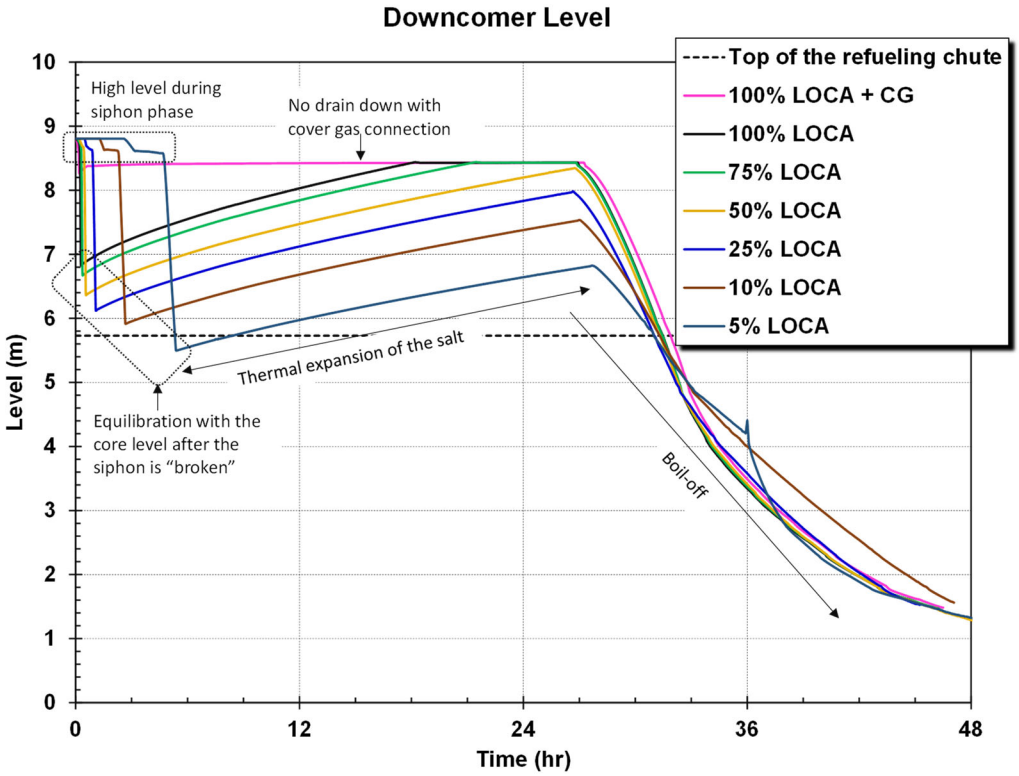

Figure 4-18 Vessel downcomer salt level response versus LOCA size.

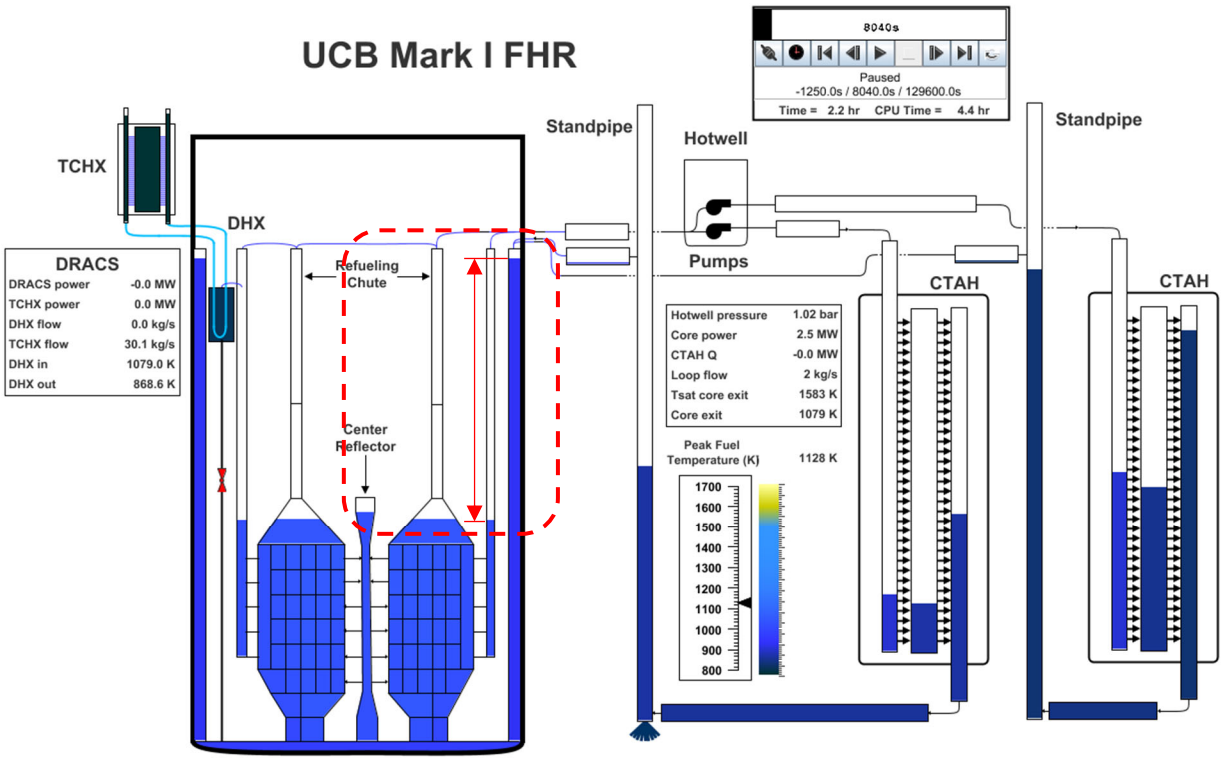

Figure 4-19 Mk1 salt levels in the 10% LOCA prior to the siphon break.

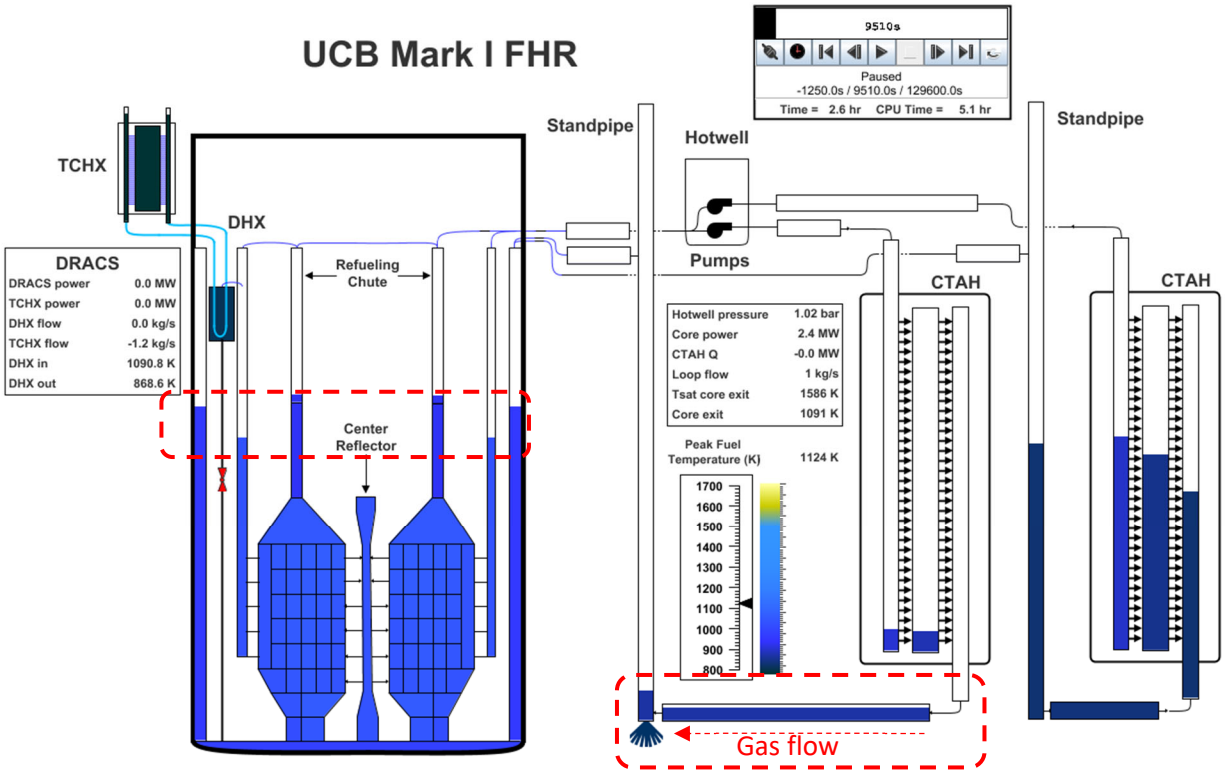

Figure 4-20 Mk1 salt levels in the 10% LOCA after equilibration.

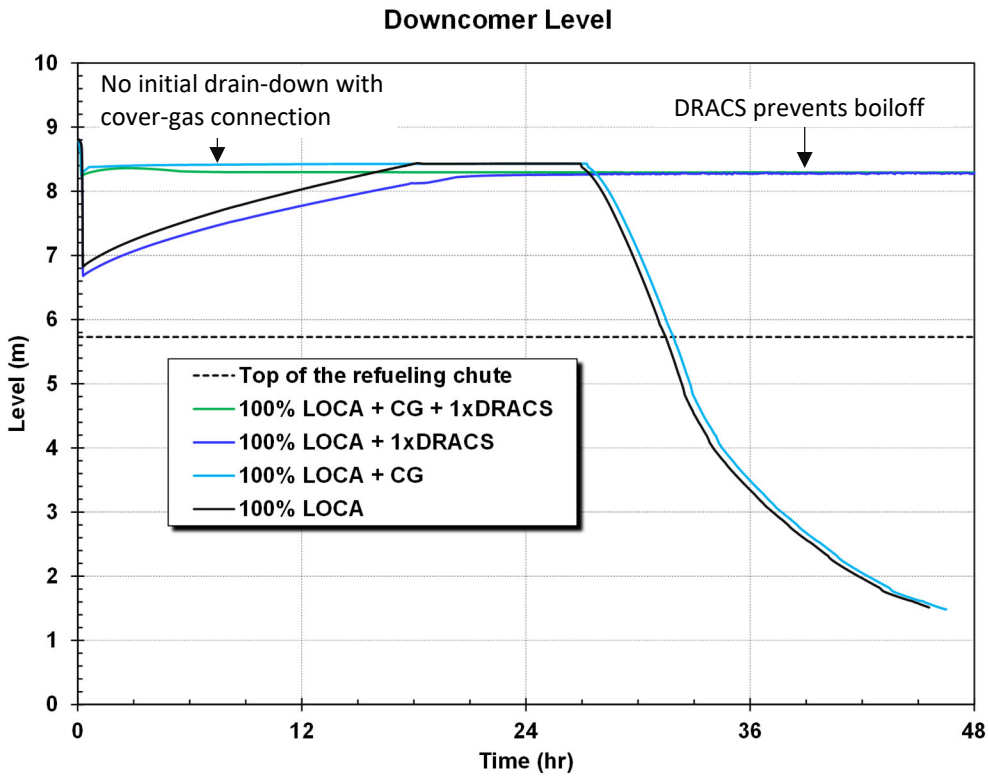

Figure 4-21 Mk1 vessel downcomer level in the 100% LOCA scenarios.

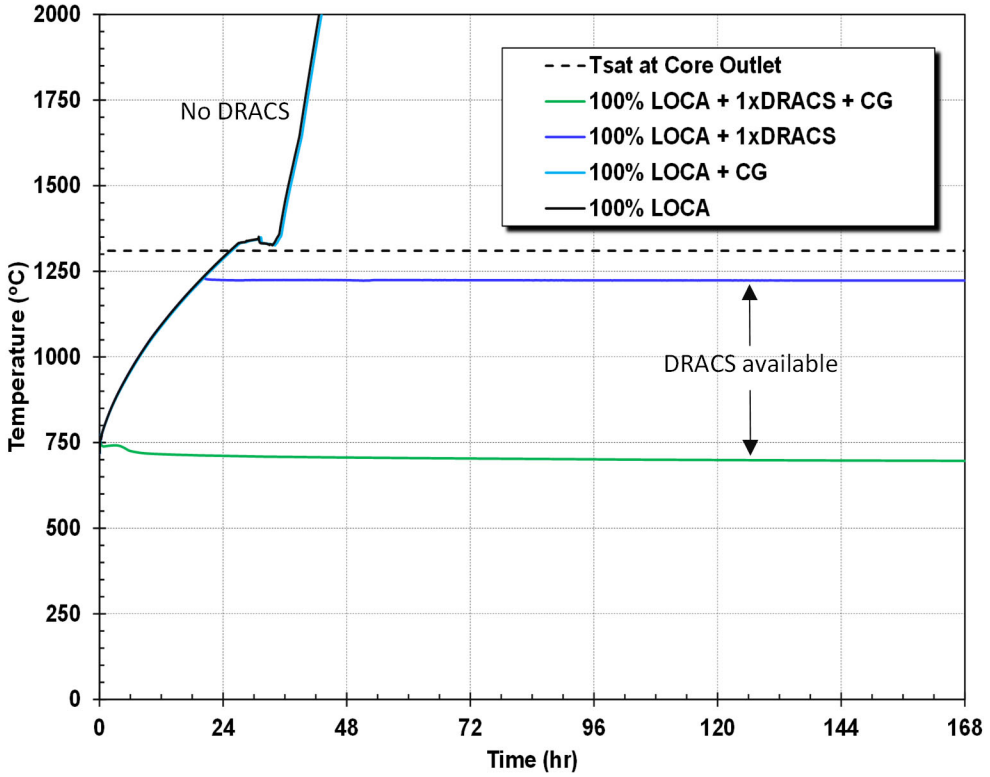

Figure 4-22 Mk1 peak fuel temperatures in the 100% LOCA scenarios.

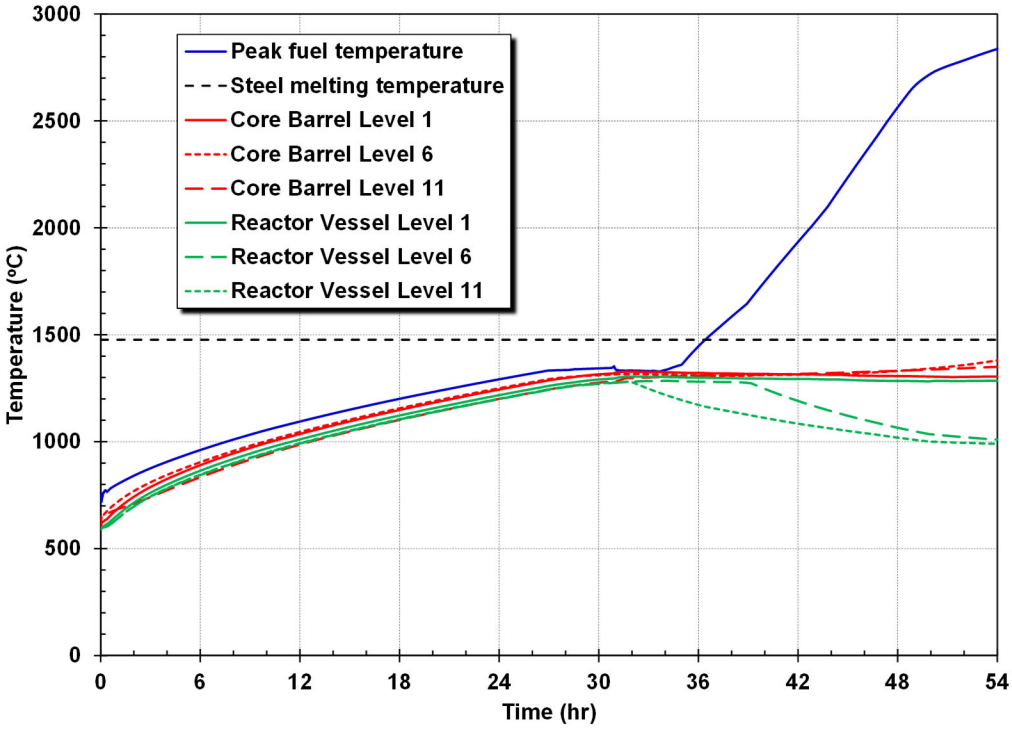

Figure 4-23 Mk1 vessel steel structure temperatures in the 75% LOCA scenario.

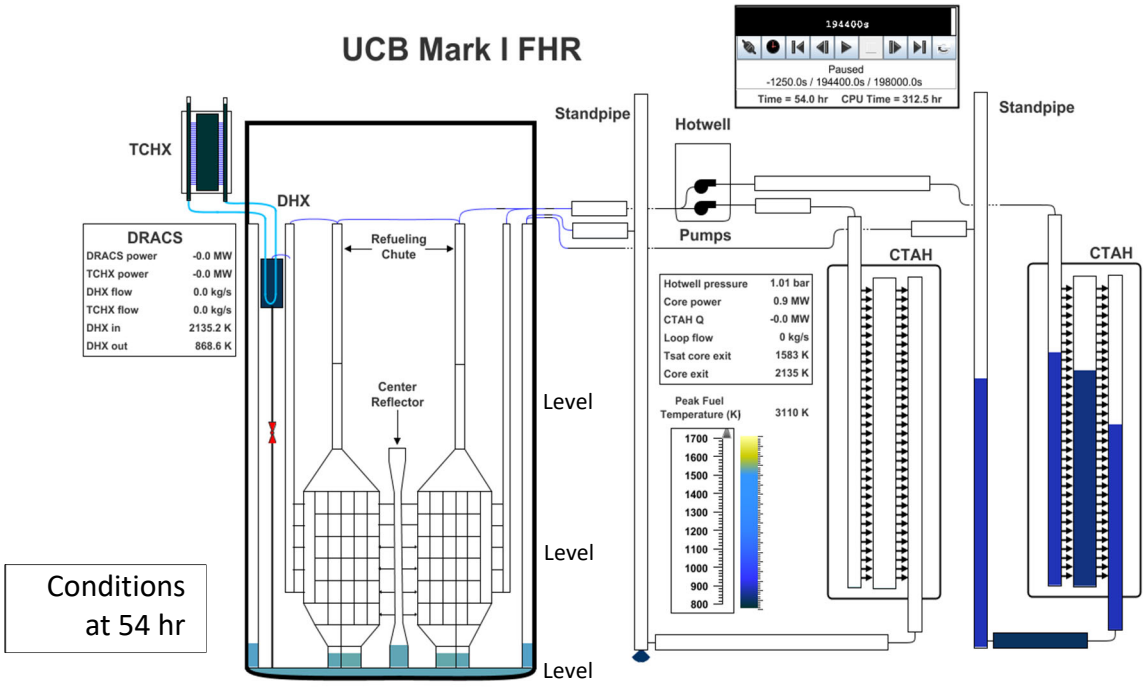

Figure 4-24 Mk1 system levels at 54 hr in the 75% LOCA scenario.

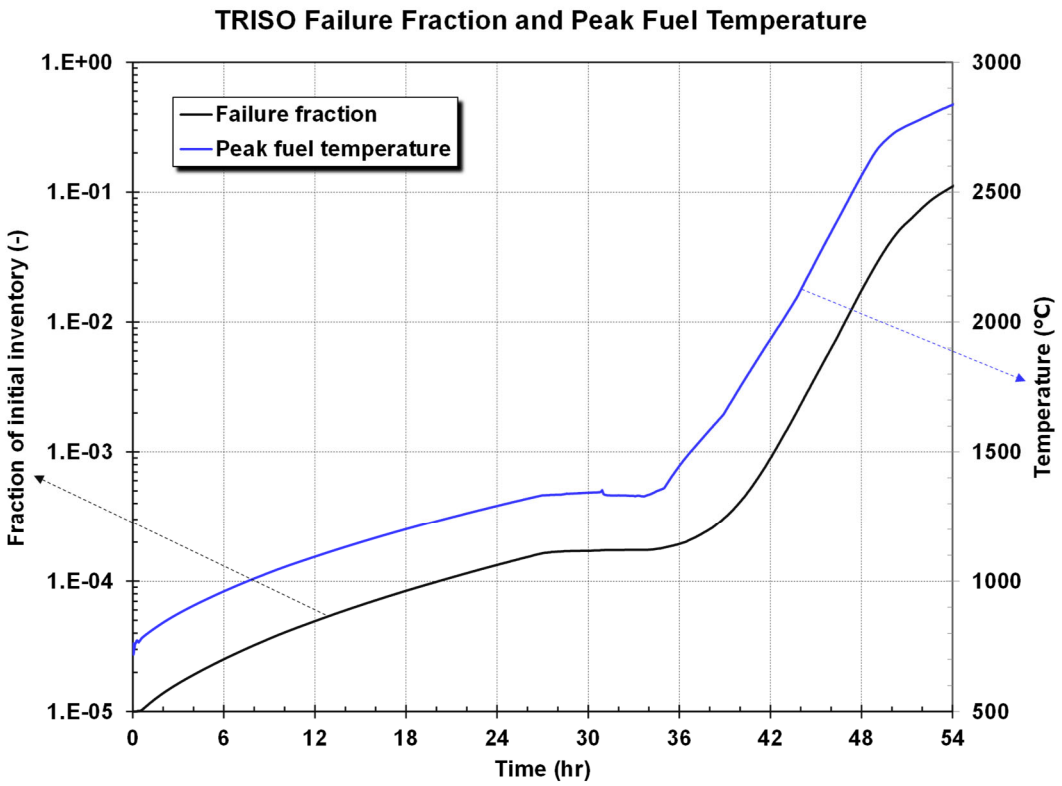

Figure 4-25 Mk1 TRISO overall failure fraction and the peak fuel temperature in the 75% LOCA scenario.

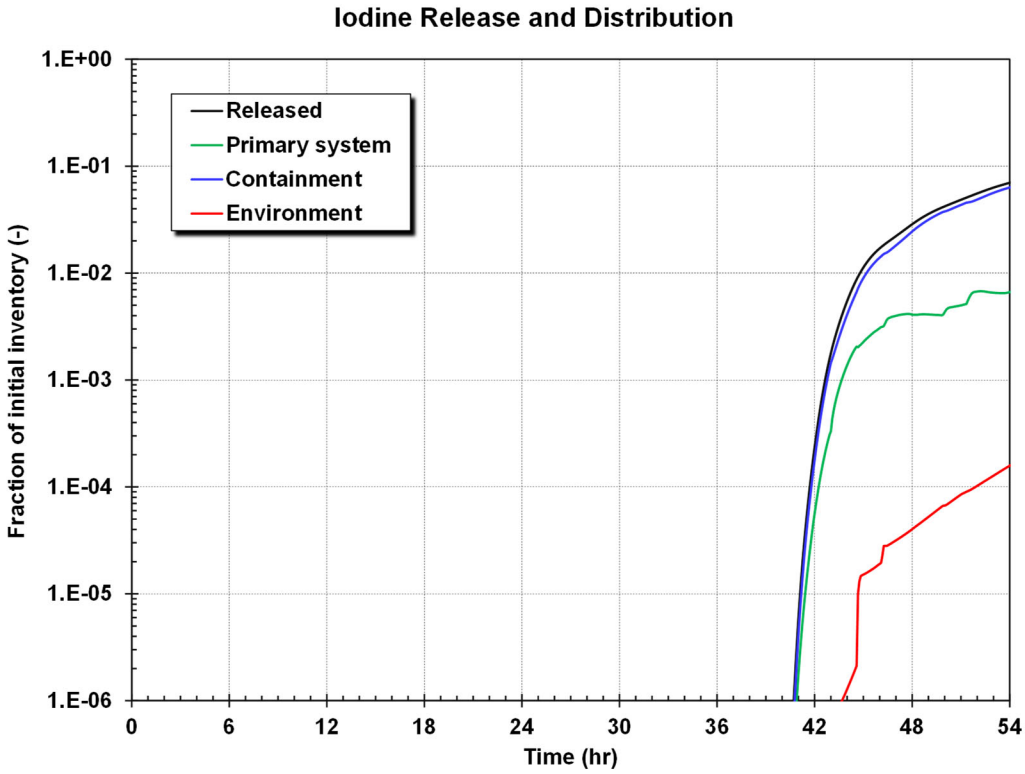

Figure 4-26 Mk1 iodine release and distribution in the 75% LOCA scenario.

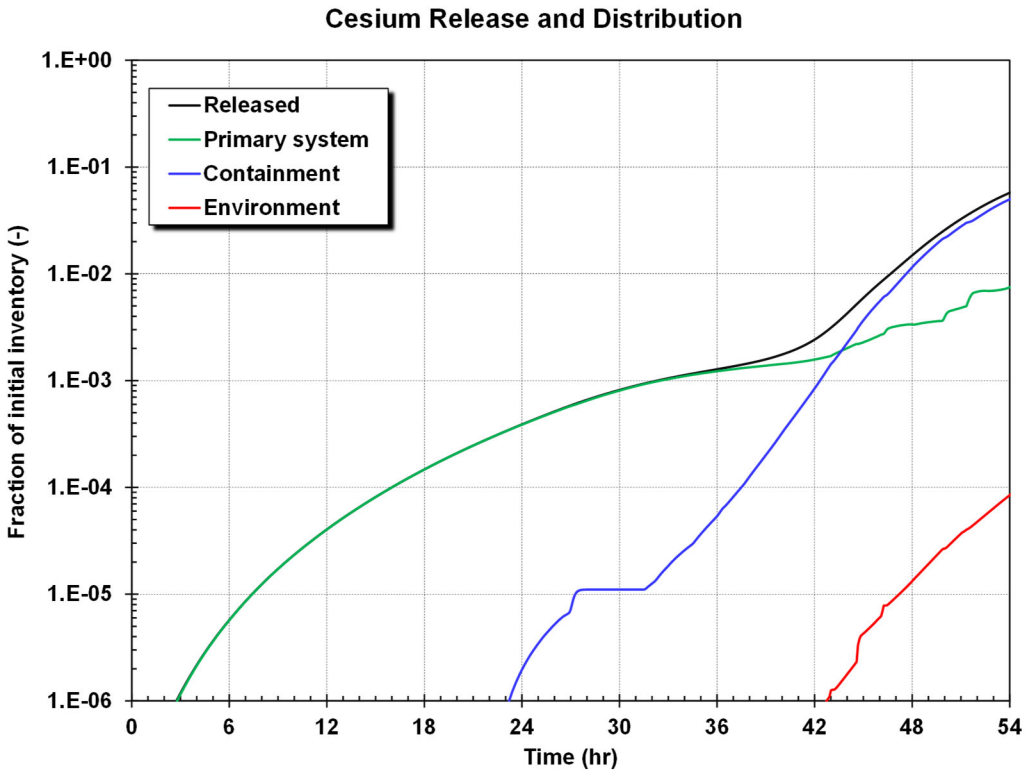

Figure 4-27 Mk1 cesium release and distribution in the 75% LOCA scenario.

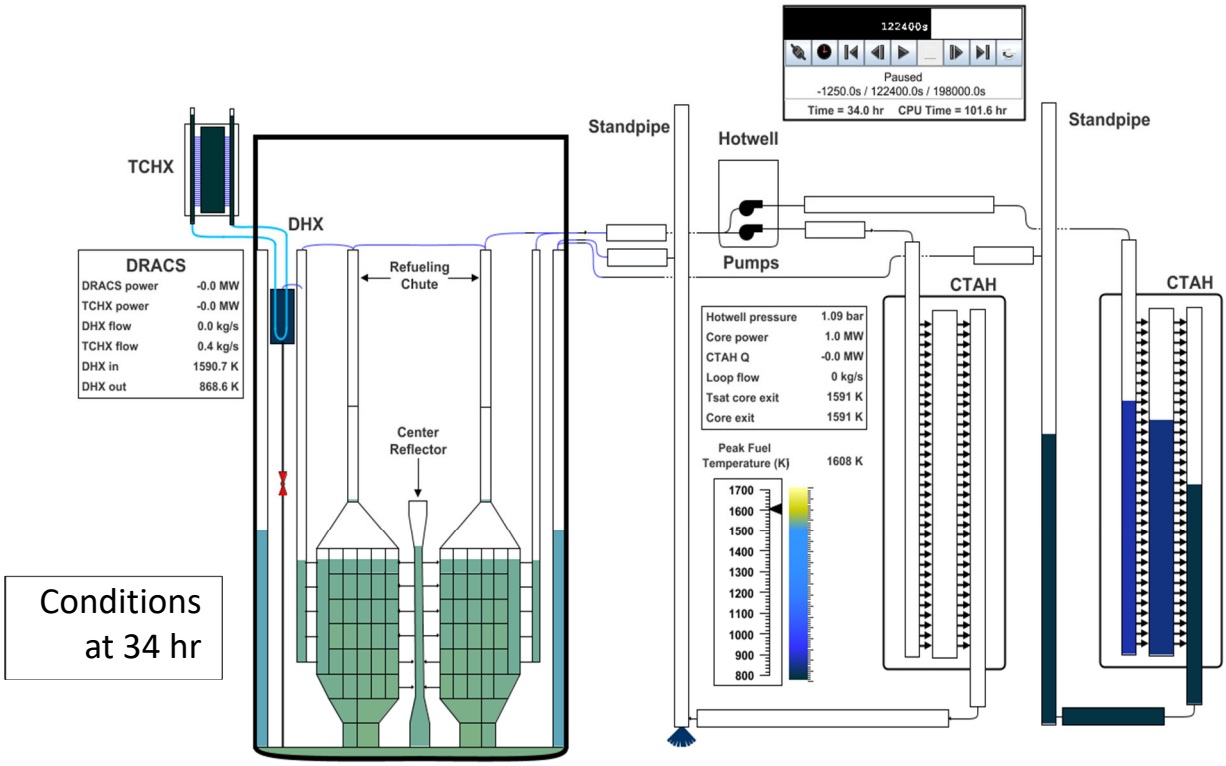

Figure 4-28 Mk1 system levels at 34 hr in the 75% LOCA scenario.

4.4. Loss-of-coolant accident with the pool chemistry model

The first 24 hr of a 10% LOCA calculation was rerun using the pool chemistry and release model (see Section 3.5.2 for a description). The 10% LOCA included the cover-gas connection between the hotwell and the standpipes to maintain the vessel inventory during the initial loop drain-down. The accelerated steady state was not used, so the initial cesium inventory in the primary system was limited to the releases following the accelerated steady state (i.e., Phase 2, see Section 3.5.1). The pool chemistry and release model was used to examine the cesium fission product release from the molten salt pool to the vapor prior to the pebble uncovery. Whereas the previous calculations retained any cesium released in the molten salt, the new calculation included a mass transfer calculation for cesium release (i.e., Cs and CsF) in control volumes with a free surface. Due to limitations in the available molten salt databases, the pool chemistry and release calculations were limited to just the cesium behavior in the molten salt. The calculation was run for 24 hr and included the heating phase of the molten salt towards the molten salt saturation temperature.

Figure 4-29 shows the cesium behavior in the primary system. The cesium release from the fuel builds up from approximately 10^{-8} at the start of the transient to 3.1×10^{-4} by 24 hr. Initially, all the cesium is retained in the molten salt. However, once the salt temperature exceeds 950°C near 7.3 hr[11], the amount vaporized from the liquid to the gas space started to increase from $<1 \times 10^{-8}$ to 1×10^{-6} by 8.3 hr. Subsequently, the cesium vaporization increased over two-orders of magnitude through 24 hr (i.e., 1.4×10^{-4} at 24 hr). Figure 4-30 shows that the percentage of the released cesium that subsequently vaporized rose to 44% by 24 hr.

The cesium distribution between the primary system, containment, and environment is shown in Figure 4-31. In comparison with the LOCA results in Section 4.3, the fraction released to the containment over the first 24 hours was over an order of magnitude larger (8×10^{-5} versus 2×10^{-6}). Similarly, the amount released to the environment over the first 24 hours was also much larger (4×10^{-7} versus 4×10^{-12}).

The results from the pool chemistry and release model show an additional refinement on the timing of the cesium release to the containment. As the molten salt temperature increases above 950°C, a significant portion of the released cesium was calculated to vaporize from the free surfaces near the top of the vessel and transport to the containment. While the overall impact was small compared to the subsequent vapor phase releases, the vaporization could be important in mitigated accidents (e.g., the "100% LOCA + 1xDRACS" case discussed in Section 4.3 and shown in Figure 4-22).

[11] This was a 235°C temperature rise over the nominal core exit molten salt temperature of 715°C, which represents a significant heat up.

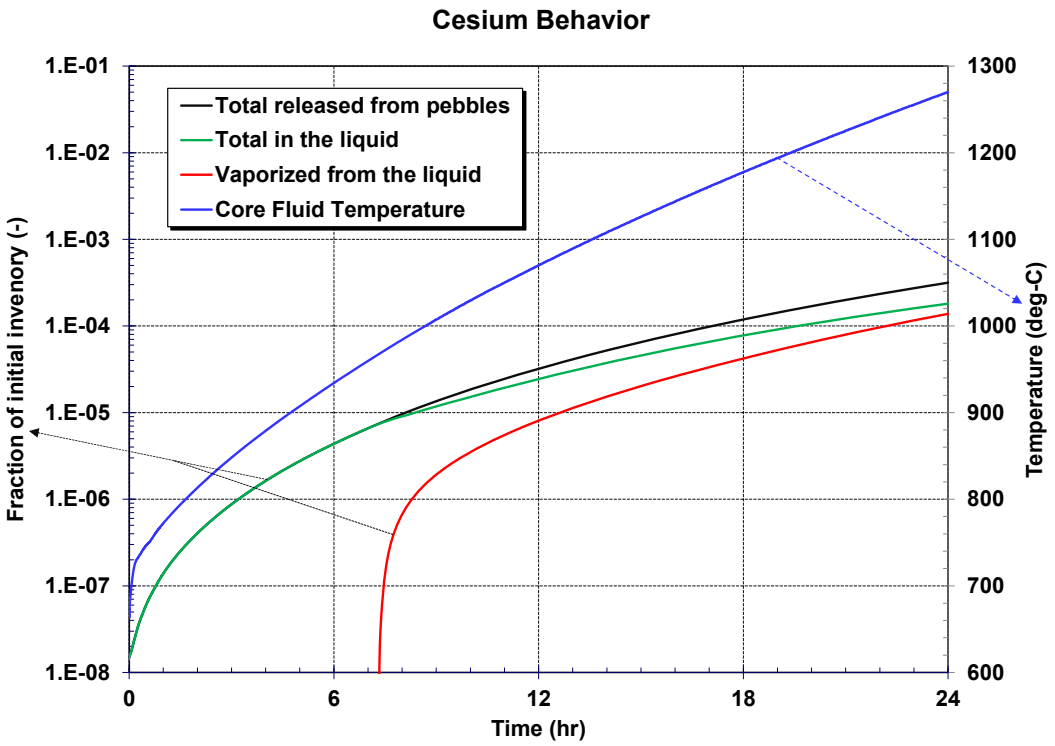

Figure 4-29 Cesium behavior in the 10% LOCA scenario with the pool chemistry and release model.

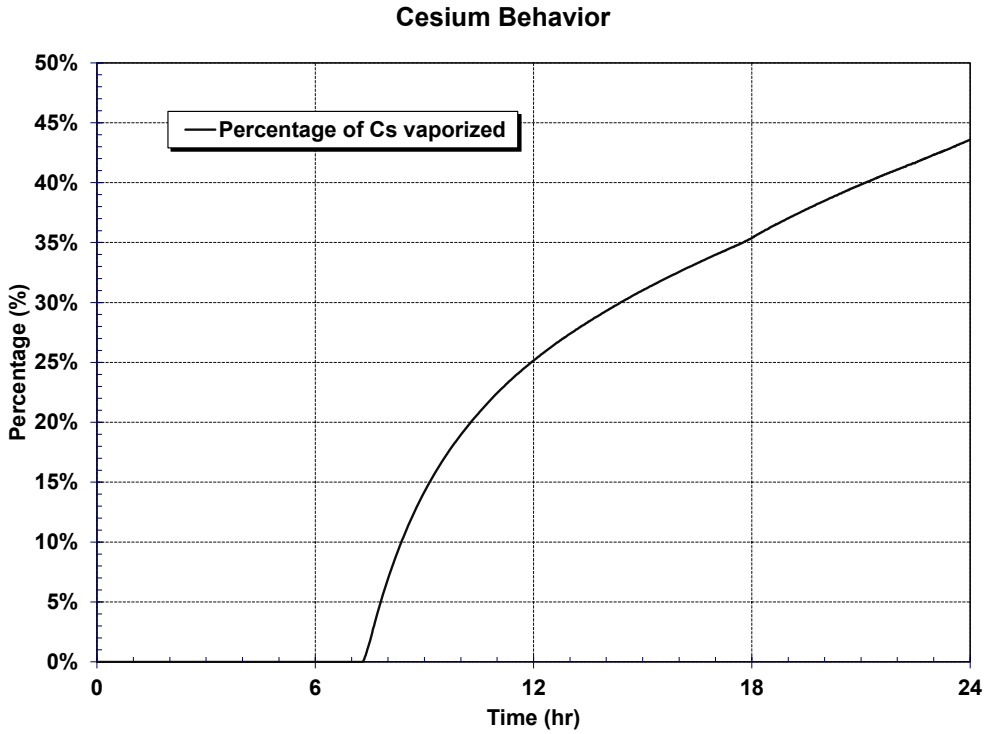

Figure 4-30 Percentage of the cesium released from the pebbles that vaporized in the 10% LOCA scenario with the pool chemistry and release model.

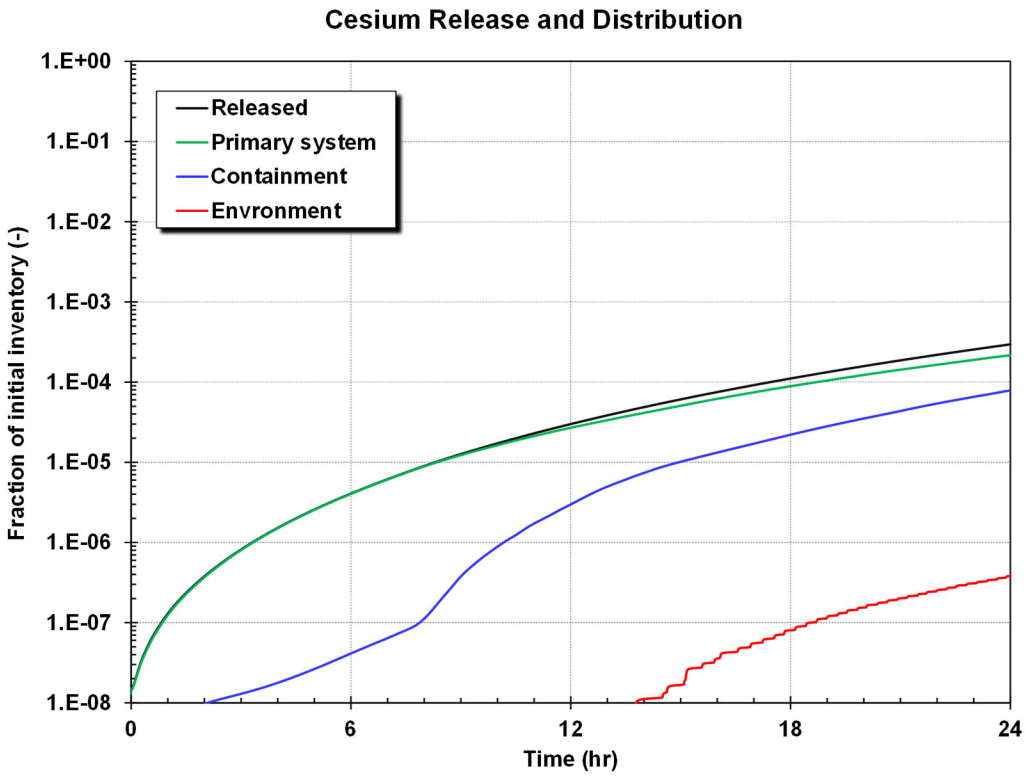

Figure 4-31 Cesium release and distribution in the 10% LOCA scenario with the pool chemistry and release model.

5. SUMMARY

The MELCOR code has been updated to support NRC safety evaluations of accidents in FHRs. This report presents demonstration calculations for a FHR from publicly available literature for the UCB Mk1 design. For plant aspects (e.g., reactor building leak rate and details of the cover-gas system) that are not described in the FHR references, the required inputs were estimated or assumed to construct a MELCOR full-plant model. A model of the Mk1 was developed to demonstrate a mechanistic source term analysis, which included the vessel with the pebble bed core, the molten salt circulation system, the secondary CTAH, and the containment building. The Mk1 input model was used to demonstrate ATWS, SBO, and LOCA scenarios. The LOCA was selected to demonstrate the evaluation of the source term. Sensitivity calculations were performed on some of the uncertain inputs to illustrate the code's response to these variations. The analyses demonstrate the flexible capabilities of MELCOR to evaluate the accident progression in a FHR. The code can incorporate evolving data from ongoing research programs and includes flexible inputs for sensitivity and Monte Carlo sampling on uncertain parameters.

REFERENCES

[1] "Non-LWR Vision and Strategy Near-Term Implementation Action Plans," Nuclear Regulatory Commission, ADAMS Accession No. ML16334A495, 2019.

[2] "Nuclear Energy Innovation and Modernization Act," Public Law No: 115-439, January 2019.

[3] B. Rearden and M. Jessee, "SCALE Code System, ORNL/TM-2005/39, Version 6.2.3," UT-Battelle, LLC, Oak Ridge National Laboratory, 2018.

[4] Andreades, C., et al., "Technical Description of the "Mark 1" Pebble-Bed Fluoride-Salt-Cooled High-Temperature Reactor (PB-FHR) Power Plant," University of California, Berkeley, UCBTH-14-002, September 2014.

[5] "SCALE/MELCOR Non-LWR Source Term Demonstration Project – Fluoride-Salt-Cooled High-Temperature Reactor (FHR)," NRC Adams Ascension Number ML21256A231, https://www.nrc.gov/docs/ML2125/ML21256A231.pdf, September 14, 2021.

[6] Humphries, L. L., et al., MELCOR Computer Code Manuals: Volume 1; Reference Manual - Version 2.2.18019, Sandia National Laboratories, SAND2019-13442, Jan 2021.

[7] Humrickhouse, P. W., and Merrill, B. J., "Revised Equation of State for FLiBe in MELCOR," Idaho National Laboratory, INL/EXT-17-44148, Revision 0, December 2017.

[8] Cisneros, A. T., "Fluoride Salt Cooled High Temperature Reactor (PB-FHR)," University of California, https://escholarship.org/uc/item/55h9183p, 2013.

[9] F. Bostelmann, C. Celik, R. F. Kile, W. A. Wieselquist (2021), "SCALE Analysis of a Fluoride Salt-Cooled High-Temperature Reactor in Support of Severe Accident Analysis", ORNL/TM-2021/2273, Oak Ridge National Laboratory, Oak Ridge, TN.

[10] "PBMR Coupled Neutronics/Thermal-hydraulics Transient Benchmark - The PBMR-400 Core Design," NEA/NSC/DOC(2013)10, July 2013.

[11] Louie, D. L., Humphries, L. L., "NSRD-10: Leak Path Factor Guidance Using MELCOR," Sandia National Laboratories, SAND2017-3200, March 2017.

[12] ASHRAE, "Handbook of Fundamentals," American Society of Heating, Refrigerating and Air-Conditioning Engineers, Inc, 1997.

[13] R.N. Morris, et al., " TRISO-Coated Particle Fuel Phenomenon Identification and Ranking Tables (PIRTs) for Fission Product Transport Due to Manufacturing, Operations, and Accidents," NUREG/CR-6844, Vol.1, U.S. Nuclear Regulatory Commission, Washington, DC (2004).

[14] "Fuel performance and fission product behavior in gas cooled reactors," IAEA TEDOC-0978, November 1997.

[15] Collin, B. P., "Diffusivities of Ag, Cs, Sr, and Kr in TRISO Fuel Particles and Graphite," Idaho National Laboratory, INL/EXT-16-39548, Revision 0, September 2016.

[16] Demkowicz, P. A., Liu, B., and Hunn, J. D., "Coated particle fuel: Historical perspectives and current progress," Journal of Nuclear Materials, Vol. 515, pg. 434-450, 2019.

[17] R.O. Gauntt, "Synthesis of VERCORS and Phebus Data in Severe Accident Codes and Applications", SAND 2010-1633, Sandia National Laboratories, Albuquerque, NM, April 2010.

[18] Dwaraknath, S. S., and Was, G. S., "Radiation enhanced diffusion of cesium, strontium, and europium in silicon carbide," Journal of Nuclear Materials, Vol. 474, pg. 76-87, 2016.

[19] Miller, G. K., Petti, D. A., Maki, J. T., Knudson, D. L., Skerjanc, W. F., "PARFUME Theory and Model Basis Report," Idaho National Laboratory, INL/EXT-18-14497, September 2018.

[20] El-Genk, M. S., and Tournier, J. P., "A Point Kinetics Model for Dynamic Simulations of Next Generation Nuclear Reactor," Progress in Nuclear Energy, Volume 92, September 2016, pp. 91-103.

[21] "SCALE/MELCOR Non-LWR Source Term Demonstration Project – Heat Pipe Reactor," NRC Adams Ascension Number ML21200A179, https://adamswebsearch2.nrc.gov/webSearch2/main.jsp?AccessionNumber= ML21179C060 , June 2021.

[22] "SCALE/MELCOR Non-LWR Source Term Demonstration Project – High-Temperature Gas-cooled Reactor," NRC Adams Ascension Number ML21200A179, https://www.nrc.gov/docs/ML2120/ML21200A179.pdf, July 2021.

DISTRIBUTION

Email—Internal

Name	Org.	Sandia Email Address
David Luxat	08852	dlluxat@sandia.gov
Brad Beeny	08852	babeeny@sandia.gov
Technical Library	01977	sanddocs@sandia.gov

Email—External [redacted]

Name	Company Email Address	Company Name
Jason Schaperow	jason.schaperow@nrc.gov	NRC
Hossein Esmaili	hossein.esmaili@nrc.gov	NRC
Shawn Campbell	campbell.shawn@nrc.gov	NRC

Hardcopy—Internal

Number of Copies	Name	Org.	Mailstop

This page left blank

This page left blank

Sandia National Laboratories

Sandia National Laboratories is a multimission laboratory managed and operated by National Technology & Engineering Solutions of Sandia LLC, a wholly owned subsidiary of Honeywell International Inc. for the U.S. Department of Energy's National Nuclear Security Administration under contract DE-NA0003525.